

12-9-2014

Electrochemical Synthesis of Nanostructured Noble Metal Films for Biosensing

Jay Kishan Bhattarai

University of Missouri-St. Louis

Follow this and additional works at: <https://irl.umsl.edu/dissertation>



Part of the [Chemistry Commons](#)

Recommended Citation

Bhattarai, Jay Kishan, "Electrochemical Synthesis of Nanostructured Noble Metal Films for Biosensing" (2014). *Dissertations*. 212.
<https://irl.umsl.edu/dissertation/212>

This Dissertation is brought to you for free and open access by the UMSL Graduate Works at IRL @ UMSL. It has been accepted for inclusion in Dissertations by an authorized administrator of IRL @ UMSL. For more information, please contact marvinh@umsl.edu.

Electrochemical Synthesis of Nanostructured Noble Metal Films for Biosensing

Jay K. Bhattarai

M.S., Chemistry, University of Missouri–St. Louis, MO, 2011

M. Sc., Physical Chemistry, Tribhuvan University–Kirtipur, 2007

A Dissertation Submitted to the Graduate School at the University of Missouri–St. Louis

In Partial Fulfillment of the Requirements for the Degree

Doctor of Philosophy in Chemistry

December 2014

Advisory Committee

Prof. Keith J. Stine, Ph.D. (Chairperson)

Prof. James S. Chickos, Ph.D.

Prof. Alexei V. Demchenko, Ph.D.

Prof. Michael R. Nichols, Ph. D.

ABSTRACT

Electrochemical Synthesis of Nanostructured Noble Metal Films for Biosensing

Jay K. Bhattarai, Prof. Keith J. Stine (Advisor)

University of Missouri–St. Louis, MO, USA

Nanostructures of noble metals (gold and silver) are of interest because of their important intrinsic properties. Noble metals by themselves are physically robust, chemically inert, highly conductive, and possess the capability to form strong bonds with thiols or dithiol molecules present in organic compounds, creating self-assembled monolayers with tunable functional groups at exposed interfaces. However, when the nanostructures are formed, they in addition possess high surface area and unique optical properties which can be tuned by adjusting the shape and the size of the nanostructures. All of these properties make nanostructures of noble metals suitable candidates to be used as a transducer for optical and electrochemical biosensing. Individual nanostructures might be easier to prepare but difficult to handle to use as a transducer. Therefore, we prepared and analyzed nanostructured films/coating of noble metals and used them as a transducer for optical and electrochemical biosensing.

We have electrochemically prepared nanoporous gold (NPG) on gold wire varying different dependable parameters (deposition potential, time, and compositional ratio) to obtain an optimal structure in term of stability, morphology, and better surface area. NPG prepared using a deposition potential of -1.0 V for 10 min from 30:70% 50 mM $\text{K}[\text{Au}(\text{CN})_2]$ and 50 mM $\text{K}[\text{Ag}(\text{CN})_2]$ was used as an optimal surface for protein immobilization, and to perform square wave voltammetry (SWV) based enzyme-linked

lectinsorbent assays. On flat gold surfaces, adjacent protein molecules sterically block their active sites due to high-density packing, which can be minimized using NPG as a substrate. NPG can also show significant peak current in SWV experiments, a sensitive electrochemical technique that minimizes non-Faradaic current, which is difficult to obtain using a flat gold surface. These all make NPG a suitable substrate, electrode, and transducer to be used in electrochemical biosensing.

We have also discovered a facile electrochemical method to synthesize novel plasmonic noble metal nanostructured films. Plasmonic noble metal nanostructures have promising applications in photovoltaic solar cells, cloaking, and molecular sensing. Here, we used plasmonic noble metal nanostructures as a transducer for biosensing using localized surface plasmon resonance (LSPR) spectroscopy, a label-free biosensing technique. The prepared nanostructured films are not only sensitive for detecting biomolecules, but are stable chemically and physically, and can be easily regenerated. We have compared the sensitivity of three different types of nanostructured films, namely; nanostructured gold film (NGF), nanostructured silver film (NSF), and NPG film, and discussed the advantages and disadvantages of the prepared structures. Finally, we report carbohydrate–lectin, lectin–protein, and layer-by-layer interactions of molecules using LSPR spectroscopy. We have also performed real-time interactions and concentration dependent studies to find the equilibrium dissociation constant of the interactions. The results from these experiments could contribute to the development of cheap and sensitive biosensors that can be used for diagnostic purposes.

DEDICATION

To my Family

ACKNOWLEDGEMENT

First and foremost, I would like to express my sincere gratitude to my advisor, Prof. Keith J. Stine, for his guidance, support, patience, and encouragement throughout my Ph.D. at University of Missouri-St. Louis. I am indebted to him for all his help. Without his guidance and effort, this research would have been far from completion.

I would like to acknowledge Prof. James S. Chickos, Prof. Alexei V. Demchenko, and Prof. Michael R. Nichols for being the part of the committee and providing me valuable suggestions and encouragement.

I want to acknowledge my former lab mates Dr. Kenise Jefferson, Dr. Yih H. Tan, Dr. Binod Pandey, and Dr. Abeera Sharma for mentoring me in my early days, creating excellent working environment, and collaborating in different projects. I want to thank my current lab mate Allan J. Alla for helpful discussions on different projects and creating excellent working environment in the lab. I would also like to thank all the masters, undergraduate, and high school students who have directly or indirectly worked with me to move the projects forward. I am thankful to Dr. Kohki Fujikawa from Prof. Demchenko's lab who synthesized thiolated glycosides and PEG derivatives required for our experiments. I would like to wish them all better and successful future.

I am grateful to Dr. David Osborn from microscopy laboratory for guiding me while taking SEM images. I am also thankful to all the respected professors, staff, graduate students, and undergraduate students in the UMSL Department of Chemistry and Biochemistry and Center for Nanoscience for creating friendly and productive environment.

I would like to thank my grandmother Bed Maya Bhattarai, father Tilak Bhattarai, mother Ganga Bhattarai, brother Bijay Bhattarai, wife Rozina Karki Bhattarai, and daughter Jaslyn Bhattarai for their love, support, and encouragement without which this entire degree would not have been possible. My life is beautiful all because of them.

Finally, I would like to thank University of Missouri–St. Louis, Department of Chemistry and Biochemistry, and Center for Nanoscience for providing me the platform for my better future by accepting me as a graduate student.

TABLE OF CONTENTS

ABSTRACT.....	iv
DEDICATION.....	vi
ACKNOWLEDGEMENT	vii
TABLE OF CONTENTS.....	ix
LIST OF ABBREVIATIONS.....	xiii
LIST OF FIGURE.....	xv
LIST OF TABLES.....	xxiv
CHAPTER 1 GENERAL INTRODUCTION	1
1.1 Biosensors	1
1.2 Electrochemical Biosensor.....	4
1.2.1 Voltammetry	5
1.2.2 Electrochemical impedance spectroscopy	7
1.3 Optical Biosensor	9
1.3.1 Surface plasmon polariton	10
1.3.2 Localized surface plasmon resonance.....	13
1.3.3 Thermal and Piezoelectric Biosensors	15
1.4 Nanostructured Transducers.....	16
1.4.1 Nanostructures	16
1.4.2 Nanostructures as transducers.....	18

1.5	Modification of Transducer Surface	19
1.5.1	Self-assembled monolayers (SAMs).....	19
1.5.2	Protein immobilization.....	21
1.6	References	27
CHAPTER 2 MATERIALS AND METHODS		33
2.1	Materials.....	33
2.2	Preparation of Nanoporous Gold (NPG).....	34
2.2.1	Preparation of NPG on gold wire.....	34
2.2.2	Preparation of NPG on flat gold plate.....	35
2.3	Electrochemical Annealing of Nanoporous Gold Wire	36
2.4	Preparation of Nanostructured Gold and Silver Films	36
2.5	Surface Modification with Organic and Biological Molecules.....	36
2.5.1	Preparation of self-assembled monolayers (SAMs)	37
2.5.2	Covalent immobilization of proteins on SAMs	37
2.5.3	Bioaffinity immobilization of proteins	37
2.6	Localized Surface Plasmon Resonance Spectroscopy	38
2.7	Electrochemical Characterization	39
2.7.1	Cyclic voltammetry (CV)	39
2.7.2	Electrochemical impedance spectroscopy (EIS).....	40
2.7.3	Square wave voltammetry (SWV)	40

2.8	Scanning Electron Microscopy (SEM)	40
2.9	Electrocatalytic oxidation of glucose on NPG wire	41
2.10	References	42
CHAPTER 3 PREPARATION, MODIFICATION AND APPLICATION OF NANOPOROUS GOLD		43
3.1	Introduction	43
3.2	Results and Discussion.....	46
3.2.1	Fabrication of NPG on gold wire.....	46
3.2.2	Fabrication of NPG on flat gold.....	52
3.2.3	Post-modification of NPG-coated gold wire.....	58
3.2.4	Application of NPG	69
3.3	Conclusions	92
3.4	References	93
CHAPTER 4 FABRICATION OF NANOSTRUCTURED GOLD FILM FOR THE STUDY OF BIOMOLECULAR INTERACTIONS USING LSPR SPECTROSCOPY. 97		
4.1	Introduction	97
4.2	Results and Discussions	103
4.2.1	Nanostructured gold film (NGF) Preparation	103
4.2.2	Refractive index sensitivity (RIS) test	107
4.2.3	Biosensing.....	111

4.2.4	Regeneration of NGF	121
4.3	Conclusions	124
4.4	References	125
CHAPTER 5 REFRACTIVE INDEX SENSITIVITY OF NANOSTRUCTURED SILVER FILM, AND COMPARISON TO GOLD NANOSTRUCTURES.....		130
5.1	Introduction	130
5.2	Result and Discussion	132
5.2.1	Refractive index sensitivity of NSF	134
5.2.2	Comparison of RIS of silver and gold nanostructure.....	136
5.3	Conclusions	138
5.4	Reference.....	139

LIST OF ABBREVIATIONS

BSA	Bovine serum albumin
CEA	Carcinoembryonic antigen
Con A	Concanavalin A
CV	Cyclic voltammetry
EDX	Energy dispersive X-ray spectrometer
EIS	Electrochemical impedance spectroscopy
FOM	Figure of merit
FWHM	Full width at half maximum
GW	Gold wire
LPA	Lipoic acid
LSPR	Localized surface plasmon resonance
MDDA	12-Mercaptododecanoic acid
MUA	11-Mercaptoundecanoic acid
NGF	Nanostructured gold film

nm	Nanometer
NPG	Nanoporous gold
NSF	Nanostructured silver film
PAMAM	Poly(amido amine)
RIS	Refractive index sensitivity
RIU	Refractive index unit
SAM	Self-assembled monolayer
SEM	Scanning electron microscopy
SPP	Surface plasmon polariton
SPR	Surface plasmon resonance
SWV	Square wave voltammetry
TEG (HO-PEG ₂ -SH)	8-Mercapto-3,6-dioxaoctanol

LIST OF FIGURE

Figure 1.1 Schematic diagram of a typical biosensor.	1
Figure 1.2 Photographic image of typical setup of three-electrode cell showing arrangement of the electrodes in a three-necked pear-shaped flask.	5
Figure 1.3 (A) Triangular potential waveform of cyclic voltammetry and (B) cyclic voltammogram for redox active species. ²²	6
Figure 1.4 Schematic illustrations of (A) sandwich type immunosensor and (B) color corresponding Nyquist plots obtain from EIS. The Nyquist plots are color coded to show a typical shift of the Nyquist plot after each binding event.	8
Figure 1.5 Most frequently used setup (Kretschmann configuration) for a SPP-based biosensor working as a immunosensor.....	12
Figure 1.6 Schematic diagram illustrating localized surface plasmon resonance.	13
Figure 1.7 Photographic image of setup of typical reflection based LSPR spectroscopy.	15
Figure 1.8 Schematic depiction of an ideal SAM formed on a gold substrate.	20
Figure 1.9 Schematic diagram of protein immobilization techniques.	22
Figure 1.10 Covalent protein immobilization mechanisms via EDC/NHS coupling	24
Figure 3.1 SEM image of an NPG plate prepared by dealloying commercially available 10K white gold in concentrated nitric acid for 48 h.....	43
Figure 3.2 Cartoon showing applications of NPG in different fields.	44
Figure 3.3 Schematic diagram of wet chemical method of preparing NPG.	45
Figure 3.4 Schematic of electrochemical method of preparing NPG on gold wire.....	46
Figure 3.5 Cyclic voltammograms of NPG-coated gold wires prepared by applying different deposition potentials.	47

Figure 3.6 Low-magnification SEM images of NPG-coated gold wires prepared at (A) -1.0 V, (B) -1.2 V and (C) -1.6 V for 10 min showing change in morphological features with changing potential. Scale bar: $5\text{ }\mu\text{m}$. (A'), (B') and (C') are the low-magnification cross sectional of (A), (B) and (C), respectively, showing change in thickness. Scale bar: $20\text{ }\mu\text{m}$.	48
Figure 3.7 EDX elemental analysis of an NPG-coated gold wire shows only the presence of gold after dealloying	49
Figure 3.8 CV of NPG-coated gold wires prepared at different (A) ratio of Au and Ag solution for 10 min and (B) deposition time with Au ₃₀ Ag ₇₀ ratio, deposition potential = -1.2 V	50
Figure 3.9 Increase in thickness of NPG-coated gold wires with the deposition time. (A) 10 min and (A') 20 min at deposition potential -1.0 V, and (B) 1 min and (B') 4 min at -1.4 V. Scale bar: $20\text{ }\mu\text{m}$.	51
Figure 3.10 SEM images of electrochemically prepared NPG films after Au ₃₀ Ag ₇₀ alloying at -1.2 V and dealloying at (A) $+1.0$ V, (B) $+1.2$ V, and (C) $+1.4$ V in KNO ₃ for 1 min. Scale bar: 200 nm . (A'), (B') and (C') are the corresponding EDX spectra showing changing Au to Ag ratio with changing potential.	54
Figure 3.11 (A–C) SEM images of NPG films prepared by electrochemical dealloying for 1 min, 6 min and 12 min, and (D) NPG plate prepared by nitric acid dealloying of commercially available alloy plate for 48 h. Scale bar: 200 nm .	55
Figure 3.12 Reflection spectra of electrochemically prepared NPG films using a dealloying potential of $+1.0$ V (vs. Ag/AgCl, satd. KCl) for different dealloying times.	56

Figure 3.13 Bulk RIS test of the NPG film prepared using alloying deposition potential of -1.2 V for 1 min and dealloying potential of $+1.0$ V for 1 min. (A) LSPR spectra obtained at different RI, 1, 1.33, 1.36, and 1.495 using air, water, ethanol, and toluene respectively, represented by lines of different colors. (B) Plot of peak wavelength versus RI showing linear dependence.	57
Figure 3.14 SEM images of NPG plate prepared by dealloying for (A) 48 h and (B) 42 days showing change in width of gaps and ligaments. Scale bar: 500 nm.....	59
Figure 3.15 Cyclic voltammograms used to determine gold surface area by oxide formation and reduction for NPG annealed in: (A) 0.1 M NaClO_4 and (B) 0.1 M NaNO_3 for 50 oxidation–reduction cycles, shown after every 5 cycle, (C) similar CV scans shown for annealing of NPG performed for 30 cycles in 0.1 M KCl , with data shown after every fifth cycle. (D) The CV scans recorded during application of the 30 annealing cycles in 0.1 M KCl . Scan rate = 100 mV s^{-1}	63
Figure 3.16 Surface area reduction after annealing in different electrolyte solutions using	64
Figure 3.17 SEM images of NPG (A) unannealed (B–D) annealed, in KCl for 30 cycles, in NaNO_3 for 50 cycles and in NaClO_4 for 50 cycles, respectively. Scale bars: 200 nm.....	65
Figure 3.18 Interligament gap (A–D) and ligament width (A'–D') of nanoporous gold before (A and A') and after annealing under different solutions (B–D').....	66
Figure 3.19 (A) Cyclic voltammograms for the determination of electrochemically accessible surface area, and (B,C) cathodic and anodic peak current versus the	

square root of the scan rate of flat gold wire showing linear dependency. The scans were from +0.6 to −0.2 V in 10 mM $K_3[Fe(CN)_6]$	68
Figure 3.20 SEM micrograph of NPG wire half dipped in 1 mg mL ^{−1} BSA solution for 5 min (A) color contrast showing no protein immobilized (bright) and physically immobilized BSA (dark). (B) High-magnification SEM image near the boundary of protein immobilized and non-immobilized region. (C) and (D) are low-magnification images of cross-section and top view of protein immobilized region showing BSA layers.....	72
Figure 3.21 High-magnification SEM images of (A) NPG not dipped in protein solution and (B) and (C) NPG and flat gold wire, respectively, dipped in 1 mg mL ^{−1} BSA solution. Scale bar: 200 nm. (A') and (B') are SEM images corresponding to (A) and (B) with scale bar 100 nm. Image with scale bar of 100 nm with better resolution cannot be obtained for BSA on flat gold.....	73
Figure 3.22 SEM images of NPG after immobilization of different concentration of BSA on surface for 5 min (A) 1 mg mL ^{−1} (B) 0.1 mg mL ^{−1} , and (C) 0.01 mg mL ^{−1} . Scale bar: 200 nm. (A'), (B') and (C') are the corresponding images of (A), (B) and (C) with scale bar: 100 nm.	74
Figure 3.23 (A) Comparison of initial LSPR peak positions of different NPG samples prepared under the same conditions from the same solution bath. (B) LSPR spectra of LPA functionalized NPG (red) and after interaction with BSA (blue) clearly showing red shift in peak wavelength and increase in intensity of 1/reflection.....	76

Figure 3.24 The schematic diagram of the electrode modification steps used to perform bioassays on an NPG wire. The NPG was first modified with LPA SAMs onto which either glycoprotein or lectin–enzyme conjugate was immobilized, and finally different types of assays were performed.	77
Figure 3.25 Square-wave voltammograms of Con A–ALP conjugate immobilized on gold wire and NPG using LPA SAMs. SWV were recorded with 1 mM p-APP in glycine buffer (pH 9.0, 100 mM) after 2 min incubation with the substrate p-APP.....	79
Figure 3.26 Square wave voltammogram of NPG wire after immobilizing Con A–ALP conjugates using different SAMs (1) LPA, (2) MDDA, (3) a 1:5 mixed SAM of MDDA and mercaptooctanol (HO-C8-SH), and (4) a 1:5 mixed SAM of MDDA and 3,6-dioxa-8-mercaptooctanol (PEG3-SH).....	80
Figure 3.27 Peak current vs. p-APP concentrations of the Con A–ALP conjugate immobilized on LPA fitted to the Michaelis–Menten equation.	84
Figure 3.28 Kinetic ELLA response on NPG. Different concentrations of (A) IgG and (B) transferrin were incubated for 2 h in PBS (pH 7.4) with Con A–ALP conjugate immobilized on LPA modified NPG and the difference in peak current before and after incubation was plotted to obtain the response plot.	85
Figure 3.29 Bar plot for SWV response due to Con A–ALP conjugate binding to different glycoproteins on NPG. Glycoproteins were immobilized on NPG and incubated with 50 $\mu\text{g mL}^{-1}$ conjugate for 24 h and then incubated with 1 mM p-APP for 2 min.	88

Figure 3.30 CV of FGW and NPG in 0.1 M NaOH solution (black) and 5 mM glucose in 0.1M NaOH solution (red). Green CV of NPG represents scanning up to 0.2 V in 5 mM glucose in 0.1M M NaOH solution. Scan rate: 100 mV s ⁻¹	90
Figure 3.31 CV of NPG when scanned up to 0.2 V in 5 mM glucose in 0.1M M NaOH solution at three subsequent scans. Scan rate: 100 mV s ⁻¹	91
Figure 3.32 CV of FGW and NPG in 5 mM glucose in 0.1M NaOH solution under multiscan (number of scans indicated). Scan rate: 100 mV s ⁻¹	91
Figure 4.1 Schematic depiction of (A) nanostructured gold film fabrication steps (B) electrochemical setup for nanostructured gold film fabrication and (C) optical setup for localized surface plasmon resonance spectroscopy (reflection mode).	104
Figure 4.2 Photographic images of (A) flat gold surface on glass slide before stripping off of silicon wafer and (B) showing changes on gold surface before and after electrodeposition.	105
Figure 4.3 (A) Chronoamperometric curves obtained during the preparation of NGFs by applying different potentials and times (indicated). (B) LSPR spectrum of corresponding NGFs recorded in a nitrogen environment.	106
Figure 4.4 SEM images of NGFs prepared using (A,B) one-step chronoamperometry technique, -1.2 V for 60 s and -1.2 V for 90 s, respectively and (C–E) two-step chronoamperometry technique, -1.2 V for 60 s followed by -1.0 V for 30 s, -1.2 V for 60 s followed by -1.4 V for 30 s, and -1.2 V for 60 s followed by -1.6 V for 30 s, respectively. Scale bar: 2 μm. Insets are the corresponding high-magnification SEM images. Scale Bar: 0.2 μm.....	107

Figure 4.5 (A) Bulk refractive index response of nanostructured gold films prepared using electrodeposition conditions of -1.2 V for 60 s, and then -1.6 V for 30 s. LSPR spectra obtained at different refractive indices (n) = 1, 1.33, 1.35, 1.37, 1.39, 1.41, and 1.43 in nitrogen, water, 15, 30, 45, 60, and 75% glycerol, respectively. The nitrogen peak is the lowest and the peaks move upward in the graph with increasing refractive index. (B) Plot of peak wavelength versus refractive index for the spectra shown in (A). (C) LSPR spectra showing the bulk RIS response at the same series of refractive index values for nanostructured gold film prepared using electrodeposition at -1.2 V for 90 s. (D) Plot of peak wavelength versus refractive index for the spectra shown in (C)..... 109

Figure 4.6 Schematic diagram of binding of Concanavalin A to thiolated mannoside immobilized on NGF surface. 112

Figure 4.7 LSPR spectra of NGF, unmodified (black), modified with mixed SAMs of α Man-C8-SH and TEG-SH prepared from 1:3 solution molar ratio (1 mM total concentration in ethanol, 2 h (red) and after immobilization of $0.5 \mu\text{M}$ proteins for 1 h (green) (A) Concanavalin A and (B) bovine serum albumin. 113

Figure 4.8 Nyquist diagram (Z' vs. Z'') for Faradic impedance measurement of NGF in 10 mM PBS buffer pH 7.4 containing 5 mM $\text{K}_3[\text{Fe}(\text{CN})_6]/\text{K}_4[\text{Fe}(\text{CN})_6]$ (1:1 mixture), unmodified (black), modified by mixed SAMs (red), and after Con A immobilization (green). The impedance spectra were recorded within frequency range of 100 kHz to 0.1 Hz. Inset is equivalent circuit used to model

impedance data. The panel on the right shows an expanded view of the high-frequency data for the bare NGF and the SAM-modified NGF.....	114
Figure 4.9 (A) Plot of the inverse of the percent reflectance at the peak wavelength versus bulk refractive index for the nanostructured gold film prepared at -1.2 V for 60 s	116
Figure 4.10 (A) Con A binding kinetics curves obtained for different concentration of Con A (indicated). The regression plots of the curves (cyan color) was obtained by fitting the built-in equation for exponential rise to maxima to obtain values of $1/\tau$. (B) Determination of the binding affinity of Con A to a mannose SAM by plotting $1/\tau$ vs. different concentration of Con A.	117
Figure 4.11 Schematic diagram of the technique applied for the detection of CEA using NGF.	119
Figure 4.12 (A) LSPR spectra of NGF showing shift by 17 nm on covalent immobilization of Con A on SAMs of 11-mercaptoundecanoic acid (MUA). (B) LSPR spectra shift by 23 nm on interaction of CEA to Con A immobilized as in (A).	120
Figure 4.13 LSPR spectra of multi-layer of biomolecules formed on NGF surface: LSPR spectra of (black) blank NGF, (red) MDDA SAMs formed on NGF, (green) immobilized PAMAM dendrimers-G5 on SAM, and (blue) immobilized mannose first formed on G5 followed by Con A on mannose . Spectra were obtained in a nitrogen environment.	122
Figure 4.14 Experiments performed to compare freshly prepared and regenerated NGF. (A) LSPR spectra of freshly prepared NGF (black) and regenerated NGF (blue)	

in a N₂ environment. (B) cyclic voltammograms of freshly prepared NGF (black), SAM immobilized NGF (red), Con A immobilized NGF (green), and regenerated NGF (blue) showing very less difference between regenerated and the freshly prepared NGF. (C) SEM image of NGF after regeneration step showing no distinct difference than that of the freshly prepared NGF.... 123

Figure 5.1 Schematic diagram of NSF preparation steps. 133

Figure 5.2 LSPR spectra of NSF prepared by applying a deposition potential of -1.2 V for different times (as indicated). 134

Figure 5.3 (A) LSPR spectra obtained when solutions of different refractive index were passed over the NSF surface prepared by depositing silver for 1 min by applying a -1.2 V potential. (B) A linear fit line is obtained when peak wavelength is plotted vs. refractive index, the slope of which gives the bulk RIS of the nanostructure and is equal to 186 ± 6 nm/RIU. 135

Figure 5.4 Comparison of bulk RIS of NSF prepared by applying -1.2 V for different deposition times (30 s, 60 s, 90 s, and 150 s). 136

Figure 5.5 SEM images of NSF prepared by applying (A) -1.2 V and (B) -1.4 V potential for 1 min of deposition time. The images from left to right are in order of increasing magnification (scale bars: 2 μ m, 0.5 μ m, 0.2 μ m, respectively). 137

LIST OF TABLES

Table 1.1 Classification of biosensors according to the type of transducer used	3
Table 1.2 Classification of nanostructures on the basis of dimensions	18
Table 3.1 Surface area comparison of NPG-coated gold wires under different conditions.	52
Table 3.2 Comparison of RIS of NPG films formed on flat gold surface at 1 min of deposition and dealloying time.....	58
Table 3.3 Surface areas determined by both oxide stripping and use of a diffusing redox probe for the NPG-coated gold wire, annealed NPG-coated gold wire, and bare gold wire electrodes.....	69
Table 3.4 Surface coverage of proteins on NPG.....	82
Table 4.1 Sensitivity of NGF prepared under different conditions.	110

CHAPTER 1 GENERAL INTRODUCTION

1.1 Biosensors

According to IUPAC, “a biosensor is device that uses specific biochemical reactions mediated by isolated enzymes, immunosystems, tissues, organelles or whole cells to detect chemical compounds usually by electrical, thermal or optical signals”.¹

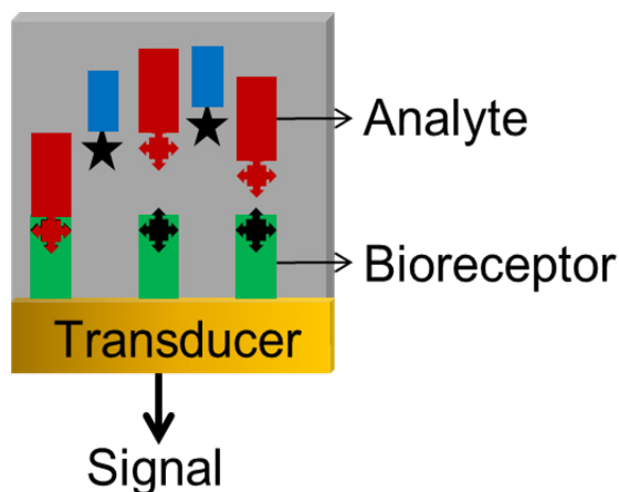


Figure 1.1 Schematic diagram of a typical biosensor.

A typical biosensor consists of bioreceptor, transducer, and detector,² as shown in **Figure 1.1**. Bioreceptors are biochemical recognition systems attached or kept in proximity to the surface of the transducer whereas the transducer transforms the biochemical response into the measurable signal which is then detected by the detector. The first biosensor reported was an amperometric enzyme electrode for glucose detection in 1962 by Clark and Lyons.³ Since then, much effort have been made to commercialize biosensors, but did not succeed until 1975 when Yellow Springs Instruments Company released the first glucose sensor system.⁴ Medisense Inc. became the first company to release a personal glucose meter in 1987.⁵ The first optical biosensor was published in the

early 1980s. Research on biosensors and their commercialization has been growing each year, which is evident from the increasing number of publications. Two of the commercially successful biosensors include a pregnancy test kit which detects human chorionic gonadotropin (hCG) protein in urine and glucose monitoring kits for diabetic patients which monitor the glucose level in blood.⁶⁻⁷

Biosensors have applications in wide variety of fields besides medical diagnostics and toxicology tests. They can be used in general industries, to monitor environmental pollution, for forensics and crime detection and to understand the interaction between biomolecules.⁸⁻¹¹ The ideal biosensors should be highly specific to analyte; independent of stirring, pH, and temperature; biocompatible; cheap; easy to use; and durable. It should also be capable to detect small sample volume rapidly and accurately.¹²⁻¹³ It is, however, difficult to prepare an ideal biosensor, and researchers are mainly focusing on preparing biosensor containing many of the above-mentioned properties.

Biosensors can be classified according to either the type of bioreceptors used or the transduction method used.¹⁴ The most common types of bioreceptors used in biosensors include enzymes, antibodies, nucleic acids, proteins, microorganisms, and cells. The most popular among these are the enzymatic biosensors because of the specificity of a well-chosen enzyme toward the analyte and its catalytic activity. Including early biosensors, most glucose monitoring biosensors use the enzyme glucose oxidase (GOx) which can catalyze the oxidation of glucose into gluconic acid and hydrogen peroxide.³⁻⁴ Other commonly used enzymes include oxidoreductase, transferase, and hydrolases. The performance of enzyme-based biosensors not only depends on a suitable substrate, pH, temperature, and cofactors but also depend on the

methods of enzyme immobilization on the substrate.⁴ The biosensors based on antibodies are called immunosensors and are useful in studying different types of antibody–antigen interactions.¹⁵ Immunosensors are a valuable tool for detecting cancer biomarkers (e.g., prostate specific antigen and carcinoembryonic antigen), cancer cells, bacteria, virus, etc.¹⁵ The other emerging biosensors are nucleic acid-based biosensors called genosensors where natural and biomimetic forms of oligo- and polynucleotides, including, aptamers of DNA or RNA are used as bioreceptors with or without labeling if the target nucleic acid sequence is known.¹⁶ The potential applications of genosensors include gene analysis, clinical diagnostics, forensic study, and medical applications.¹⁶⁻¹⁷

Biosensors can be divided based on transduction methods into optical, electrochemical, thermal, and piezoelectric which are summarized on **Table 1.1**.^{14, 18}

Table 1.1 Classification of biosensors according to the type of transducer used.

Transducers	Technique
Electrochemical	Voltammetry, Impedometry, Potentiometry, Amperometry, Conductometry
Optical	Surface and localized plasmon resonance, Absorbance, Fluorescence, Ellipsometry, Surface enhanced Raman spectroscopy
Thermal	Calorimetry
Mass (piezoelectric)	Crystal microbalance, Surface acoustic wave

1.2 Electrochemical Biosensor

Electrochemical biosensors are popular because of their ability to detect small sample volumes, low-cost, and simplicity of usage. The other advantage of the electrochemical biosensors is that they can be performed in colored or turbid samples without any interference such as in the case of detecting analytes within blood samples.¹⁹

In electrochemical biosensors, bioreceptors selectively react with the target analyte and produces an electrical signal in the form of current (amperes) and/or potential (volts) and/or impedance (ohms) which can then be measured using different approaches, including voltammetric, potentiometric, amperometric, conductometric, and impedimetric methods.²⁰ The amount of signal produced is related to the concentration of the analyte reacting with bioreceptors. The electrochemical biosensors can further be divided into biocatalytic devices and affinity sensors, depending on the nature of biological recognition process.²⁰ Biocatalytic devices produce measurable electroactive species on analyte recognition e.g. glucose and lactose detection, whereas affinity sensors produce electroactive signals by selectively binding the analyte to the bioreceptor e.g., antigen/antibody interaction and DNA hybridization.

An electrochemical biosensor consists of two or three electrodes first dipped into a supporting electrolyte.²¹ Analyte can be mixed with the supporting electrolyte or can be added later depending on the experiment performed. A typical three-electrode electrochemical cell consists of (1) reference electrode, usually silver/silver chloride (KCl sat.) (0.22 V vs. SHE, standard hydrogen electrode); (2) counter or auxiliary electrode, made up of platinum wire (99.997% purity); and (3) working electrode, which is conductive and chemically stable such as platinum, gold, or carbon. Photograph of a

typical three-electrode cell is shown in **Figure 1.2**, showing three alligator clips holding three different electrodes.

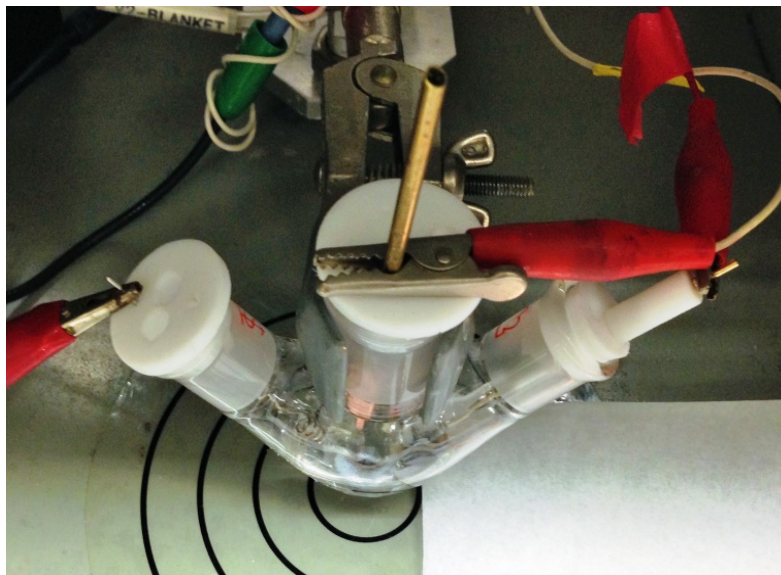


Figure 1.2 Photographic image of typical setup of three-electrode cell showing arrangement of the electrodes in a three-necked pear-shaped flask.

1.2.1 Voltammetry

Voltammetry is useful for quantification of low-level samples where a potential is applied to the working electrode versus a reference electrode and current is measured versus a counter-electrode.²⁰ In this technique, the potential is scanned over a set potential range while recording the current as a peak or plateau which is proportional to the concentration of analyte. The common voltammetry methods include linear sweep voltammetry, cyclic voltammetry, square wave voltammetry, differential pulse voltammetry, polarography, etc.

Cyclic voltammetry (CV) is one of the most commonly used electroanalytical techniques for the study of electroactive species. It is normally performed without stirring

the analyte solution. In this technique, the potential is linearly scanned to a certain point and scanned back to the starting point making a triangular waveform, as shown in **Figure 1.3A,B**.²² If a redox reaction occurs under such conditions, anodic and cathodic current peaks can be obtained when current is plotted versus potential, also called a voltammogram. The anodic peak current (i_{pa}), cathodic peak current (i_{pc}), anodic peak potential (E_{pa}) and cathodic peak potential (E_{pc}) are characteristic of types of reactions and concentration of analyte.²²

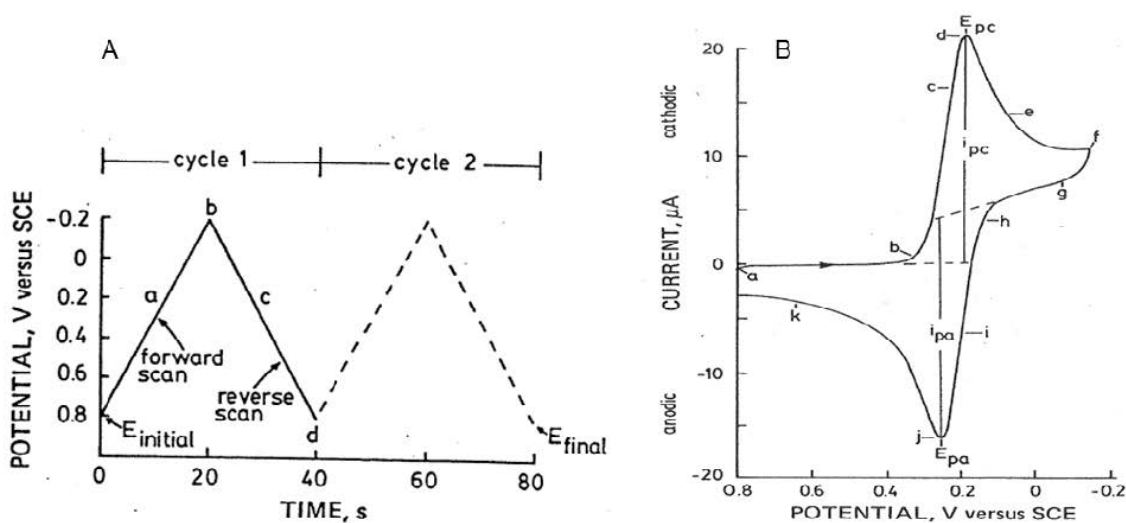


Figure 1.3 (A) Triangular potential waveform of cyclic voltammetry and (B) cyclic voltammogram for redox active species.²²

If both the species in redox couple can rapidly exchange electrons with the working electrode, they are called an electrochemically reversible couple whose formal reduction potential (E^0) can be obtained by

$$E^0 = (E_{pa} + E_{pc})/2 \quad (1.1)$$

whereas the number of electrons transferred can be determined by

$$\Delta E = (E_{pa} - E_{pc}) \approx 0.059/n \quad (1.2)$$

The peak current (i_p) can be obtained using Randles–Sevcik equation:

$$i_p = (2.69 \times 10^5) n^{3/2} A D^{1/2} C \nu^{1/2} \quad (1.3)$$

where n is the electron stoichiometry, A is surface area of electrode (cm^2), D is diffusion coefficient ($\text{cm}^2 \text{s}^{-1}$) of the electroactive species, C is concentration (mol cm^{-3}), and ν is scan rate (V s^{-1}) with the value of i_{pa} being equal to i_{pc} , so

$$i_{pa}/i_{pc} = 1 \quad (1.4)$$

If there is a slow electrons exchange between the redox species with the working electrode surface, those redox couple is called an electrochemically irreversible couple which causes increase in peak potential separation and all the above equations are not exactly applicable in this case.²²

1.2.2 Electrochemical impedance spectroscopy

Electrochemical impedance spectroscopy (EIS) is another very sensitive technique which can be used for biosensing.²³ This technique measures the resistive and capacitive properties of materials by applying a small alternating sinusoidal potential, typically 2–10 mV. An impedance spectrum is obtained by varying the frequency over a wide range and most commonly expressing in the form of a Nyquist plot.²⁴

If the applied sinusoidal potential $E(t) = E_0 \sin(\omega t)$, the response current $I(t) = I_0 \sin(\omega t - \phi)$, where E_0 and I_0 are the amplitudes of potential and current respectively and ϕ is the phase angle difference between current and potential. Then the impedance of the system is defined by eq 1.5:²⁵

$$Z(t) = \frac{E(t)}{I(t)} = \frac{E_0 \sin(\omega t)}{I_0 \sin(\omega t + \phi)} = Z_0 \frac{\sin(\omega t)}{\sin(\omega t + \phi)} \quad (1.5)$$

From Euler's theorem:

$$Z(\omega) = \frac{E}{I} = |Z|e^{j\phi} = Z_0(\cos\phi + j\sin\phi) = Z' + jZ'' \quad (1.6)$$

where $j = (-1)^{1/2}$, and Z' and Z'' are real and imaginary impedance respectively.

EIS becomes handy mainly to study affinity-based biosensors, such as studying antibody (Ab)–antigen (Ag) binding, on the electrode surface.²⁶ The schematic diagram of typical Ab–Ag interactions that can be studied through EIS is shown in **Figure 1.4A** and the corresponding typical Nyquist plots in **Figure 1.4B**. The increase in real and imaginary components of Nyquist plots is directly proportional to the concentration of the analyte present in the electrode surface. Using nanostructured materials for impedance-based biosensor is advantageous because of increased electrode surface area, improved electrical conductivity on sensing interface, and easy accessibility to the analyte.

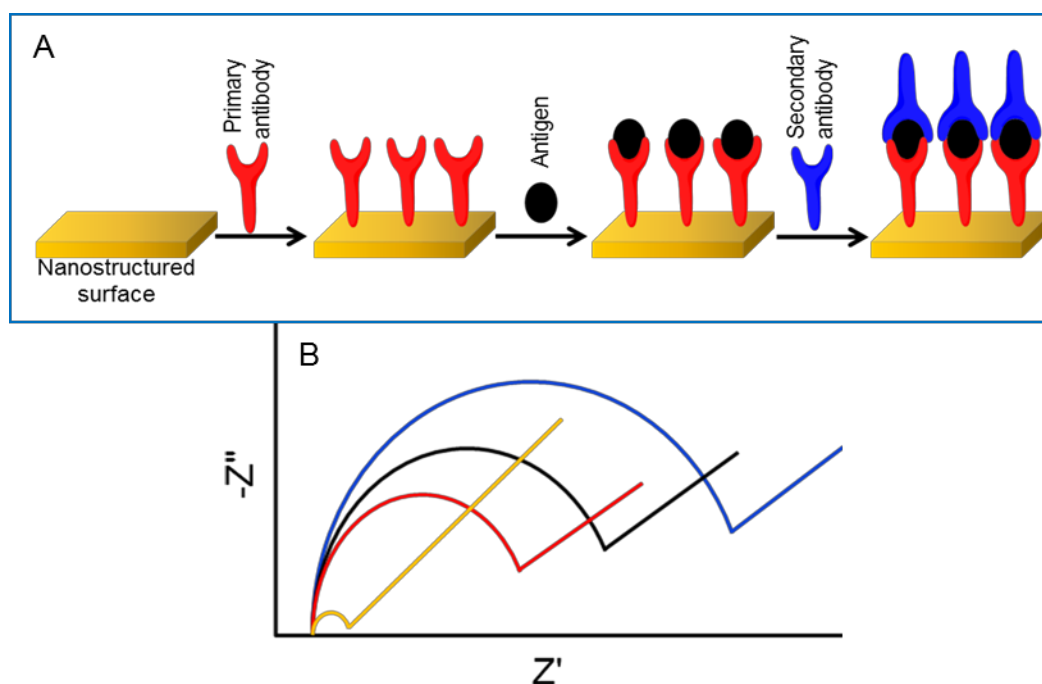


Figure 1.4 Schematic illustrations of (A) sandwich type immunosensor and (B) color corresponding Nyquist plots obtain from EIS. The Nyquist plots are color coded to show a typical shift of the Nyquist plot after each binding event.

1.3 Optical Biosensor

An optical biosensor is another commonly used biosensor technique for biomolecules detection and analysis. The advantages of optical biosensors are that they are immune to electromagnetic interference and can perform remote sensing and high-throughput detection.²⁷ Optical biosensing can be performed either by labeling or without labeling of biomolecules. Fluorescence labeling is the commonly used labeling technique where either target molecules or bioreceptor molecules are labeled with fluorophores.²⁸ The fluorescence-based detection is a very sensitive technique; however, fluorescent dyes can interfere with the interaction of target molecules and bioreceptor. Besides this effect, labeling of the molecules is laborious and precise location of fluorophores on each molecule cannot usually be controlled, making it an unsuitable technique for many quantitative analysis.²⁷ To avoid this labeling problem, label-free detection can be performed where the molecules can be detected in their natural form. This technique is easy to perform, cheap, and quantitative analysis and kinetic measurement of the interaction of molecules can also be performed. Optical biosensors are based on different spectroscopic techniques, e.g., absorption, reflection, ellipsometry, fluorescence, phosphorescence, propagating surface plasmon resonance, localized surface plasmon resonance, Raman, surface enhanced Raman spectroscopy, refraction, and dispersion spectrometry, which records different spectrochemical properties such as amplitude, energy, polarization, decay time, and phase.¹⁸ One of the commonly measured properties is phase. When electromagnetic radiation is exposed to the biomolecules, the phase of the radiation is changed depending on the refractive index (RI) of the analyte. Surface plasmon resonance-based spectroscopy is one of the techniques based on the change in

RI and hence to the phase. Two popular surface plasmon-based optical biosensor includes propagating surface plasmon or surface plasmon polariton²⁹ and localized surface plasmon resonance spectroscopy³⁰.

1.3.1 Surface plasmon polariton

Propagating surface plasmon or surface plasmon polariton (SPP) spectroscopy-based biosensor is popular for studying the affinity-based interactions of the biomolecules such as protein–protein interactions, label-free immunoassay, enzyme–substrate interactions, DNA hybridization, diagnosis of virus induced diseases, and many more.³¹

Surface plasmons present at metal–dielectric interfaces having dielectric constants of opposite signs can be excited using light waves giving rise to surface plasmon polariton. The propagation constant of a surface plasmon (β_{sp}) at interface of metal–dielectric can be expressed as³²

$$\beta_{sp} = \frac{\omega}{c} \sqrt{\frac{\epsilon_d \epsilon_m}{\epsilon_d + \epsilon_m}} = \frac{2\pi}{\lambda} \sqrt{\frac{\epsilon_d \epsilon_m}{\epsilon_d + \epsilon_m}} \quad (1.7)$$

where ω is the angular frequency, c is the speed of light in vacuum, λ is wavelength of light in vacuum, and $\epsilon_d (= \epsilon_d' + i\epsilon_d'')$ and $\epsilon_m (= \epsilon_m' + i\epsilon_m'')$ are dielectric functions of the dielectric and metal, respectively. Also, ϵ_d' and ϵ_d'' are real and imaginary part of ϵ_d whereas ϵ_m' and ϵ_m'' are real and imaginary part of ϵ_m . The surface plasmon polariton can be described by the above equation only when real part of ϵ_m is negative and $\epsilon_m < -\epsilon_d$ which can be fulfilled by many metals like gold, silver and aluminum in the visible and near IR regions of the spectrum.

One of the common types of setup for excitation of surface plasmons is using the Kretschmann configuration (**Figure 1.5**),³³ where an incident light wave propagating through a prism falls on the surface of the metal film at one face of the prism and is totally internally reflected generating the evanescent wave which penetrates the thin metal film. By controlling the angle of incidence, an evanescent wave which propagates along the interface with the propagation constant can be coupled to surface plasmon using the eq 1.8:³²

$$\frac{2\pi}{\lambda} n_p \sin(\theta) = \text{Re}(\beta_{sp}) \quad (1.8)$$

where θ denotes the angle of incidence, n_p denotes the RI of the prism and Re denotes real part of the complex number. When surface plasmon is excited, a small portion of incident light energy is transferred to surface plasmon slightly decreasing the intensity of the light wave.

In SPP, plasmons propagate along x and y axes at the metal–dielectric interface and decay evanescently along the z -axis.³⁰ Any interaction of the molecule of interest with the propagating plasmon leads to a shift in plasmonic resonance condition. In other words, any changes in RI at the surface of SPP supporting metal film changes the propagation constant, which through the coupling condition, changes properties of the light wave (e.g., angle of reflection, wavelength, intensity, and phase) and is expressed under three different measurement modes: (1) angle resolved, (2) wavelength shift, or (3) imaging.³⁰ In SPP-based biosensors, the first step is to immobilize biorecognition elements (bioreceptors) on the surface of a transducer film. When analyte molecules present in solution bind to the bioreceptor molecules, RI near the metal–dielectric interface increases, and can be measured optically. Any change in RI (Δn) is directly

proportional to surface concentration of the analyte molecule (Γ in g cm^{-2}) bound to bioreceptor on transducer surface which can be explained by³¹

$$\Delta n = \frac{dn}{dc} \frac{\Gamma}{h} \quad (1.9)$$

where $\frac{dn}{dc}$ denotes the increase in RI of the analyte molecules (typically $0.1\text{--}0.3 \text{ mL g}^{-1}$)

and h is the thickness of the transducer. SPP-based biosensing can be performed on one of the following formats (1) direct detection (2) sandwich detection, (3) competitive detection, and (4) inhibition detection depending on the binding property of the bioreceptor and the size, concentration, and purity of the analyte.³² **Figure 1.5** represents the schematic diagram of a SPP immunosensor based on the direct detection format wherein antibody (red Y shape) specific to the antigen (blue sphere) is first immobilized on the sensor surface and then antigen is passed across the antibody. The output spectra before and after capturing the antigen to sensor surface is represented by red and blue line respectively.

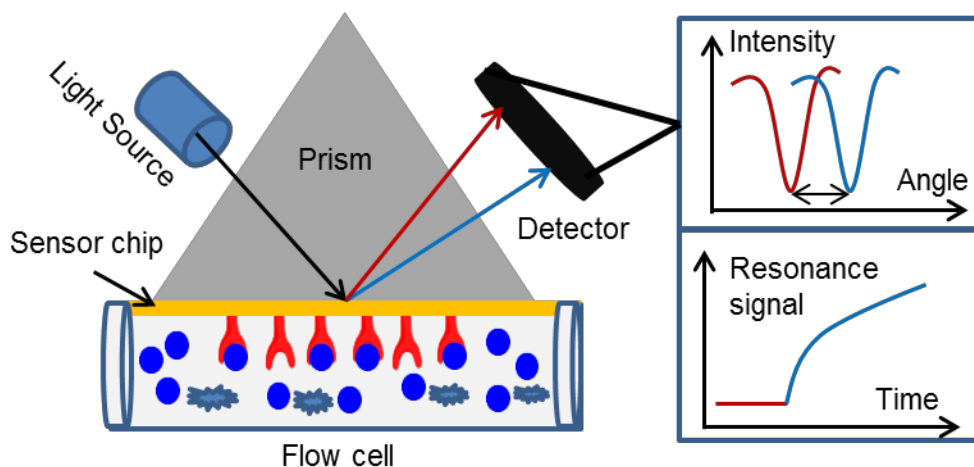


Figure 1.5 Most frequently used setup (Kretschmann configuration) for a SPP-based biosensor working as a immunosensor.

1.3.2 Localized surface plasmon resonance

When particles having size much smaller than the wavelength of incident light (nanostructures) interact with the light wave, the plasmons present on the surface of nanostructure start to oscillate locally around the nanostructure with the frequency called localized surface plasmon resonance (LSPR) (**Figure 1.6**).³⁰ LSPR-based biosensing is relatively new, but is a powerful technique in the field of biosensing. Scientists are exploring this technique because of its simplicity and possibility to be miniaturized, decreasing the cost. This technique is very sensitive and supports label-free real-time biosensing. Similar to SPP, LSPR-based biosensing also depends on the change in RI with output data commonly represented by measuring wavelength or intensity shift. LSPR-based biosensing, however, also depends on shape, size, and composition of the material used as a transducer.³⁴

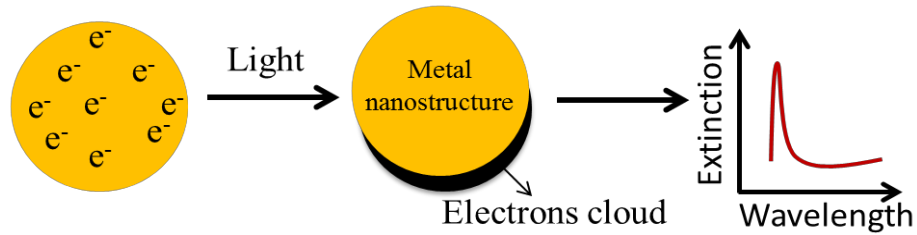


Figure 1.6 Schematic diagram illustrating localized surface plasmon resonance.

The LSPR extinction spectrum (E_λ) of the metal nanoparticles can be obtained by deriving Maxwell's equation.^{30,35} The first such derivation was performed by Gustav Mie for spherical particles in the early 20th century,

$$E_\lambda = \frac{18\pi\epsilon_A^{3/2}V}{\lambda} \left[\frac{\epsilon_i}{(\epsilon_r(\lambda) + \chi\epsilon_A)^2 + \epsilon_i(\lambda)^2} \right] \quad (1.10)$$

where V is the particle volume, χ is the shape factor (sphere = 2), ϵ_A is the external

(medium) dielectric constant, ε_r is real metal dielectric constant, and ε_i is imaginary metal dielectric constant. The value of χ can be analytically obtained for spheres and spheroids; however, for more complex geometries numerical modeling, such as discrete dipole approximation and finite-difference time-domain method, can be performed to get the extinction spectra.

The change in maximum wavelength of extinction spectra (λ_{\max}) depends on dielectric constant (ε) and hence to the RI (n) by $\varepsilon = n^2$. Hence, change in RI is related to the change in maximum wavelength by³⁰

$$\Delta\lambda_{\max} = m\Delta n[1 - \exp(-2d/l_d)] \quad (1.11)$$

where m is the bulk RI response, d is the thickness of the adsorbate layer, and l_d is electromagnetic field decay length. This relation is used for sensing biomolecules using LSPR-based technique.

There are three common approaches for the measurement of LSPR spectra (1) transmission mode, (2) reflection mode, and (3) dark field light scattering mode.³⁰ Depending on the transducer used, several methods can be applied. If the incident light can transmit through the nanostructure surface, the transmission mode can be used, but if light cannot be transmitted then a reflection-based mode should be used.³⁰ Transmission geometry shows wavelength as a maximum value in the extinction curve whereas the reflected geometry shows the wavelength as a minimum value which can be inverted to get a maximum value as in general extinction spectra. For the case of single nanoparticles or a system with small sample area, the dark field light scattering mode comes in handy.³⁶ **Figure 1.7** shows the photograph of the typical setup used in our lab for sensing biomolecules using reflection geometry. It consists of a light source attached to the fiber

optic probe containing a bundle of seven optical fibers with six illumination fibers around one readout fiber. The six illumination fibers guide the light toward the sample while readout fiber collects the reflected light from the sample. The signal from readout fiber is passed to spectrophotometer and finally to computer as LSPR spectra. Depending on the experiment, a nanostructured transducer can be placed inside flow cell or outside while adjusting the distance from the probe to the sample of around 4 mm.

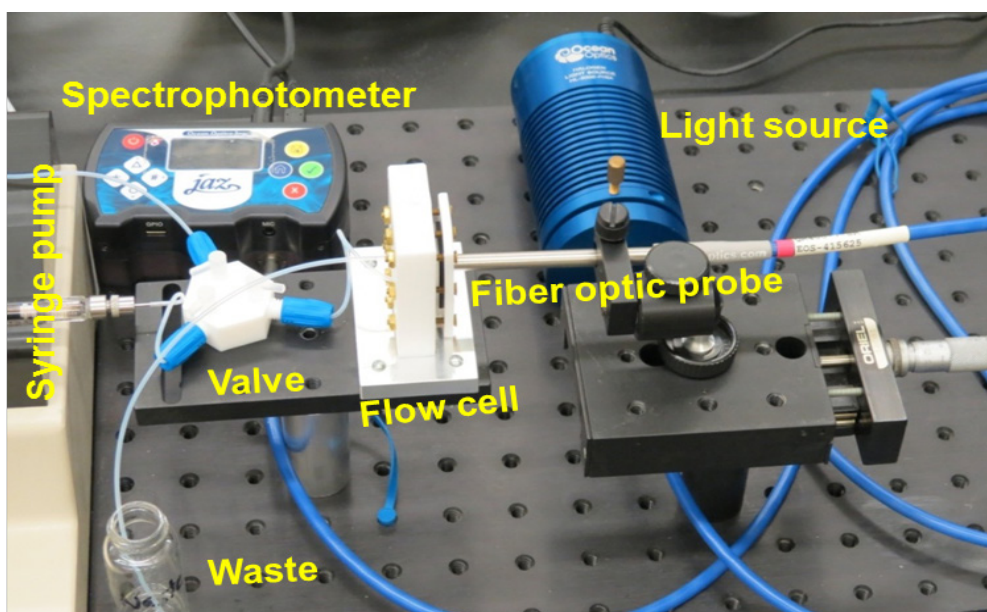


Figure 1.7 Photographic image of setup of typical reflection based LSPR spectroscopy.

1.3.3 Thermal and Piezoelectric Biosensors

Thermal and piezoelectric biosensors are less commonly used biosensors compared to electrochemical and optical biosensors. In thermal-based biosensors, when biomolecules immobilized on the sensor's surface come in contact with the analyte, a certain amount of heat is produced or absorbed which is proportional to analyte concentration.³⁷ A calorimetry is one of the commonly used thermal-based biosensor.³⁸

Piezoelectric biosensors are based on the change in mass of the transducer before and after the immobilization of analyte. A quartz crystal microbalance (QCM) is one of the commonly used techniques where a piezoelectric crystal, most commonly a quartz-crystal coated with a gold electrode, is made to vibrate at a particular frequency.³⁹ Depending on the increase in mass by interaction of the analyte to bioreceptor on surface, the resonance frequency of quartz crystal changes, which can be measured electrically and the amount of mass change can be determined.⁴⁰

1.4 Nanostructured Transducers

The role of transducer is imperative for biosensor regardless of the technique used. However, depending on technique different types of transducers are preferred. In this dissertation, we will be mainly focusing on transducers suitable for electrochemical and optical biosensor (surface plasmon based) while taking advantages of properties of the nanostructured surface.

1.4.1 Nanostructures

Nanostructures are strongly bound groups of atoms (10^3 to 10^9) with a definite shape having molecular weights 10^4 to 10^{10} daltons and at least one of the dimensions is 1 to 100 nm.⁴¹ They are of intense scientific interest due to their enhanced and novel properties compared to bulk materials some of which include high surface area-to-volume ratio, reactivity, sensing capability and increased mechanical strength.⁴²⁻⁴³ Because of their unique properties, nanostructures have application in diverse fields, including, but not limited to, biomedicine (drug delivery), energy (hydrogen storage, solar cell, and battery), optics (sensors), and electronics (computer chips, information



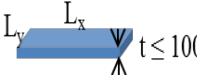
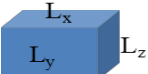
storage).⁴⁴⁻⁴⁵ However, different applications prefer nanostructures with different morphologies. Therefore, there is a need to explore and understand more about nanostructures to enhance their performance in various applications.

Nanostructures can be prepared in wide varieties of shapes. Nanotubes, nanowires, nanoparticles, quantum dots, nanocages, nanorods, nanocrystallites, nanocomposites, nanotriangles, nanopowders, nanorings, and nanostructured films are some of the examples of nanostructures.⁴⁶⁻⁴⁸ The most popular mode for classifying these nanostructures is according to the dimensions of the nanostructure that are not in a nanometric size range (>100 nm). According to this classification, nanostructures are classified into zero (0-D), one (1-D), two (2-D), and three (3-D) dimensions as shown in **Table 1.2**.⁴⁹ When all x , y , and z dimensions of nanostructure are in the nanoscale range, it is classified as 0-D. If one dimension is not in the nanoscale range it is called 1-D, if two dimensions are not in the nanoscale range, it is called 2-D and finally if none of the dimensions are in the nanoscale range, but the material possesses the nanocrystalline structure, it is called 3-D.

Common techniques for synthesizing nanostructures are wet chemical synthesis (colloidal, sol-gel),⁴⁶ vapor deposition (e.g., chemical and physical vapor deposition, sputter deposition, laser ablation, electric arc deposition),⁵⁰⁻⁵¹ mechanical (e.g., high-energy ball milling, melt mixing),⁵² and electrochemistry. Lithographic techniques (e.g., photolithography, electron beam lithography, nanosphere lithography) are one of other commonly used template-based techniques combined with vapor deposition to synthesize periodically controlled nanostructures.⁵³⁻⁵⁵ All of these techniques have their own advantages and shortcomings. Techniques like electron beam lithography can precisely

control the periodicity of the nanostructure, but it is time consuming, and the instrumentation is complex, costlier and needs expertise for operation. On the other hand, colloidal synthesis methods can synthesize a wide variety of nanostructures but give less control over the periodicity, and aggregation is always a problem.

Table 1.2 Classification of nanostructures on the basis of dimensions

Dimensions	Nanoscale Dimension
 <p>0-D $d \leq 100$</p>	<p>All the three dimensions at nanoscale</p> <p>e.g., nanoparticles</p>
 <p>1-D $d \leq 100$</p>	<p>Two dimensions at nanoscale, L is not</p> <p>e.g., nanorods, nanotubes</p>
 <p>2-D $t \leq 100$</p>	<p>One dimension (t) at nanoscale, other two are not</p> <p>e.g., thin nanofilms</p>
 <p>3-D</p>	<p>All the three dimensions are not at nanoscale</p> <p>e.g., nanocrystalline and nanocomposite materials</p>

1.4.2 Nanostructures as transducers

Nanostructures of noble metals mainly gold and silver are intriguing to scientists because they can strongly scatter and absorb the light because of large optical field enhancements,⁵⁶ conductivity, chemical and physical stability, biocompatibility, and

capability to form self-assembled monolayers (SAMs) on the surface. All of these properties are most of what is required for an ideal transducer of a biosensor.

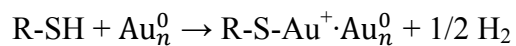
1.5 Modification of Transducer Surface

One of the very first steps for any biosensor is to modify the transducer surface with a suitable bioreceptor. This can be achieved by either chemically or physically immobilizing or trapping the bioreceptor on the surface of the transducer.

1.5.1 Self-assembled monolayers (SAMs)

For chemically immobilizing biomolecules on the surface of the noble metals, we can either modify the surface with organic monolayer films first or directly immobilize on the surface by modifying the biomolecules themselves. This can be achieved using either the Langmuir–Blodgett technique, where preassembled films at the air–water interface are transferred to the nanostructured surface, or a self-assembly technique, where molecules assemble themselves on the metal surface.⁵⁷ Between these two techniques, self-assembly is popular as it is easy to perform and results in stronger chemisorption of an organic monolayer on a nanostructure surface in contrast to physisorption by the Langmuir–Blodgett technique. Organic molecules with head-groups like thiols, disulfides, and amines, and tail group having hydrophobic alkanes can easily self-assemble on the surface of noble metal nanostructures reducing the surface free energy of metals to form monolayer films, called self-assembled monolayers (SAMs).⁵⁸ A schematic diagram of a SAM having terminal functional groups is shown in **Figure 1.8**. Different types of functional group can be attached to the terminal end of the hydrophobic part depending on the nature of the study, through which further chemistry

can be performed. Thiol head-group-based SAMs are the most studied SAMs to date because of strong thiol-gold bond formation.⁵⁹



The most common method of preparing SAM is by immersing a metal substrate into dilute (1–10 mM) ethanolic solution of thiols for overnight (12–17 h) in ambient conditions.⁵⁹ When thiol atoms come in contact with a clean metal surface, they start forming monolayers instantly; however, the molecules reorganize themselves if the metal surface is left in solution over a longer period, minimizing the defects.⁶⁰ Alkyl chains of SAMs arrange themselves in trans-conformation with nearly 20–30° tilt from normal to the metal surface.⁶¹ However, studies have shown that overall arrangement and binding of SAMs on the gold surface depend on a numbers of factors, including length of alkyl chains, the nature and distance between terminal functional group, concentration and purity of adsorbate, immersion time, and substrate morphology.⁵⁹

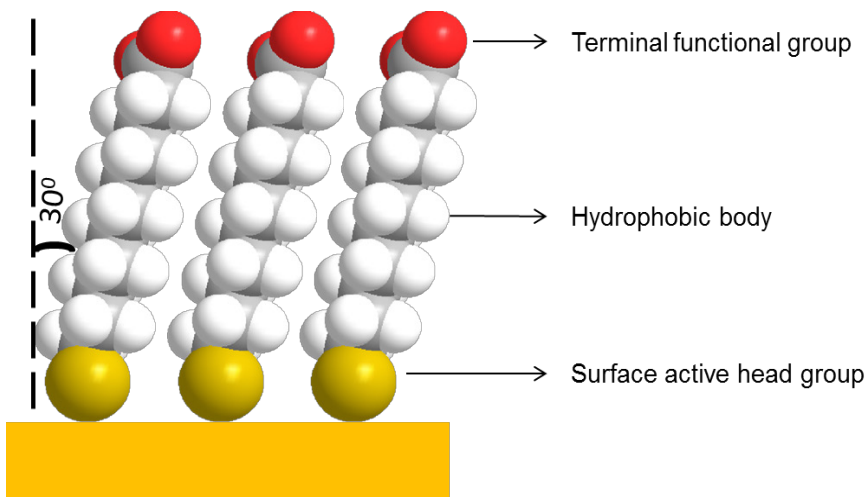


Figure 1.8 Schematic depiction of an ideal SAM formed on a gold substrate.

It has been found that SAMs formed by molecules with longer alkyl chains form less defect compared to SAMs formed by shorter alkyl chain (fewer than 8 carbons).⁶² Mixed SAMs of two different adsorbates can be prepared to control the density of the required molecule and is also useful if the required molecule's own physical dimensions would prevent forming a well-organized assembly.⁶³⁻⁶⁴ SAMs formed on the substrate can also be removed from the substrate bringing the substrate back to original condition. Different mechanical and chemical treatment can be performed to remove the SAMs from substrate, including thermal desorption, ion sputtering, plasma oxidation, photo-oxidation, electrochemical reduction, use of chemical oxidants or reductants such as strong acids and bases.^{59, 65} Scanning probe microscopy (SPM) techniques, such as scanning tunneling microscopy (STM) and atomic force microscopy (AFM), are the commonly used techniques for determining the arrangement of SAMs and defects on the substrate. Thickness of the SAMs can be determined using ellipsometry and AFM techniques and the composition and functionality can be determined using IR spectroscopy, SERS, XPS, and XRD. Other techniques used for characterizing SAMs include electrochemical techniques (CV, EIS, and SWV) and surface plasmon resonance spectroscopy.⁵⁹ SAMs have application in diverse disciplines, including biosensors, nanotechnology, biomolecular electronics, biomimetics, and as corrosion inhibitions.

1.5.2 Protein immobilization

Proteins are biological macromolecules which have an imperative role in living organisms, including regulating metabolic process, transporting and storing essential molecules, generating energy, and defending from foreign substances.⁶⁶⁻⁶⁷ Analyzing proteins in vitro and studying their interactions with other biomolecules will not only

help to understand the mechanism of interactions, but also help in many other important fields, including diagnosis, drug discovery, proteomics, quality control, and environmental monitoring.⁶⁸ One of the methods for using proteins for in vitro analysis is by immobilizing them on appropriate substrate surfaces such as clean glass, silicon plates, and metal surfaces. There are wide varieties of methods for immobilizing proteins on the substrate, but selection of the most appropriate method depends on types of substrate, properties of proteins and nature of the study.⁶⁹ When immobilizing proteins, certain things should be taken into consideration such as the possibility of denaturation, change of conformation with loss in activity, low density on the surface, nonspecific protein adsorption, and aggregation.⁷⁰ In general, protein immobilization can be categorized into physical, covalent, and bioaffinity immobilization.⁷¹

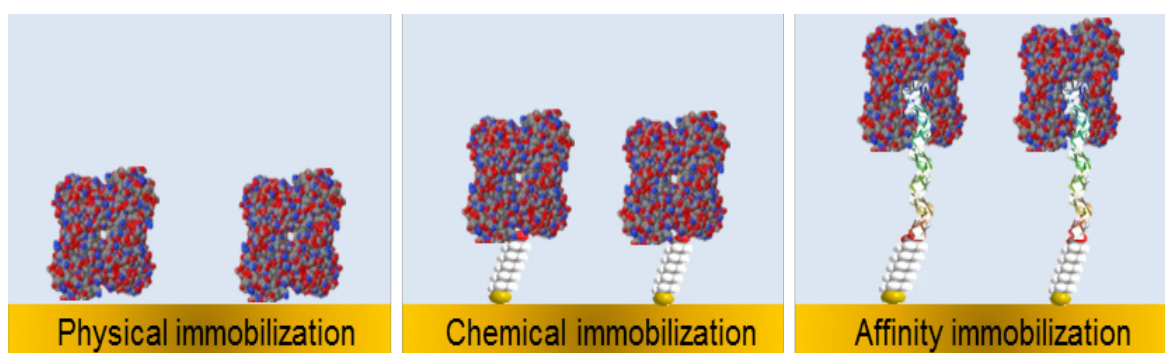


Figure 1.9 Schematic diagram of protein immobilization techniques.

1.5.2.1 Physical immobilization

Depending on the nature of protein and substrate, protein can adsorb physically on the substrate surface via interaction by one or more intermolecular forces such as hydrophobic, electrostatic (ionic), van der Waals, or hydrogen-bonding interactions (**Figure 1.9**).⁷² This method is simple and no other activity decreasing chemicals are

needed. However, proteins immobilized by this method are weakly attached to the surface, heterogeneous, and can orient themselves randomly. Furthermore, it is difficult to control the density of protein on the surface and reproducibility is always a problem.

1.5.2.2 Covalent immobilization

To overcome the disadvantages of physical immobilization techniques, covalent immobilization can be applied. Proteins immobilized by this method are more stable under buffer condition. The first step of covalent immobilization is to form self-assembled monolayers with appropriate terminal functional groups.⁷³ The choice of functional group depends on which functional group of the protein is targeted for coupling. Commonly available functional groups on the surface of proteins are -NH_2 , -COOH , -SH , and -OH present in the amino acids Lys, Asp and Glu, Cys, and Thr and Ser, respectively.⁷¹ If the -NH_2 functional groups of the protein are targeted, the terminal group of SAMs should be carboxylic acid or aldehyde so that cross coupling between functional groups can be performed, immobilizing the protein. Similarly, for -COOH , -SH , and -OH the terminal groups of SAMs can be an amine, maleimide, and epoxide, respectively. While covalently immobilizing the protein, there is always the chance that analyte binding sites may be affected because of chemical modification of proteins.⁷⁴ Choosing the appropriate chemistry, however, helps to avoid or at least minimize the loss in protein activity.

Targeting the amine groups of the lysines present in proteins is one of the most common approaches to covalently immobilize protein.⁷⁵ In this method, a SAM of desired alkane chain length with terminal -COOH groups is immobilized on a suitable substrate. The next step, then, is to activate the carboxyl group which can be achieved by

using 1-ethyl-3-(3-dimethylaminopropyl)carbodiimide hydrochloride (EDC)/N-hydroxysuccinimide (NHS) chemistry.⁷⁶ A detailed mechanism of EDC/NHS for coupling reaction of -COOH and -NH_2 groups is shown in **Figure 1.10**. When EDC reacts with the carboxyl group, it forms an amine-reactive intermediate, an O-acylisourea. The intermediate formed by this reaction, however, is relatively unstable and susceptible to hydrolysis by regeneration of the carboxyl group and is therefore not useful in the two-step conjugation procedures without stabilization. The use of NHS allows the conversion of the O-acylisourea intermediate into a relatively stable but amine reactive NHS-ester. Finally, protein immobilization occurs through displacement of NHS groups by -NH_2 group present on lysine residues of the protein. It is worth noting that the factors that govern the stability and efficiency of NHS-ester cross-linking with the amine group on the protein include the ionic strength of a buffer, pH, concentration, and the ratio of EDC/NHS.⁷⁰

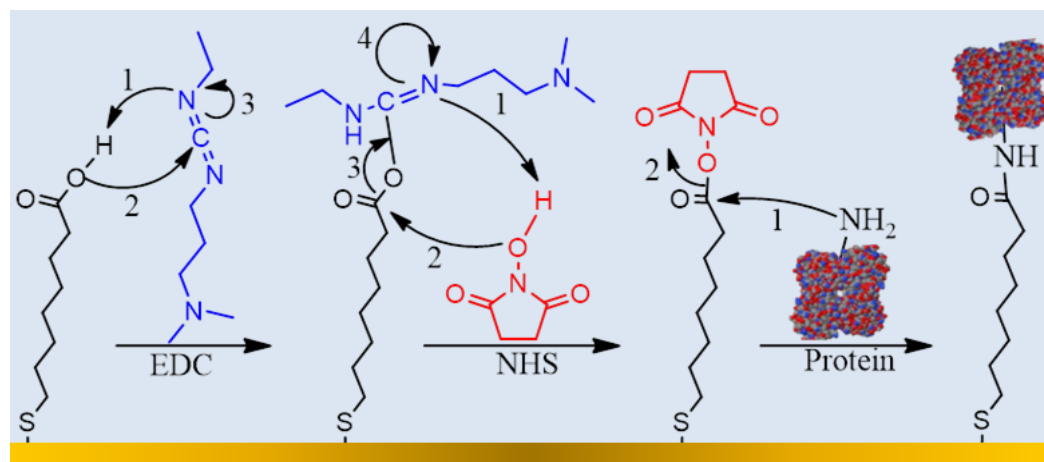


Figure 1.10 Covalent protein immobilization mechanisms via EDC/NHS coupling

Using covalent methods, proteins can be strongly bound to the surface with minimum loss of activity; however, sites and orientation of immobilized molecules

cannot be predicted appropriately.⁷¹ If the experiment needs to know these conditions, bioaffinity methods of immobilization can be used.

1.5.2.3 Bioaffinity immobilization

The first step of the bioaffinity immobilization method is to immobilize protein or molecule which works as bioreceptor through a physical or covalent immobilization process, which is then followed by specific binding of other proteins (analyte) to the bioreceptor (**Figure 1.9**). This process results in a specific orientation of protein that can be predicted from that of the binding sites of the bioreceptor molecules. The capturing of a bioreceptor specific analyte from complex mixtures, such as blood and cell extract, is also possible.⁷⁷ The binding, however, is weaker compared to covalent immobilization but stronger than physical immobilization. Another advantage of this method is that the analyte can be detached from bioreceptor by changing pH, temperature, and passing competitively strongly binding molecules, generating a fresh bioreceptor on the surface.⁷⁷ Some of the commonly used bioaffinity-based immobilization approaches includes: antibody–antigen,⁷⁸ lectin–carbohydrate,⁷⁹ and strept(avidin)–biotin interactions⁸⁰.

Antibody–antigen.

Antibody (Ab) or immunoglobulin (Ig) is a special type of protein which specifically recognizes and destroys foreign substances (antigens), such as bacteria and viruses, if found inside the body.⁸¹ The basic structure of typical antibodies comprises of two identical large heavy chains and two identical small light chains, giving a Y shaped structure for a monomer.⁸² The arm fragments of the Y shape contain the antigen binding sites and hence are given the name Fab (antibody binding fragments) whereas the base fragments of Y is called Fc (crystallizable fragment) as this part can be easily

crystallized. The Fab region further comprises of constant and variable domain for both heavy and light chains.⁸³ If the antibody can be immobilized at the Fc region, the antigen can easily be captured at the Fab region.

There are five different isotypes of immunoglobulin, IgA, IgD, IgE, IgG, and IgM, among which, IgG is most abundant and plays an important role against invading pathogens.⁸¹ Detecting the certain type of antigen or excessive production of other types of antigen using biosensors helps to predict the type of disease or abnormality present in the body. One of such examples include, detecting tumor markers from the bodily fluid for the early prediction of cancer.⁸⁴

Carbohydrate–lectin.

Lectins are another special type of protein, which have the ability to bind specific types of carbohydrate.⁸⁵ Therefore, lectins can also specifically bind to glycoproteins, bacteria and virus by targeting their carbohydrate moieties.⁸⁶ For immobilizing lectin or glycoprotein using this method, one of these proteins is first covalently immobilized on the substrate and then target protein can be specifically immobilized. Direct interaction of protein free carbohydrate with lectin can also be studied e.g., mannose to Concanavalin A (Con A)⁸⁷ and galactose to peanut agglutinin (PNA)⁸⁸.

1.6 References

1. MacNaught, A. D.; Wilkinson, A. R.; Pure, I. U. o.; Chemistry, A., *Compendium of Chemical Terminology: Iupac Recommendations*. Blackwell Science: 1997.
2. Velusamy, V.; Arshak, K.; Korostynska, O.; Oliwa, K.; Adley, C., An Overview of Foodborne Pathogen Detection: In the Perspective of Biosensors. *Biotechnol. Adv.* **2010**, 28 (2), 232-254.
3. Clark, L. C.; Lyons, C., Electrode Systems for Continuous Monitoring in Cardiovascular Surgery. *Ann. N.Y. Acad. Sci.* **1962**, 102 (1), 29-45.
4. Wang, J., Glucose Biosensors: 40 Years of Advances and Challenges. *Electroanalysis* **2001**, 13 (12), 983-988.
5. Clarke, S. F.; Foster, J. R., A History of Blood Glucose Meters and Their Role in Self-Monitoring of Diabetes Mellitus. *Br. J. Biomed. Sci.* **2012**, 69 (2), 83-93.
6. Lu, Y.; Xiang, Y., Personal Glucose Meters for Detection and Quantification of a Broad Range of Analytes. Google Patents: 2012.
7. Kovalevskaya, G.; Birken, S.; Kakuma, T.; O'Connor, J. F., Early Pregnancy Human Chorionic Gonadotropin (Hcg) Isoforms Measured by an Immunometric Assay for Choriocarcinoma-Like Hcg. *J. Endocrinol.* **1999**, 161 (1), 99-106.
8. Terry, L. A.; White, S. F.; Tigwell, L. J., The Application of Biosensors to Fresh Produce and the Wider Food Industry. *J. Agric. Food. Chem.* **2005**, 53 (5), 1309-1316.
9. Hanrahan, G.; Patil, D. G.; Wang, J., Electrochemical Sensors for Environmental Monitoring: Design, Development and Applications. *J. Environ. Monit.* **2004**, 6 (8), 657-664.
10. Healy, D. A.; Hayes, C. J.; Leonard, P.; McKenna, L.; O'Kennedy, R., Biosensor Developments: Application to Prostate-Specific Antigen Detection. *Trends Biotechnol.* **2007**, 25 (3), 125-131.
11. Klenkar, G.; Liedberg, B., A Microarray Chip for Label-Free Detection of Narcotics. *Anal. Bioanal. Chem.* **2008**, 391 (5), 1679-1688.
12. Zelada-Guillén, G. A.; Bhosale, S. V.; Riu, J.; Rius, F. X., Real-Time Potentiometric Detection of Bacteria in Complex Samples. *Anal. Chem.* **2010**, 82 (22), 9254-9260.
13. Wu, L.; Zhang, X.; Liu, W.; Xiong, E.; Chen, J., Sensitive Electrochemical Aptasensor by Coupling "Signal-on" and "Signal-Off" Strategies. *Anal. Chem.* **2013**, 85 (17), 8397-8402.
14. Monošík, R.; Stred'anský, M.; Šturdík, E., Biosensors - Classification, Characterization and New Trends. *Acta Chimica Slovaca* **2012**, 5 (1), 109-120.
15. Wilson, M. S., Electrochemical Immunosensors for the Simultaneous Detection of Two Tumor Markers. *Anal. Chem.* **2005**, 77 (5), 1496-1502.
16. Ariksoysal, D. O.; Karadeniz, H.; Erdem, A.; Sengonul, A.; Sayiner, A. A.; Ozsoz, M., Label-Free Electrochemical Hybridization Genosensor for the Detection of Hepatitis B Virus Genotype on the Development of Lamivudine Resistance. *Anal. Chem.* **2005**, 77 (15), 4908-4917.
17. Grabowska, I.; Malecka, K.; Stachyra, A.; Góra-Sochacka, A.; Sirko, A.; Zagórski-Ostojka, W.; Radecka, H.; Radecki, J., Single Electrode Genosensor for

Simultaneous Determination of Sequences Encoding Hemagglutinin and Neuraminidase of Avian Influenza Virus Type H5n1. *Anal. Chem.* **2013**, *85* (21), 10167-10173.

18. Vo-Dinh, T.; Cullum, B., Biosensors and Biochips: Advances in Biological and Medical Diagnostics. *Fresenius J. Anal. Chem.* **2000**, *366* (6-7), 540-51.

19. Setford, S. J.; White, S. F.; Bolbot, J. A., Measurement of Protein Using an Electrochemical Bi-Enzyme Sensor. *Biosens. Bioelectron.* **2002**, *17* (1), 79-86.

20. Ronkainen, N. J.; Halsall, H. B.; Heineman, W. R., Electrochemical Biosensors. *Chem. Soc. Rev.* **2010**, *39* (5), 1747-1763.

21. Liao, W.-Y.; Chou, T.-C., Fabrication of a Planar-Form Screen-Printed Solid Electrolyte Modified Ag/AgCl Reference Electrode for Application in a Potentiometric Biosensor. *Anal. Chem.* **2006**, *78* (12), 4219-4223.

22. Kissinger, P. T.; Heineman, W. R., Cyclic Voltammetry. *J. Chem. Educ.* **1983**, *60* (9), 702.

23. Lisdat, F.; Schäfer, D., The Use of Electrochemical Impedance Spectroscopy for Biosensing. *Anal. Bioanal. Chem.* **2008**, *391* (5), 1555-1567.

24. Chang, B.-Y.; Park, S.-M., Electrochemical Impedance Spectroscopy. *Annu. Rev. Anal. Chem.* **2010**, *3*, 207-229.

25. Retter, U.; Lohse, H., Electrochemical Impedance Spectroscopy. In *Electroanalytical Methods*, Springer: 2002; pp 149-166.

26. Singh, R.; Suni, I. I., Minimizing Nonspecific Adsorption in Protein Biosensors That Utilize Electrochemical Impedance Spectroscopy. *J. Electrochem. Soc.* **2010**, *157* (10), J334-J337.

27. Fan, X.; White, I. M.; Shopova, S. I.; Zhu, H.; Suter, J. D.; Sun, Y., Sensitive Optical Biosensors for Unlabeled Targets: A Review. *Anal. Chim. Acta* **2008**, *620* (1), 8-26.

28. Viveros, L.; Paliwal, S.; McCrae, D.; Wild, J.; Simonian, A., A Fluorescence-Based Biosensor for the Detection of Organophosphate Pesticides and Chemical Warfare Agents. *Sens. Actuators B Chem.* **2006**, *115* (1), 150-157.

29. Homola, J.; Yee, S. S.; Gauglitz, G., Surface Plasmon Resonance Sensors: Review. *Sens. Actuators B Chem.* **1999**, *54* (1), 3-15.

30. Willets, K. A.; Van Duyne, R. P., Localized Surface Plasmon Resonance Spectroscopy and Sensing. *Annu. Rev. Phys. Chem.* **2007**, *58*, 267-297.

31. Homola, J., Present and Future of Surface Plasmon Resonance Biosensors. *Anal. Bioanal. Chem.* **2003**, *377* (3), 528-539.

32. Homola, J., Surface Plasmon Resonance Sensors for Detection of Chemical and Biological Species. *Chem. Rev.* **2008**, *108* (2), 462-493.

33. Yao, Y.; Yi, B.; Xiao, J.; Li, Z. In *Surface Plasmon Resonance Biosensors and Its Application*, Bioinformatics and Biomedical Engineering, 2007. ICBBE 2007. The 1st International Conference on, IEEE: 2007; pp 1043-1046.

34. Ringe, E.; McMahon, J. M.; Sohn, K.; Cobley, C.; Xia, Y.; Huang, J.; Schatz, G. C.; Marks, L. D.; Van Duyne, R. P., Unraveling the Effects of Size, Composition, and Substrate on the Localized Surface Plasmon Resonance Frequencies of Gold and Silver Nanocubes: A Systematic Single-Particle Approach. *J. Phys. Chem. C* **2010**, *114* (29), 12511-12516.

35. Mayer, K. M.; Hafner, J. H., Localized Surface Plasmon Resonance Sensors. *Chem. Rev.* **2011**, *111* (6), 3828-3857.

36. Hu, M.; Novo, C.; Funston, A.; Wang, H.; Staleva, H.; Zou, S.; Mulvaney, P.; Xia, Y.; Hartland, G. V., Dark-Field Microscopy Studies of Single Metal Nanoparticles: Understanding the Factors That Influence the Linewidth of the Localized Surface Plasmon Resonance. *J. Mater. Chem.* **2008**, *18* (17), 1949-1960.
37. Ramanathan, K.; Danielsson, B., Principles and Applications of Thermal Biosensors. *Biosens. Bioelectron.* **2001**, *16* (6), 417-423.
38. Zhang, Y.; Tadigadapa, S., Calorimetric Biosensors with Integrated Microfluidic Channels. *Biosens. Bioelectron.* **2004**, *19* (12), 1733-1743.
39. Shen, Z.; Huang, M.; Xiao, C.; Zhang, Y.; Zeng, X.; Wang, P. G., Nonlabeled Quartz Crystal Microbalance Biosensor for Bacterial Detection Using Carbohydrate and Lectin Recognitions. *Anal. Chem.* **2007**, *79* (6), 2312-2319.
40. Mannelli, I.; Minunni, M.; Tombelli, S.; Mascini, M., Quartz Crystal Microbalance (Qcm) Affinity Biosensor for Genetically Modified Organisms (Gmos) Detection. *Biosens. Bioelectron.* **2003**, *18* (2), 129-140.
41. Whitesides, G. M.; Mathias, J. P.; Seto, C. T., Molecular Self-Assembly and Nanochemistry: A Chemical Strategy for the Synthesis of Nanostructures. *Science (Washington, D. C., 1883-)* **1991**, *254* (5036), 1312-19.
42. Parveen, S.; Misra, R.; Sahoo, S. K., Nanoparticles: A Boon to Drug Delivery, Therapeutics, Diagnostics and Imaging. *Nanomed-Nanotechnol* **2012**, *8* (2), 147-166.
43. Ghosh Chaudhuri, R.; Paria, S., Core/Shell Nanoparticles: Classes, Properties, Synthesis Mechanisms, Characterization, and Applications. *Chem. Rev.* **2011**, *112* (4), 2373-2433.
44. Schwartzberg, A. M.; Zhang, J. Z., Novel Optical Properties and Emerging Applications of Metal Nanostructures†. *J. Phys. Chem. C* **2008**, *112* (28), 10323-10337.
45. Jain, P. K.; Huang, X.; El-Sayed, I. H.; El-Sayed, M. A., Noble Metals on the Nanoscale: Optical and Photothermal Properties and Some Applications in Imaging, Sensing, Biology, and Medicine. *Acc. Chem. Res.* **2008**, *41* (12), 1578-1586.
46. Xia, Y.; Yang, P.; Sun, Y.; Wu, Y.; Mayers, B.; Gates, B.; Yin, Y.; Kim, F.; Yan, H., One-Dimensional Nanostructures: Synthesis, Characterization, and Applications. *Adv. Mater.* **2003**, *15* (5), 353-389.
47. Wiley, B.; Sun, Y.; Xia, Y., Synthesis of Silver Nanostructures with Controlled Shapes and Properties. *Acc. Chem. Res.* **2007**, *40* (10), 1067-1076.
48. Hu, J.; Odom, T. W.; Lieber, C. M., Chemistry and Physics in One Dimension: Synthesis and Properties of Nanowires and Nanotubes. *Acc. Chem. Res.* **1999**, *32* (5), 435-445.
49. Aliofkhazraei, M.; Rouhaghdam, A. S., *Fabrication of Nanostructures by Plasma Electrolysis*. John Wiley & Sons: 2010.
50. Che, G.; Lakshmi, B.; Martin, C.; Fisher, E.; Ruoff, R. S., Chemical Vapor Deposition Based Synthesis of Carbon Nanotubes and Nanofibers Using a Template Method. *Chem. Mater.* **1998**, *10* (1), 260-267.
51. Marine, W.; Patrone, L.; Luk'Yanchuk, B.; Sentis, M., Strategy of Nanocluster and Nanostructure Synthesis by Conventional Pulsed Laser Ablation. *Appl. Surf. Sci.* **2000**, *154*, 345-352.
52. Koch, C., Synthesis of Nanostructured Materials by Mechanical Milling: Problems and Opportunities. *Nanostruct. Mater.* **1997**, *9* (1), 13-22.

53. Jones, M. R.; Osberg, K. D.; Macfarlane, R. J.; Langille, M. R.; Mirkin, C. A., Templated Techniques for the Synthesis and Assembly of Plasmonic Nanostructures. *Chem. Rev.* **2011**, *111* (6), 3736-3827.
54. Haynes, C. L.; Van Duyne, R. P., Nanosphere Lithography: A Versatile Nanofabrication Tool for Studies of Size-Dependent Nanoparticle Optics. *J. Phys. Chem. B* **2001**, *105* (24), 5599-5611.
55. Tseng, A. A.; Chen, K.; Chen, C. D.; Ma, K. J., Electron Beam Lithography in Nanoscale Fabrication: Recent Development. *Electronics Packaging Manufacturing, IEEE Transactions on* **2003**, *26* (2), 141-149.
56. Jain, P. K.; Huang, X.; El-Sayed, I. H.; El-Sayed, M. A., Noble Metals on the Nanoscale: Optical and Photothermal Properties and Some Applications in Imaging, Sensing, Biology, and Medicine. *Acc. Chem. Res.* **2008**, *41* (12), 1578-86.
57. Ferretti, S.; Paynter, S.; Russell, D. A.; Sapsford, K. E.; Richardson, D. J., Self-Assembled Monolayers: A Versatile Tool for the Formulation of Bio-Surfaces. *TrAC, Trends Anal. Chem.* **2000**, *19* (9), 530-540.
58. Ulman, A., Formation and Structure of Self-Assembled Monolayers. *Chem. Rev.* **1996**, *96* (4), 1533-1554.
59. Love, J. C.; Estroff, L. A.; Kriebel, J. K.; Nuzzo, R. G.; Whitesides, G. M., Self-Assembled Monolayers of Thiolates on Metals as a Form of Nanotechnology. *Chem. Rev.* **2005**, *105* (4), 1103-1170.
60. Evans, S. D.; Sharma, R.; Ulman, A., Contact Angle Stability: Reorganization of Monolayer Surfaces? *Langmuir* **1991**, *7* (1), 156-161.
61. Laibinis, P. E.; Whitesides, G. M.; Allara, D. L.; Tao, Y. T.; Parikh, A. N.; Nuzzo, R. G., Comparison of the Structures and Wetting Properties of Self-Assembled Monolayers of N-Alkanethiols on the Coinage Metal Surfaces, Copper, Silver, and Gold. *J. Am. Chem. Soc.* **1991**, *113* (19), 7152-7167.
62. Porter, M. D.; Bright, T. B.; Allara, D. L.; Chidsey, C. E., Spontaneously Organized Molecular Assemblies. 4. Structural Characterization of N-Alkyl Thiol Monolayers on Gold by Optical Ellipsometry, Infrared Spectroscopy, and Electrochemistry. *J. Am. Chem. Soc.* **1987**, *109* (12), 3559-3568.
63. Arima, Y.; Iwata, H., Effect of Wettability and Surface Functional Groups on Protein Adsorption and Cell Adhesion Using Well-Defined Mixed Self-Assembled Monolayers. *Biomaterials* **2007**, *28* (20), 3074-3082.
64. Patel, N.; Davies, M. C.; Hartshorne, M.; Heaton, R. J.; Roberts, C. J.; Tendler, S. J. B.; Williams, P. M., Immobilization of Protein Molecules onto Homogeneous and Mixed Carboxylate-Terminated Self-Assembled Monolayers. *Langmuir* **1997**, *13* (24), 6485-6490.
65. Kakiuchi, T.; Usui, H.; Hobara, D.; Yamamoto, M., Voltammetric Properties of the Reductive Desorption of Alkanethiol Self-Assembled Monolayers from a Metal Surface. *Langmuir* **2002**, *18* (13), 5231-5238.
66. Ingebritsen, T. S.; Cohen, P., Protein Phosphatases: Properties and Role in Cellular Regulation. *Science* **1983**, *221* (4608), 331-338.
67. Abbas, A. K.; Lichtman, A. H.; Pillai, S., *Cellular and Molecular Immunology*. Elsevier Health Sciences: 1994.
68. Petricoin, E. F.; Hackett, J. L.; Lesko, L. J.; Puri, R. K.; Gutman, S. I.; Chumakov, K.; Woodcock, J.; Feigal, D. W.; Zoon, K. C.; Sistare, F. D., Medical

Applications of Microarray Technologies: A Regulatory Science Perspective. *Nat. Genet.* **2002**, 32, 474-479.

69. Lee, Y.; Lee, E. K.; Cho, Y. W.; Matsui, T.; Kang, I. C.; Kim, T. S.; Han, M. H., Proteochip: A Highly Sensitive Protein Microarray Prepared by a Novel Method of Protein Immobilization for Application of Protein-Protein Interaction Studies. *Proteomics* **2003**, 3 (12), 2289-2304.
70. Tan, Y. H.; Pandey, B.; Sharma, A.; Bhattarai, J.; Stine, K. J., Bioconjugation Reactions for Covalent Coupling of Proteins to Gold Surfaces. *Global J. Biochem.* **2012**, 3, 6.
71. Rusmini, F.; Zhong, Z.; Feijen, J., Protein Immobilization Strategies for Protein Biochips. *Biomacromolecules* **2007**, 8 (6), 1775-1789.
72. Kim, D.; Herr, A. E., Protein Immobilization Techniques for Microfluidic Assays. *Biomicrofluidics* **2013**, 7 (4), 041501.
73. Frasconi, M.; Mazzei, F.; Ferri, T., Protein Immobilization at Gold-Thiol Surfaces and Potential for Biosensing. *Anal. Bioanal. Chem.* **2010**, 398 (4), 1545-1564.
74. Mateo, C.; Fernández-Lorente, G.; Abian, O.; Fernández-Lafuente, R.; Guisán, J. M., Multifunctional Epoxy Supports: A New Tool to Improve the Covalent Immobilization of Proteins. The Promotion of Physical Adsorptions of Proteins on the Supports before Their Covalent Linkage. *Biomacromolecules* **2000**, 1 (4), 739-745.
75. Stine, K. J.; Jefferson, K.; Shulga, O. V., Nanoporous Gold for Enzyme Immobilization. In *Enzyme Stabilization and Immobilization*, Springer: 2011; pp 67-83.
76. Wissink, M.; Beernink, R.; Pieper, J.; Poot, A.; Engbers, G.; Beugeling, T.; Van Aken, W.; Feijen, J., Immobilization of Heparin to Edc/Nhs-Crosslinked Collagen. Characterization and in Vitro Evaluation. *Biomaterials* **2001**, 22 (2), 151-163.
77. Saleemuddin, M., Bioaffinity Based Immobilization of Enzymes. In *Thermal Biosensors, Bioactivity, Bioaffinity*, Springer: 1999; pp 203-226.
78. Karlsson, R.; Michaelsson, A.; Mattsson, L., Kinetic Analysis of Monoclonal Antibody-Antigen Interactions with a New Biosensor Based Analytical System. *J. Immunol. Methods* **1991**, 145 (1), 229-240.
79. Lee, R. T.; Lee, Y. C., Affinity Enhancement by Multivalent Lectin-Carbohydrate Interaction. *Glycoconjugate J.* **2000**, 17 (7-9), 543-551.
80. Wilchek, M.; Bayer, E. A.; Livnah, O., Essentials of Biorecognition: The (Strept) Avidin-Biotin System as a Model for Protein-Protein and Protein-Ligand Interaction. *Immunol. Lett.* **2006**, 103 (1), 27-32.
81. Janeway, C., *Immunobiology Five*. Garland Pub.: 2001.
82. Leatherbarrow, R. J.; Stedman, M.; Wells, T. N., Structure of Immunoglobulin G by Scanning Tunnelling Microscopy. *J. Mol. Biol.* **1991**, 221 (2), 361-365.
83. Al-Lazikani, B.; Lesk, A. M.; Chothia, C., Standard Conformations for the Canonical Structures of Immunoglobulins. *J. Mol. Biol.* **1997**, 273 (4), 927-948.
84. Tothill, I. E. In *Biosensors for Cancer Markers Diagnosis*, Semin. Cell Dev. Biol., Elsevier: 2009; pp 55-62.
85. Sharon, N.; Lis, H., Lectins as Cell Recognition Molecules. *Science* **1989**, 246 (4927), 227-234.
86. Lis, H.; Sharon, N., Lectins: Carbohydrate-Specific Proteins That Mediate Cellular Recognition. *Chem. Rev.* **1998**, 98 (2), 637-674.

87. Naismith, J. H.; Field, R. A., Structural Basis of Trimannoside Recognition by Concanavalin A. *J. Biol. Chem.* **1996**, 271 (2), 972-976.
88. Ambrosi, M.; Cameron, N. R.; Davis, B. G.; Stolnik, S., Investigation of the Interaction between Peanut Agglutinin and Synthetic Glycopolymeric Multivalent Ligands. *Org. Biomol. Chem.* **2005**, 3 (8), 1476-1480.

CHAPTER 2 MATERIALS AND METHODS

2.1 Materials

Gold wire of 0.2 mm diameter (99.99%) was obtained from Electron Microscopy Sciences (Fort Washington, PA). Silicon wafer (3" N<100>, 1–10 ohm–cm, 356–406 μm thick) prime grade was purchased from Nova Electronic Materials, LLC (Flower Mound, TX). Fisherbrand plain microscope slides 25 mm \times 75 mm \times 1 mm were purchased from Fisher Scientific (Fairlawn, NJ). Sulfuric acid and 30% hydrogen peroxide required to prepare piranha were also purchased from Fisher Scientific. Methanol (HPLC grade), ethanol (HPLC grade), glycerol, potassium dicyanoaurate(I) ($\text{K}[\text{Au}(\text{CN})_2]$) (99.98%), Potassium dicyanoargentate(I) ($\text{K}[\text{Ag}(\text{CN})_2]$) (99.96%), 11-mercaptoundecanoic acid (MUA), and N-hydroxysuccinimide (NHS) were purchased from Sigma–Aldrich, Inc. (Milwaukee, WI). Epoxy (EPO–TEK 377) was purchased from Epoxy Technology (Billerica, MA). Sodium carbonate anhydrous, sodium acetate, calcium chloride dihydrate, manganese(II) chloride tetrahydrate, potassium nitrate and methyl α -D-mannopyranoside (>99%) were obtained from Sigma–Aldrich, Inc. (Allentown, PA). Bovine serum albumin (BSA), concanavalin A (Con A), transferrin, immunoglobulin G (IgG) from rabbit serum, fetuin and asialofetuin (type I) from fetal calf serum, soybean agglutinin, tris(hydroxymethyl) aminomethane (Tris) buffer, Phosphate buffer saline (pH 7.4) and *N*-(3-dimethylaminopropyl)-*N'*-ethylcarbodiimide hydrochloride were purchased from Sigma–Aldrich, Inc. (Saint Louis, MO). Carcinoembryonic antigen (CEA) and prostate specific antigen (PSA) were purchased from Fitzgerald (North Acton, MA). Alkaline phosphatase labeling kits were purchased from Dojindo Molecular Technologies

Inc. (Rockville, Maryland). p-Aminophenyl phosphate (p-APP) was obtained from Gold Biochem (St. Louis, MO). Thiolated mannoside (8-mercaptooctyl- α -D-mannopyranoside (α Man-C₈-SH)) and thiolated triethylene glycol (2-(2-(2-mercaptoethoxy)ethoxy)ethanol (TEG-SH)) were synthesized in Prof. Demchenko's lab as reported previously.¹ Milli-Q water (18.2 M Ω cm) and ethanol (HPLC grade) were used to prepare aqueous solution and self-assembled monolayers forming solutions, respectively.

2.2 Preparation of Nanoporous Gold (NPG)

NPG was prepared as a coating on gold wire or as a thin film on a flat gold surface depending on the experiment conducted.

2.2.1 Preparation of NPG on gold wire

NPG-coated gold wire was prepared by first electrochemically depositing gold and silver on 5 mm long and 0.2 mm diameter gold wires to form an alloy.² Three-electrode cell consisting of platinum (Pt) as an auxiliary electrode, silver/silver chloride (Ag/AgCl) as a reference electrode and gold wire as working electrode was used. The electrolytes mixture consists of 250 mM sodium carbonate and 30:70% 50 mM K[Au(CN)₂] and 50 mM K[Ag(CN)₂], respectively. The electrolyte solution was deaerated by bubbling argon gas for 10 min and the deposition was performed at ambient pressure and temperature. The time and potential of deposition were varied depending on experiment. As-prepared alloy was dealloyed by immersing the alloy-coated gold wire in concentrated nitric acid for 24 h, during which less noble silver metal was selectively removed, giving porous structures, which was then rinsed with Milli-Q water and stored in ethanol until further use.

2.2.2 Preparation of NPG on flat gold plate

2.2.2.1 Preparing glass slides

Glass slides were cut to size of 12.5 mm × 10 mm × 1 mm. Cut glass slides were cleaned using piranha solution (3:1, H₂SO₄:30% H₂O₂) for 45 min, (**Warning:** Because of its oxidizing nature, piranha reacts violently with organic compounds, so care must be taken while handling) rinsed with copious amount of Milli-Q water and stored in methanol. The slides were dried in an oven at 125 °C for 30 min and cooled prior to use.

2.2.2.2 Flat gold preparation

Flat gold was prepared using a published method with some modifications.³ In brief, a Hummer VI sputter coater (Anatech Ltd.) was used to sputter gold onto the silicon wafer for 20 min, adjusting the current to 10 mA to get a thickness of about 200 nm. Then, one drop of thoroughly mixed two components of epoxy (EPO-TEK 377) was used for attaching a clean glass slide to the gold sputtered silicon wafer. Multilayers of silicon wafer-gold-epoxy-glass slides were cured at 150 °C for 2 h. After cooling, glass slides were stripped off of the silicon wafer using a slight force with the help of tweezers to expose a flat gold surface.

2.2.2.3 NPG on flat gold surface

An alloy of Au and Ag was formed on a flat gold surface similarly as on the NPG-coated gold wire. However, dealloying was performed electrochemically in KNO₃ solution by applying different potentials for different times.

2.3 Electrochemical Annealing of Nanoporous Gold Wire

The NPG formed on gold wire was further electrochemically annealed to increase the pore size or interligament gap while still keeping the surface area high. Three different solutions, 0.1 M KCl, 0.1 M NaNO₃, and 0.1 M NaClO₄ were chosen and their effects on annealing were studied. Cyclic potential sweeps of 30 or 50 oxidation–reduction cycles at 100 mV s^{−1} from −0.4 V to +1.2 V with a 2 s hold at the positive end and an 8 s hold at the negative end of each cycle was used. Total cycles were performed in five-cycle increments while determining the surface area after every fifth cycle. Finally, the annealed wires were cleaned and dried under nitrogen.

2.4 Preparation of Nanostructured Gold and Silver Films

Thin films of nanostructured gold (NGF) were prepared on a flat gold surface (working electrode) from 50 mM aqueous solution of potassium dicyanoaurate(I) containing 0.25 M sodium carbonate electrolyte by applying different potentials for different period of times at room temperature.⁴ Similarly, nanostructured silver films (NSF) were prepared from 50 mM aqueous solution of potassium dicyanoargentate(I) containing 0.25 M sodium carbonate electrolyte on a flat gold surface.

2.5 Surface Modification with Organic and Biological Molecules

The nanostructured surfaces have been modified using different organic and biological molecules. Different thiolated organic molecules having terminal functional group were used to link the biomolecules to the nanostructured surface.

2.5.1 Preparation of self-assembled monolayers (SAMs)

SAMs on a nanostructured surface were formed by directly immersing in 1 mM ethanolic solution of two thiolated molecules. One of the two thiolated compounds had a desired terminal functional group for further immobilization, whereas other was compatible thiolated polyethylene glycol. Depending on the type of experiment, nanostructured surface were left in thiolated solutions for either 2 h or overnight (17 h). The resulting SAMs surface was rinsed with ethanol and dried under nitrogen flow.

2.5.2 Covalent immobilization of proteins on SAMs

For covalently immobilizing the proteins on SAMs functionalized nanostructured surfaces, we have used either lipoic acid (LPA) or alkanethiols with different carbon chain length having –COOH terminal groups. Once the SAMs were formed, the terminal –COOH groups were activated by immersing the nanostructured substrate in 5 mM EDC/NHS (1:1) solution (detailed mechanism is reported in section 1.6.2.2.). The activated surfaces were allowed to react with different concentration of the desired protein solutions for different periods depending on the nature of the study. The immobilized proteins were washed with buffer before recording the data or used for further steps.

2.5.3 Bioaffinity immobilization of proteins

For this type of immobilization, the SAMs formed should have a terminal molecule that specifically binds to the desired proteins. We have studied the specific interaction between mannose and Concanavalin A protein on both NPG and NGF surfaces using different techniques.

2.5.3.1 Mannose–Con A binding assay on NGF using LSPR spectroscopy

Mixed self-assembled monolayers (SAMs) of α Man-C8-SH and TEG-SH were prepared on the surface of NGF by coadsorption from ethanol having total concentration 1 mM (molar ratio 1:3) for 2 h at room temperature. After coadsorption, NGF plate was washed with ethanol, dried under nitrogen, and placed inside the flow cell. Tris buffer (10 mM, pH 7.4) containing NaCl (0.1 M), CaCl_2 (1 mM) and MnCl_2 (1 mM) was passed through the flow cell followed by Con A and allowed to interact for 1 h, washed with the buffer followed by water and dried under nitrogen flow before collecting LSPR spectra. However, for the real-time interactions study all the spectra were collected in buffer.

2.6 Localized Surface Plasmon Resonance Spectroscopy

The LSPR spectra of NGF were acquired using reflection geometry. It consists of a white light source (HL-2000 Tungsten Halogen Light, Ocean Optics), spectrometer (Jaz, Ocean Optics) connected to a computer having SpectraSuite software (Ocean Optics), a reflection probe (Ocean Optics) and a home-built flow cell. The reflection probe consists of a bundle of seven optical fibers with six illumination fibers around one read fiber. The nanostructured film modified glass slide was kept tightly inside the home-built flow cell which can hold a volume of 0.5 mL and has a quartz window for the light to pass through. The distance between probe and sample was kept constant at approximately 4 mm. The reflection spectra obtained were inverted using SigmaPlot 12.0 (Systat Software Inc.) and analyzed using OriginPro 8.5.0 SR1 (OriginLab Corporation).

2.7 Electrochemical Characterization

All the electrochemical experiments were carried out using either a potentiostat/galvanostat model 273A or PARSTAT 2273 (EG & G Princeton Applied Research) operated by PowerSuite software and a three-electrode cell having Ag/AgCl (KCl sat.) (0.22 V vs. SHE) as a reference electrode (CH Instruments Inc., Austin, TX) and platinum wire (99.997% purity, 0.5 mm diameter) as a counter-electrode (Alfa Aesar, Ward Hill, MA).

2.7.1 Cyclic voltammetry (CV)

CV was used to determine the surface area of nanostructured gold by the gold oxide stripping method and to determine the electrochemically accessible surface area. The gold oxide stripping experiment was performed using 7 mL of 0.5 M sulfuric acid (H_2SO_4) as an electrolyte at a scan rate 100 mV s^{-1} and scanning the potential from 0 to 1.6 V and back to 0 V (vs. Ag/AgCl). The charge under the reduction peak of cyclic voltammogram was integrated to obtain the surface area, using the reported conversion factor $450 \text{ } \mu\text{C}/\text{cm}^2$.⁵

Electrochemical accessible surface area of nanostructured gold was determined by taking a CV in 10 mM potassium ferricyanide ($\text{K}_3[\text{Fe}(\text{CN})_6]$). When anodic or cathodic peak current of the cyclic voltammogram was plotted versus the square root of scan rate, a straight line was obtained. The slope of the line was used in the Randles–Sevcik equation to obtain the electrochemically accessible surface area, eq 3. CV was also performed for checking the surface purity of regenerated NGF using 1 mM $\text{K}_3[\text{Fe}(\text{CN})_6]$ in 0.1 M KCl by applying a potential scan from -0.2 to 0.6 V versus Ag/AgCl (KCl sat.).

2.7.2 Electrochemical impedance spectroscopy (EIS)

EIS was performed in 5 mM $\text{K}_3[\text{Fe}(\text{CN})_6]/\text{K}_4[\text{Fe}(\text{CN})_6]$ (1:1) redox probe prepared in 10 mM phosphate buffer pH 7.4, frequency range 100 kHz to 0.1 Hz and bias potential of 0.2 V. Zsimpwin 3.21 software (Princeton Applied Research, Oak Ridge, TN) was used for data analysis.

2.7.3 Square wave voltammetry (SWV)

SWV measurements were carried out using a PARSTAT 2273 (Princeton Applied Research, Oak Ridge, TN) and the PowerPULSE software. The optimal parameters for the SWV were obtained by varying pulse width, pulse height, and step height used in the square wave voltammetric analysis of a p-aminophenol (p-AP) standard solution (1 mM). The best parameters determined for the square wave voltammetric measurement of the oxidation of p-aminophenol were; pulse height 50 mV, pulse width 0.2 s, and step height 2 mV. The potential was scanned from 0.1 to 0.2 V at a rate of 5.0 mV s^{-1} in glycine buffer (pH 9.0, 100 mM).⁶ SWV scans record the forward current (I_f), reverse current (I_r), and the difference current (ΔI) versus the applied potential. Error bars in the graphs represent standard error of three measurements.

2.8 Scanning Electron Microscopy (SEM)

SEM imaging and energy-dispersive X-ray spectroscopy (EDX) were performed using field emission scanning electron microscope (6320F, JEOL USA, Inc.). Imaging was carried out at working distance of 8 mm at an accelerating voltage of 5 kV or 8 kV. SEM images were analyzed using image processing software AnalySIS (Soft Imaging

System GmbH (version 3) to measure interligament gap and ligament width of NPG as well as any other nanostructured features.

2.9 Electrocatalytic oxidation of glucose on NPG wire

Electro-oxidation of α -D-(+)-glucose (Sigma-Aldrich), 5 mM in 0.1 M NaOH, was performed using cyclic voltammetry at a scan rate of 100 mV s^{-1} between the potential limits of -1.0 V and 0.8 V vs. Ag/AgCl reference electrode. Additional scans were performed between the limits of -1.0 V and $+0.2 \text{ V}$. Gold wire, NPG-coated gold wire, and NPG-coated Au wire annealed by cycling in 0.1 M NaNO_3 were used as working electrodes. The solutions were degassed using nitrogen for 20 min before the electrochemical measurements.

2.10 References

1. Pandey, B.; Tan, Y. H.; Fujikawa, K.; Demchenko, A. V.; Stine, K. J., Comparative Study of the Binding of Concanavalin a to Self-Assembled Monolayers Containing a Thiolated A-Mannoside on Flat Gold and on Nanoporous Gold. *J. Carbohydr. Chem.* **2012**, *31* (4-6), 466-503.
2. Shulga, O. V.; Zhou, D.; Demchenko, A. V.; Stine, K. J., Detection of Free Prostate Specific Antigen (Fpsa) on a Nanoporous Gold Platform. *Analyst* **2008**, *133* (3), 319-322.
3. Stamou, D.; Gourdon, D.; Liley, M.; Burnham, N. A.; Kulik, A.; Vogel, H.; Duschl, C., Uniformly Flat Gold Surfaces: Imaging the Domain Structure of Organic Monolayers Using Scanning Force Microscopy. *Langmuir* **1997**, *13* (9), 2425-2428.
4. Bhattarai, J. K.; Sharma, A.; Fujikawa, K.; Demchenko, A. V.; Stine, K. J., Electrochemical Synthesis of Nanostructured Gold Film for the Study of Carbohydrate–Lectin Interactions Using Localized Surface Plasmon Resonance Spectroscopy. *Carbohydr. Res.* **2014**.
5. Pandey, B.; Tan, Y. H.; Parameswar, A. R.; Pornsuriyasak, P.; Demchenko, A. V.; Stine, K. J., Electrochemical Characterization of Globotriose-Containing Self-Assembled Monolayers on Nanoporous Gold and Their Binding of Soybean Agglutinin. *Carbohydr. Res.* **2013**, *373*, 9-17.
6. Pandey, B.; Bhattarai, J. K.; Pornsuriyasak, P.; Fujikawa, K.; Catania, R.; Demchenko, A. V.; Stine, K. J., Square-Wave Voltammetry Assays for Glycoproteins on Nanoporous Gold. *J. Electroanal. Chem.* **2014**, *717*, 47-60.

CHAPTER 3 PREPARATION, MODIFICATION AND APPLICATION OF NANOPOROUS GOLD

3.1 Introduction

Nanoporous gold (NPG) is a three-dimensional sponge like structure of gold¹ having size of pores (interligament gaps) and ligaments width on the order of a few nanometers to a few hundreds of nanometers.² The SEM image of an NPG plate is shown in **Figure 3.1**.

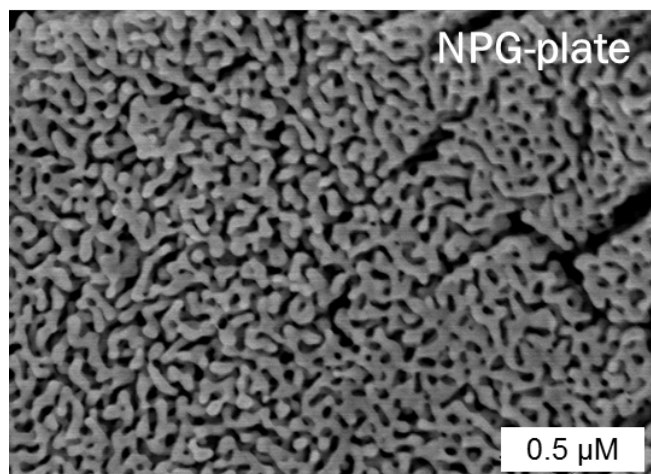


Figure 3.1 SEM image of an NPG plate prepared by dealloying commercially available 10K white gold in concentrated nitric acid for 48 h.

NPG is of much interest to scientists because of its high surface area-to-volume ratio, ease of preparation and modification, biocompatibility, conductivity, chemical and physical stability, and regenerative nature.³ Moreover, it has the ability to serve as a support for stable self-assembled monolayers (SAMs) of organic molecules on its surface because of strong thiol-gold bonding.⁴

Because of these properties, NPG has applications in a wide variety of fields. NPG has been used as a catalyst for oxidizing and reducing different gas and liquid molecules. In one study, selective oxidative coupling of methanol was successfully performed to yield methyl formate, which is an important precursor for formic acid, formamide, and dimethyl formamide synthesis.⁵ There are numbers of other examples where NPG was used as a catalyst, some of them include, carbon monoxide oxidation at low temperature,⁶ reduction of oxygen to hydrogen peroxide first and then to water,⁷ aerobic oxidation of D-glucose to D-gluconic acid⁸ and organosilane oxidation with water⁹. NPG has also been used as a surface-chemistry-driven actuator converting chemical energy directly into a mechanical response.¹⁰ Protein immobilization,^{4, 11} sensing,¹²⁻¹⁴ and most recently plasmonics¹⁵⁻¹⁷ are the other fields where the use of NPG can be found (**Figure 3.2**).

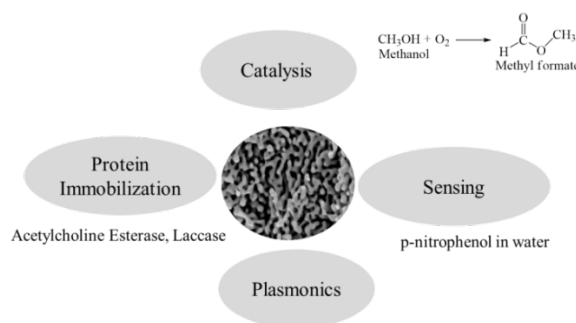


Figure 3.2 Cartoon showing applications of NPG in different fields.

Because of the wide variety of applications of NPG, more research needed to be performed, and better ways to synthesize and control the pores and ligaments of NPG have to be explored. Two common methods of preparation of NPG are wet chemical methods and electrochemical methods. In both of these methods, the very first step is to prepare or obtain an appropriate alloy of gold with other less noble metal(s). Finally, the

less noble metal or metals in an alloy is selectively dissolved by either putting the alloy in a corrosive environment (e.g., acids) or by applying an electrochemical potential (**Figures 3.3 and 3.4**).¹⁸⁻¹⁹ If the dealloying is performed by applying a potential, it is called electrochemical dealloying and if done without a potential, chemical dealloying. The shape and size of the interligament gaps and ligaments width of NPG formed depend on several factors, including compositional ratio, type of alloy,²⁰⁻²² electrodeposition potential, corrosive environment, dealloying time,²³ dealloying temperature,²⁴ and dealloying potential. Once NPG is formed, the width of interligament gaps and ligaments can still be further tuned by annealing at different temperatures for different times²⁵ or electrochemically by applying cyclic potential sweep for different number of cycles in different electrolyte solutions. The advantages of the electrochemical fabrication method of metal nanostructures over other techniques are that structures can be formed without the need of templates, surfactants or any other stabilizers that can introduce heterogeneous impurity. In this chapter, we have (a) explored the effects of various dependable parameters in electrochemical fabrication of nanoporous gold (b) modified already formed NPG by electrochemical annealing to increase the pores or interligament gaps size, and (c) used NPG as a substrate to study interactions of biomolecules, mainly carbohydrate–protein interactions.

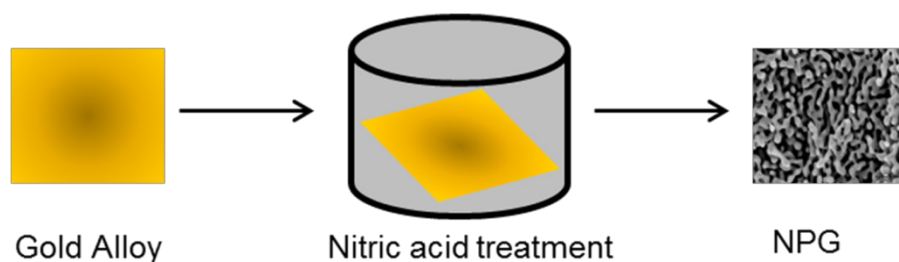


Figure 3.3 Schematic diagram of wet chemical method of preparing NPG.

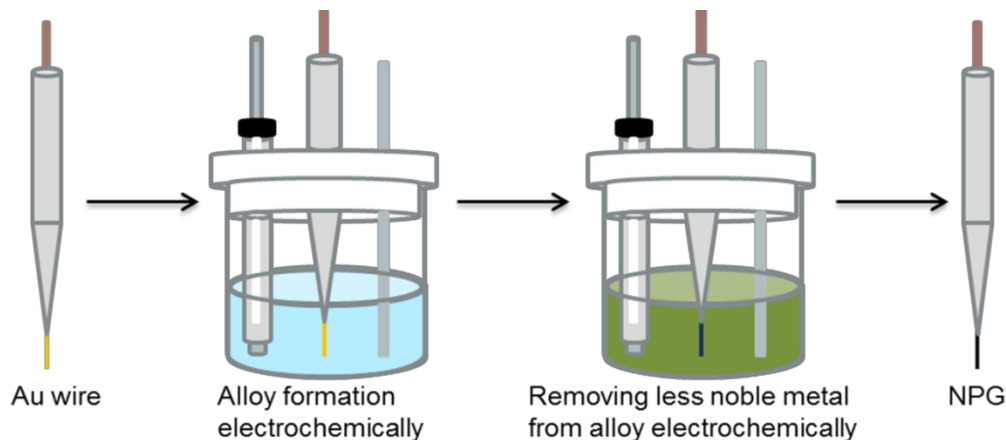


Figure 3.4 Schematic of electrochemical method of preparing NPG on a gold wire.

3.2 Results and Discussion

3.2.1 Fabrication of NPG on gold wire

NPG-coated gold wires have been prepared electrochemically in our lab previously for the detection of the free prostate specific antigen.²⁶ However, the detailed morphological changes of NPG-coated gold wires while changing different variables were still to be explored. By studying the effects of variables, the optimal conditions for preparing NPG with desired pores and ligaments size can be obtained, for applying it in different fields of research.

3.2.1.1 Effects of potential

NPG-coated gold wires prepared at different deposition potential, compositional ratio of gold and silver, and deposition time were compared. **Figure 3.5** shows the cyclic voltammograms of NPG-coated gold wires prepared at -1.0 , -1.2 and -1.4 V deposition potentials for 10 min from electrolyte mixtures consisting of 250 mM sodium carbonate and 30:70% 50 mM $\text{K}[\text{Au}(\text{CN})_2]$ and 50 mM $\text{K}[\text{Ag}(\text{CN})_2]$, respectively, followed by

dealloying in concentrated nitric acid for 24 h. We have found that when the potential was changed from -1.0 to -1.2 V the surface area of the NPG-coated gold wire increased from 12 ± 2 to 16 ± 2 cm². This is because of an increase in total amount of mass deposited on gold wire by increasing amount of current flowing in the solution. However, the NPG-coated gold wire prepared at -1.4 V was fragile and surface area was found to vary significantly because of visually evident loss of NPG structures.

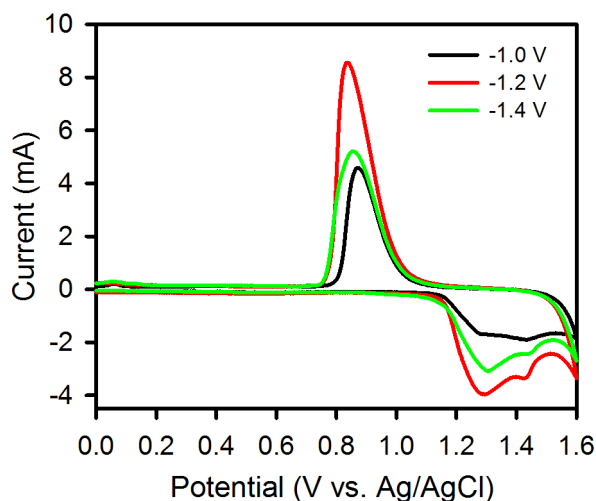


Figure 3.5 Cyclic voltammograms of NPG-coated gold wires prepared by applying different deposition potentials.

SEM images of NPG-coated gold wires prepared by applying different deposition potentials are shown in **Figure 3.6**. It has been found that the surface morphology changes drastically with a change in potential of $+0.2$ V. We have found that morphology of the NPG-coated gold wire prepared at -1.0 V is smoother compared to structures formed at -1.2 V and -1.4 V. We have also found that at -1.2 V, globular structures were formed and at -1.4 V, dendritic structures were formed. The reason for the physical instability of the structures formed at -1.4 V is obvious from the SEM images. As can be

seen in the images, the structures formed at -1.4 V are taller and thinner making it more susceptible to breakage by even the gentle force of water while cleaning.

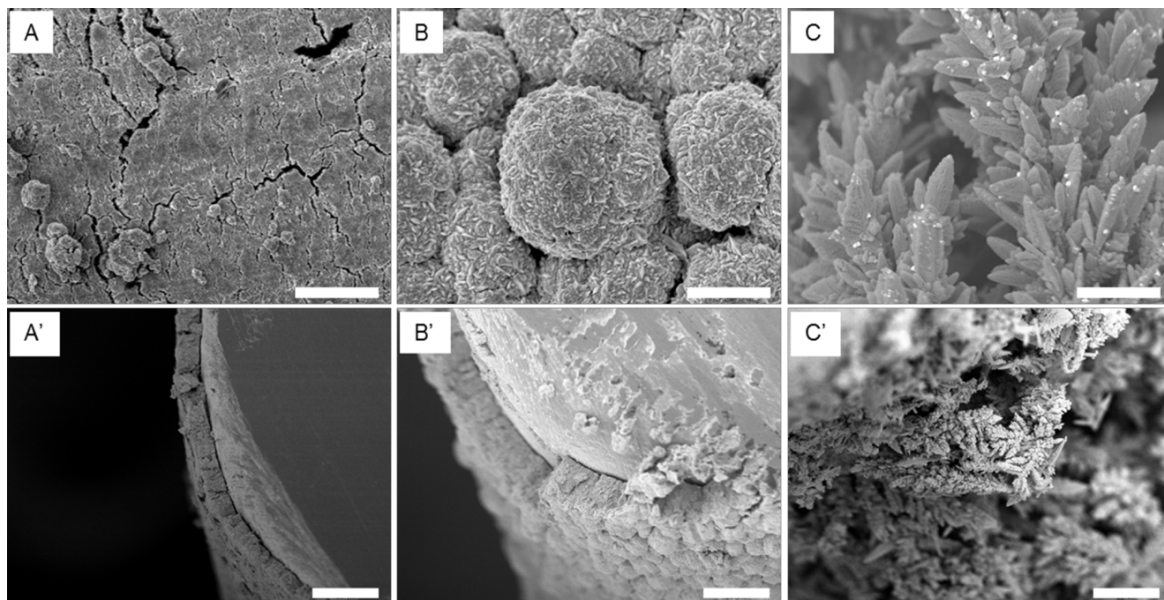


Figure 3.6 Low-magnification SEM images of NPG-coated gold wires prepared at (A) -1.0 V, (B) -1.2 V and (C) -1.6 V for 10 min showing change in morphological features with changing potential. Scale bar: $5\text{ }\mu\text{m}$. (A'), (B') and (C') are the low-magnification cross sectional of (A), (B) and (C), respectively, showing change in thickness. Scale bar: $20\text{ }\mu\text{m}$.

The composition of the NPG-coated gold wire before and after dealloying is determined by EDX spectroscopy (**Figure 3.7**). Before dealloying, a significant portion of silver is present in an alloy represented by peak at 2.98 keV (L-Shell), which disappears after dealloying showing only the characteristics peaks of gold at 2.12 keV (M-shell) and 9.7 keV (L-Shell).

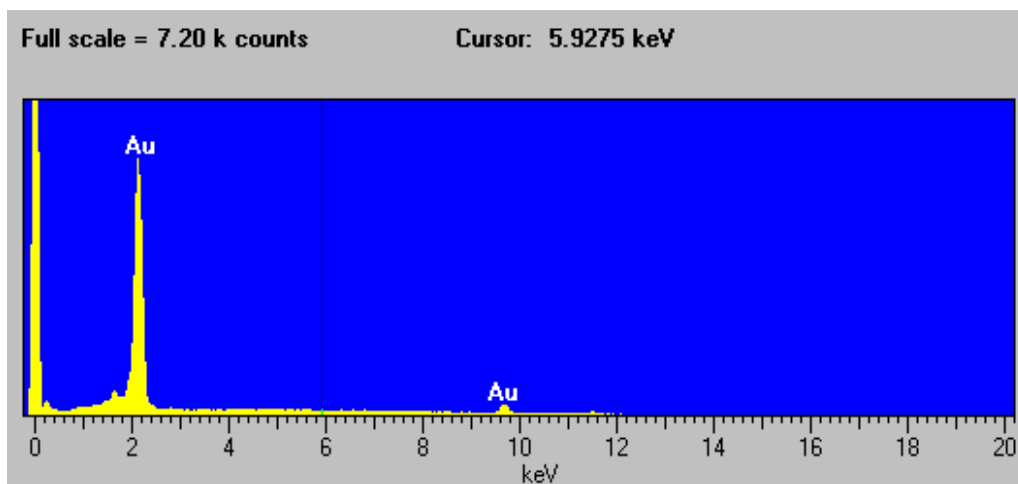


Figure 3.7 EDX elemental analysis of an NPG-coated gold wire shows only the presence gold after dealloying.

From the above data, we can infer that deposition at -1.4 V is not suitable condition for making NPG on gold wire to be used as an electrode or a substrate for biomolecule immobilization. Deposition at -1.0 and -1.2 V are physically stable with -1.2 V deposition having a globular structure and higher surface area. In the experiments where a smooth morphology is preferred, a -1.0 V deposition condition can be a better option.

3.2.1.2 Effects of compositional ratio and deposition time

Figure 3.8A shows cyclic voltammograms of NPG-coated gold wires prepared using different compositional ratio of gold and silver. We have found that NPG-coated gold wires prepared from alloy of Au₃₀Ag₇₀ forms higher surface area compared to NPG prepared by other compositional ratios, Au₂₀Ag₈₀, Au₄₀Ag₆₀, and Au₅₀Ag₅₀.

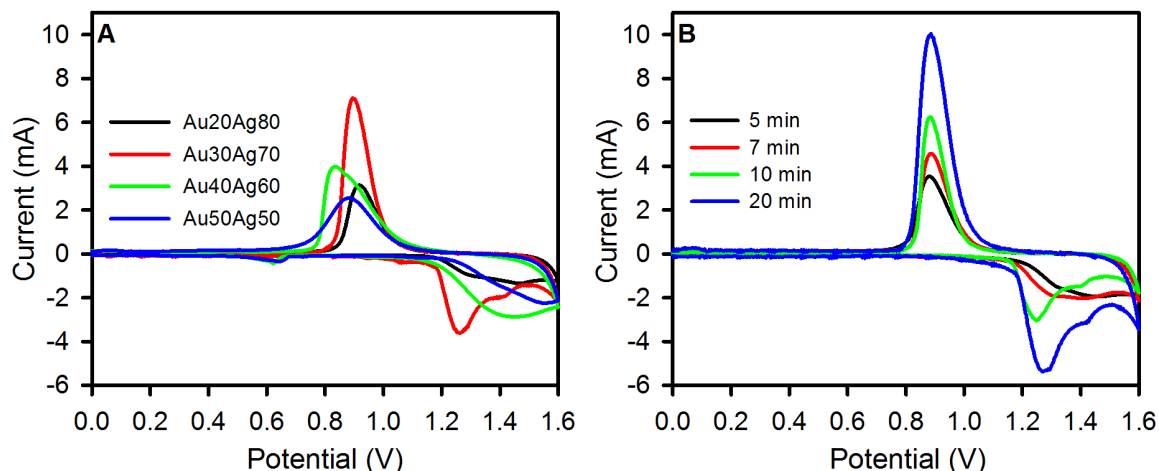


Figure 3.8 CV of NPG-coated gold wires prepared at different (A) ratio of Au and Ag solution for 10 min and (B) deposition time with Au30Ag70 ratio, deposition potential = -1.2 V.

Figure 3.8B shows CVs of NPG-coated gold wire prepared at deposition time 5, 7, 10, and 20 min. We have found that surface area increases with increase in time, which must be due to an increase in thickness and can be seen in cross-sectional SEM images (**Figure 3.9**). It can be seen that an NPG-coated gold wire prepared at -1.0 V for 10 min is 75 nm thick (**Figure 3.9A**), thinner than the one prepared at -1.0 V for 20 min, which is 150 nm thick (**Figure 3.9A'**). However, NPG-coated gold wires prepared by using a deposition time of 20 min at -1.2 and -1.4 V were found to be physically unstable. In fact, it has been found that the NPG prepared at -1.4 V for 5 min or more is fragile and can easily peel off of gold wire. Physically stable NPG at -1.4 V can be formed by applying the potential only up to 4 min or less, SEM images of which are shown in **Figure 3.9B and B'** for 1 min and 4 min, respectively.

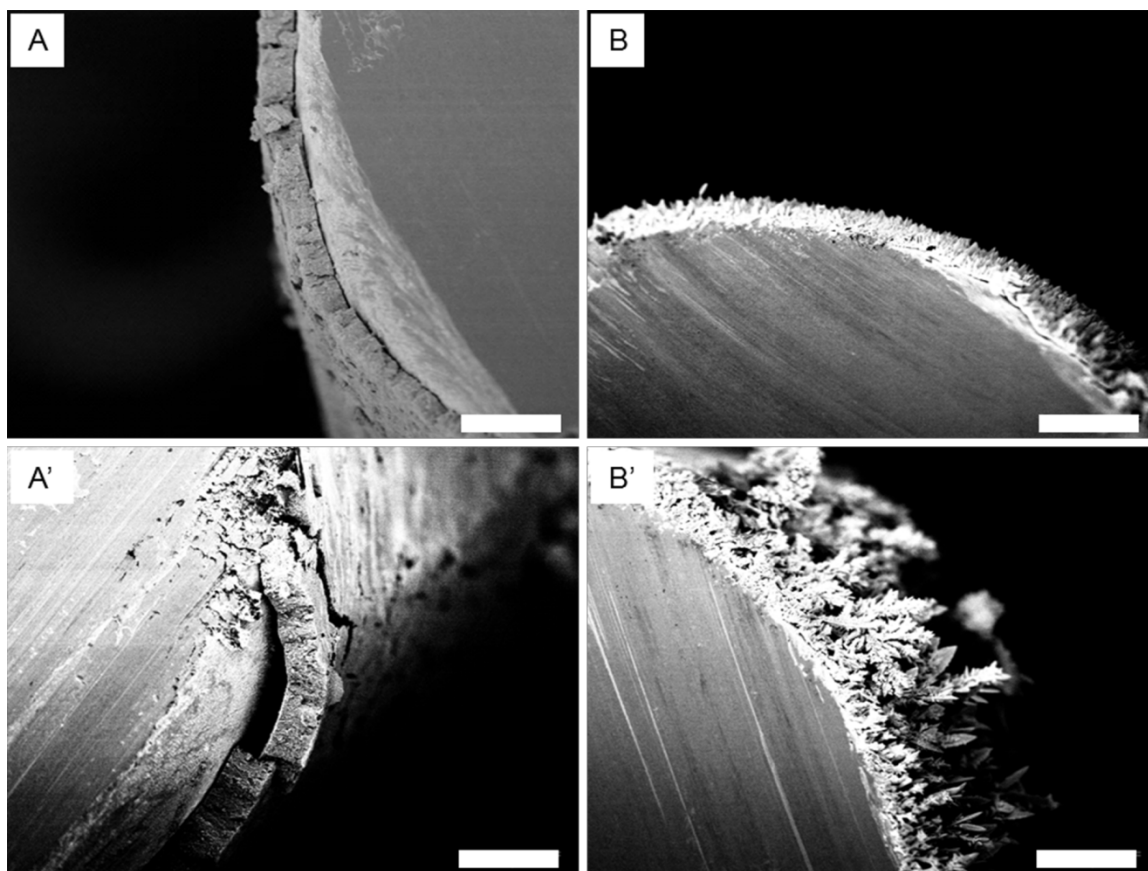


Figure 3.9 Increase in thickness of NPG-coated gold wires with the deposition time. (A) 10 min and (A') 20 min at deposition potential -1.0 V, and (B) 1 min and (B') 4 min at -1.4 V. Scale bar: $20\text{ }\mu\text{m}$.

From these data, we can conclude that deposition at -1.0 V forms an alloy with a smoother NPG morphology, compared to the morphology formed from the alloy prepared at -1.2 V deposition potential which forms spherical structures. NPG prepared under both of these conditions are physically robust. However, structures formed from an alloy deposited at -1.4 V are tree-like dendritic structures, but fragile. We have found that NPG prepared from electrolyte solution of Au₃₀Ag₇₀ ratio gives a higher surface area. The surface area also increases linearly with the increase in deposition time.

Table 3.1 Surface area comparison of NPG-coated gold wires under different conditions.

Atomic Ratio Au:Ag	Deposition Time (min)	Charge (μC)	Surface Area (cm^2)	Atomic Ratio Au:Ag	Deposition Time (min)	Charge (μC)	Surface Area (cm^2)
	5	2266	5.03		5	5562	12.37
20:80	7	2988	6.64	40:60	7	6543	14.54
	10	4052	9.00		10	7234	16.07
	5	4942	10.98		5	340.9	0.75
30:70	7	5511	12.24	50:50	7	359.4	0.79
	10	7960	17.68		10	515.5	1.14
Bare Au wire				Theoretically calculated surface area of bare wire = 0.0317 cm^2			

3.2.2 Fabrication of NPG on flat gold

NPG prepared on gold wire is good as a working electrode for electrochemical detection of biomolecules, however, it is not flat enough to be used as an optical sensor since optical sensing technique like localized surface plasmon resonance spectroscopy uses incident light beam with diameter around 4 mm. To address the problem, we made thin films of NPG on a rectangular flat gold prepared on glass slide having dimensions $1 \text{ cm} \times 1.25 \text{ cm}$, so that we could use it as both an electrochemical and optical biosensor.

The deposition potential for preparing the NPG films was choose to be -1.2 V from Au30Ag70 solution as it has been found initially that under this condition a higher surface area, rough but stable structure could be created. We chose a deposition time of 1 min so that a thin film prepared on flat gold surface is stable, and we explored the effects of the dealloying potential and dealloying time on formation of NPG.

3.2.2.1 Effects of dealloying potential

Figure 3.10A–C shows the SEM images of NPG films prepared at $+1.0$, $+1.2$, and $+1.4$ V dealloying potential in KNO_3 for 1 min. We don't see much difference just by looking at images as comparable pores sizes can be seen in all the three images. However, the diameter of pores are 7 ± 1.5 , 9 ± 2 , and 10 ± 2 nm for the structures prepared at $+1.0$, 1.2 , and $+1.4$ V dealloying potential, respectively. It was also found that the structure formed at $+1.0$ V has fewer surface defects compared to the structures formed at $+1.2$ V and $+1.4$ V dealloying potentials. When we took EDX spectra of the as-prepared structures, the gold and silver composition ratio vary significantly, with the structure prepared at $+1.0$ V having Au:Ag in the ratio of 46:54, $+1.2$ V having Au:Ag in ratio of 76:24, and $+1.4$ V having Au:Ag in ratio of 80:20 (**Figure 3.10A'–C'**). This shows that even though potential does not play much role in determining the size of porous structure, it plays an important role in determining the compositional ratio of gold and silver in the structure formed under these conditions.

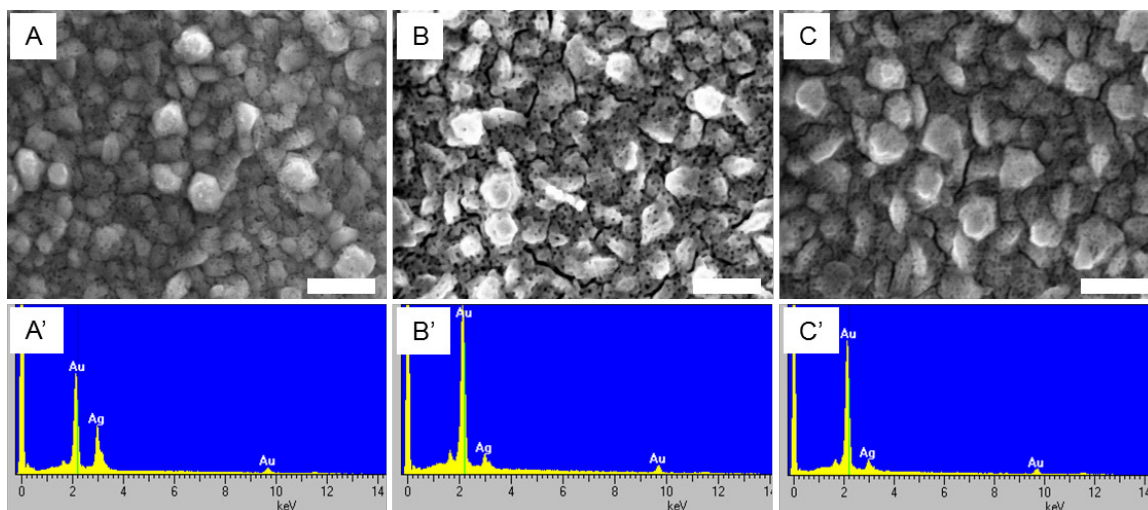


Figure 3.10 SEM images of electrochemically prepared NPG films after Au₃₀Ag₇₀ alloying at -1.2 V and dealloying at (A) $+1.0$ V, (B) $+1.2$ V, and (C) $+1.4$ V in KNO₃ for 1 min. Scale bar: 200 nm. (A'), (B') and (C') are the corresponding EDX spectra showing changing Au to Ag ratio with changing potential.

3.2.2.2 Effects of electrochemically dealloying time

The structures formed by changing different potentials for 1 min consistently form the structures that have a higher content of silver. The next step we performed was the change of the dealloying time while keeping the potential constant. For this experiment, we kept the potential at $+1.0$ V and changed the dealloying time with the increments of 1 min. The SEM images of the NPG films prepared at 1, 6, and 12 min are shown in **Figure 11A–C**, whereas **Figure 11D** is an NPG plate prepared by nitric acid dealloying for 48 h. It has been found that upon increasing the dealloying time, the width of the ligament and diameter of pores increases linearly. The pore size of the NPG film which was 7 ± 1.5 nm at 1 min changed to 39 ± 13 nm after 12 min of dealloying, and has ligament width of 40 ± 14 nm. Looking at the standard deviation of the structures

prepared at 1 and 12 min, it can also be inferred that with increasing dealloying time, randomness in pore and ligament size increases.

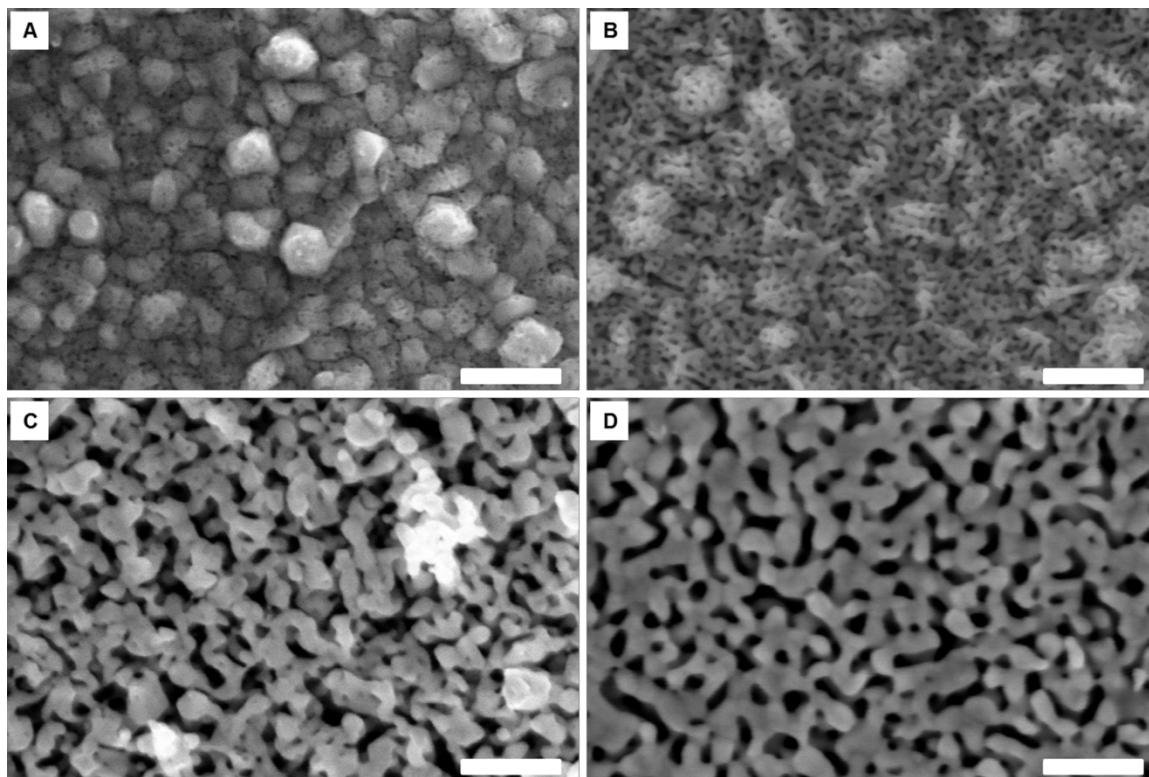


Figure 3.11 (A–C) SEM images of NPG films prepared by electrochemical dealloying for 1 min, 6 min and 12 min, and (D) NPG plate prepared by nitric acid dealloying of commercially available alloy plate for 48 h. Scale bar: 200 nm.

When we checked the EDX spectrum of the structure prepared at +1.0 V for 12 min, we found that there were still nearly 5% of silver left in the structure, which we concluded is difficult to remove as we saw the same amount even after 30 min of dealloying time. We also checked the reflection spectra of the structures formed. We have found that all the structures formed show characteristic inverse reflectance peaks, which doesn't appear for flat gold plate. The spectrum red shifts in peak wavelength and

becomes broader increasing the full width at half maxima with the increasing dealloying time (**Figure 3.12**).

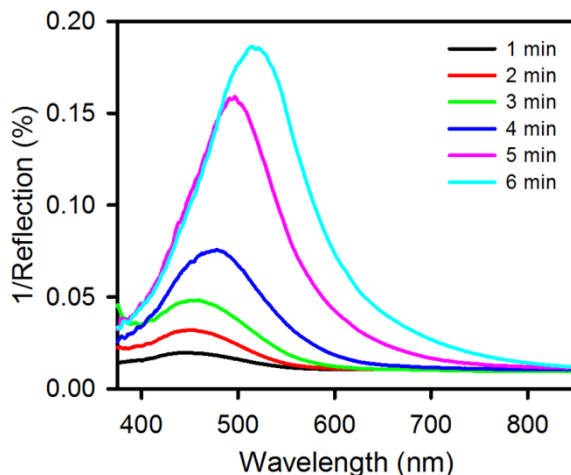


Figure 3.12 Reflection spectra of electrochemically prepared NPG films using a dealloying potential of +1.0 V (vs. Ag/AgCl, satd. KCl) for different dealloying times.

3.2.2.3 Bulk refractive index sensitivity (RIS) of NPG films

The bulk RIS of the NPG films prepared on a flat gold surface was evaluated by measuring reflection spectra from the NPG films in air, water, and organic solvents (ethanol and toluene). The refractive indices of air, water, ethanol, and toluene are 1.00, 1.33, 1.36, and 1.495 respectively. The NPG films were found stable after the use of organic solvents. With the increase in refractive index of the surrounding medium, a red shift of the surface plasmon band and decrease in reflection intensity can be observed. Unlike some of the previously reported experiments, where wavelength shows nearly linear response but intensity is random with change in refractive index,²⁷ the NPG films show a nearly linear response in both wavelength and inverse reflectance with the change in the refractive index of the surrounding medium (**Figure 3.13**). Since NPG films shown linear response to both inverse reflectance and wavelength, it can be used as a LSPR

transducer based on both parameters. **Figure 3.13** is the representative bulk RIS test performed for the NPG film prepared from alloy deposited at -1.2 V for 1 min followed by applying a dealloying potential of $+1.0$ V for 1 min. The bulk RIS is found from slope of peak wavelength versus refractive index and is 112 nm RIU^{-1} .

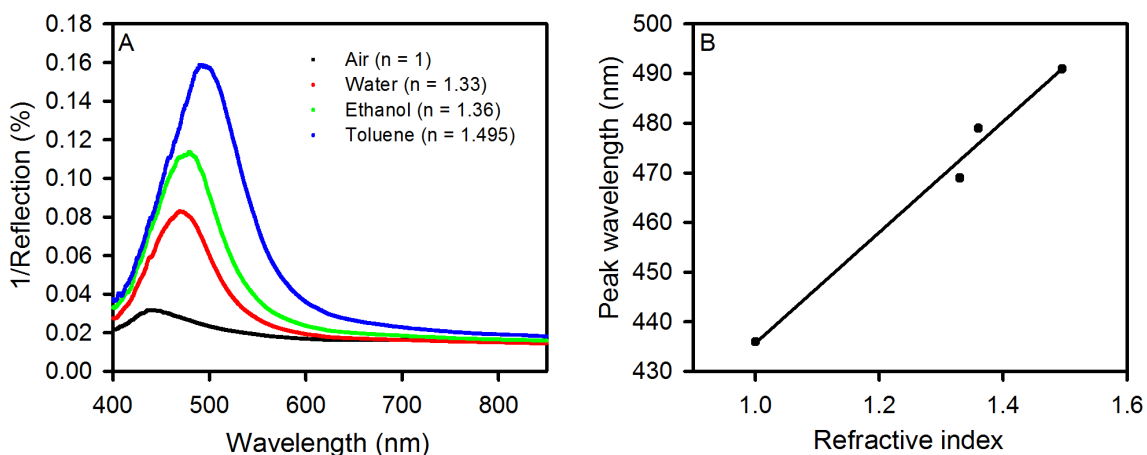


Figure 3.13 Bulk RIS test of the NPG film prepared using alloying deposition potential of -1.2 V for 1 min and dealloying potential of $+1.0$ V for 1 min. (A) LSPR spectra obtained at different RI, 1, 1.33, 1.36, and 1.495 using air, water, ethanol, and toluene respectively, represented by lines of different colors. (B) Plot of peak wavelength versus RI showing linear dependence.

Comparison of bulk RIS of NPG films prepared under different conditions are shown in **Table 3.2**. It can be seen that the NPG films prepared by using an alloy deposition potential of -1.2 V and dealloying potential of $+1.0$ V give better sensitivity compared to other preparation conditions. The reason for lower dealloying potentials giving higher sensitivity should be because of presence of a higher amount of residual silver in the NPG formed, as can see through EDX data (**Figure 3.10A**). It has been found earlier that silver films can show better RIS compared to gold but are not very

stable to open environment and can form an oxide layer. We have shown before that structures formed at alloys deposited at lower potential have sharper features, so the RIS is greater for structures prepared by deposition at -1.2 V compared to that prepared by deposition at -1.0 V. However, structures of alloy formed at -1.4 are physically not very stable. Even the stable structures formed don't show better sensitivity which might be because of easier removal of silver from the alloy formed upon dealloying.

Table 3.2 Comparison of RIS of NPG films formed on flat gold surface at 1 min of deposition and dealloying time.

Deposition potential	Dealloying potential	Sensitivity (nm/RIU)
-1.0 V	+1.0 V	60
	+1.2 V	51
-1.2 V	+1.0 V	115
	+1.2 V	80
-1.4 V	+1.0 V	81
	+1.2 V	32

3.2.3 Post-modification of NPG-coated gold wire

The width of gaps and ligaments of NPG can not only be controlled while preparing them but also can be controlled after NPG is already formed, called post-modification. Controlling the width of gaps and ligaments of NPG allows us to use them

for immobilizing biomolecules of a wider variety of shape and size more efficiently. The most common method of post-modification is thermal annealing and has been reported previously.²⁸ However, NPG can also be modified using acid treatment for an extended period of time and electrochemical annealing, which we will be exploring in detail. The underlying mechanism of annealing can be explained using surface diffusion of gold atoms. The increase in surface diffusion of gold atoms leads to the growth in the ligament size, eventually increasing the size of pores and interligament gaps.²⁹

3.2.3.1 Acid treatment for extended period

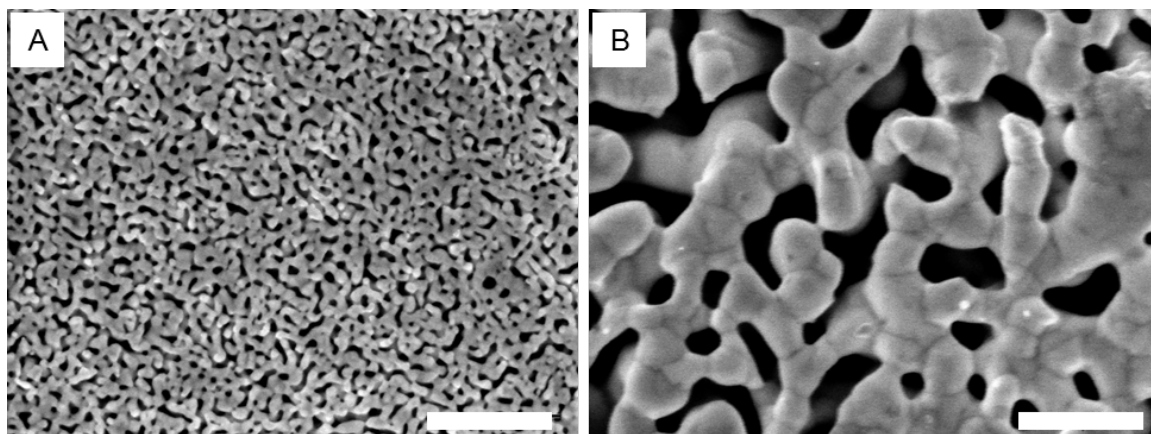


Figure 3.14 SEM images of NPG plate prepared by dealloying for (A) 48 h and (B) 42 days showing change in width of gaps and ligaments. Scale bar: 500 nm.

Figure 3.14 is SEM images of NPG plate showing effect of acid treatment on width of gaps and ligaments. **Figure 3.14A** is SEM image of NPG plate prepared by dealloying the commercially available gold alloy for 48 h. The average interligament gap and ligament width of the NPG plate formed are 27 ± 7 and 38 ± 8 nm respectively. However, when the NPG plate is prepared by dealloying for 42 days both the average

gaps and ligaments width increases linearly to 115 ± 32 and 160 ± 47 nm, (**Figure 3.14B**).

3.2.3.2 Electrochemical annealing of NPG-coated gold wire

Electrochemical annealing could be useful when thermal or acid treatment is not possible or convenient. This technique also provides an additional tool for adjustment of NPG pore size and surface area. Here, in this electrochemical method, once the NPG was formed on gold wire, it was annealed using cyclic potential sweeps of 30 or 50 oxidation–reduction cycles. Three different electrolyte solutions 0.1 M KCl or 0.1 M NaNO₃ or 0.1 M NaClO₄ were used and a potential was applied from -0.4 to $+1.2$ V using a 2 s hold at the positive end and a 8 s hold at the negative end at 100 mV s^{-1} . Total cycles were performed with 5-cycles increments while recording the surface area after every 5-cycle.

Cycling in these electrolyte solutions leads to annealing of NPG as is evident from the decrease in the peak current of cyclic voltammograms corresponding to gold oxide reduction (**Figure 3.15A–C**). There are fewer space exchange reactions between gold and oxygen, which occur when a monolayer of the oxide is formed or reduced. In **Figure 3.15D**, the current versus potential sweeps are shown during the electrochemical cycling process in 0.1 M KCl. The earlier scans (fifth scan), show features associated with the presence of some residual silver, which is greatly diminished in later scans. The surface area determined after every additional 5-cycles of annealing is shown in **Figure 3.16** for NPG-coated gold wires annealed in these three electrolyte solutions. In order to account for modest variations in the initial surface area of the three different NPG-coated gold electrodes, the changes in area versus cycle number are shown as A/A_0 for each trial

where A_0 is the initial NPG surface area for that trial. The value of A_0 found for eight trials was 21.0 ± 2.0 nm.

Comparisons between different electrolytes where anions serve as an adsorbate can help determine the effect of an anion adsorption on the relative mobility of the surface Au atoms.³⁰ Nitrate and perchlorate are both oxyanions that are expected to be physisorbed weakly through interaction of one or more oxygen atoms with the Au surface. Their overall effect on surface area annealing after 50 electrochemical cycles as indicated is found to be similar. These weakly adsorbed anions enhance the mobility of the Au atoms and promote the increase in the pore sizes. The adsorption of anions in solutions is expected to take place favorably at potentials above the potential of zero charge (pzc). The pzc in 0.01 M HNO_3 has been reported as near 0.0 V, with a higher value near 0.23 V (vs. SCE) reported in 0.01 M NaClO_4 . We also performed experiments wherein rather than cycling we let the electrodes sit at a positive potential of 0.4 V for 15 min to note any structural changes brought about on the electrodes. However, there was no change as observed from the SEM images for the wires and we can safely conclude that electrochemical cycling under the stated conditions induces changes in the NPG that are not found on holding the electrodes at a fixed potential of 0.4 V.

Another solution used for annealing is 0.1 M KCl in which we see greater annealing and most of the enhanced surface area due to NPG is eroded by 50 cycles. Since NPG was seen to be essentially removed from the Au wire surface by 50 cycles, it was decided to perform only 30 cycles during which we found the decrease in surface area (67% reduction) was substantially larger than that seen for the 50 cycles performed on the other two solutions (24% reduction in perchlorate and 24% reduction in nitrate).

Diaz et al. studied gold dissolution using different $\text{Au}^+/\text{Au}^{3+}$ ratios. They analyzed the thermodynamics and kinetics of the current potential equation to conclude that AuCl_4 was formed at a potential more positive than 0.8 V (vs. SCE) and AuCl_2 was formed at potentials below 0.8 V (vs. SCE).³¹ Investigations have shown that strongly absorbed chloride ions on Au(111) lead to an increase in gold surface diffusion with a reduction in the anodic dissolution due to oxide layer formation in a solution which contained chloride ions.³² The cycling performed in 0.1 M KCl solution for 30 cycles led to a greater decrease in surface area than in the other solutions and we investigated the change in the electrolyte solution (to a pale yellow) after cycling using UV–Vis spectroscopy. It was found that 0.291 mg of gold was removed from the electrode surface and dissolved into the solution as the gold chloride complex (AuCl_4^-). The ϵ for AuCl_4^- at $\lambda_{\text{max}} = 323$ nm is $5800 \text{ l}/(\text{M cm})$ ³³ and an absorbance value of 0.9533 was recorded giving AuCl_4 concentration of 0.164 mM in the solution in the electrochemical cell. We see a substantial decrease in surface area on exposure of the NPG-coated gold wires to electrochemical cycling in KCl solution. It can be postulated that in presence of chloride in solution, there is rapid motion of the step edges and increased atomic mobility can be argued due to bonding of the surface gold atoms to the adsorbate. This bonding can be stronger than the neighboring gold atom bonding which shall in turn increase substantially the mobility of the gold atoms thus increasing the pore sizes. However, the Au surface in this case erodes due to formation of the soluble complex ion.

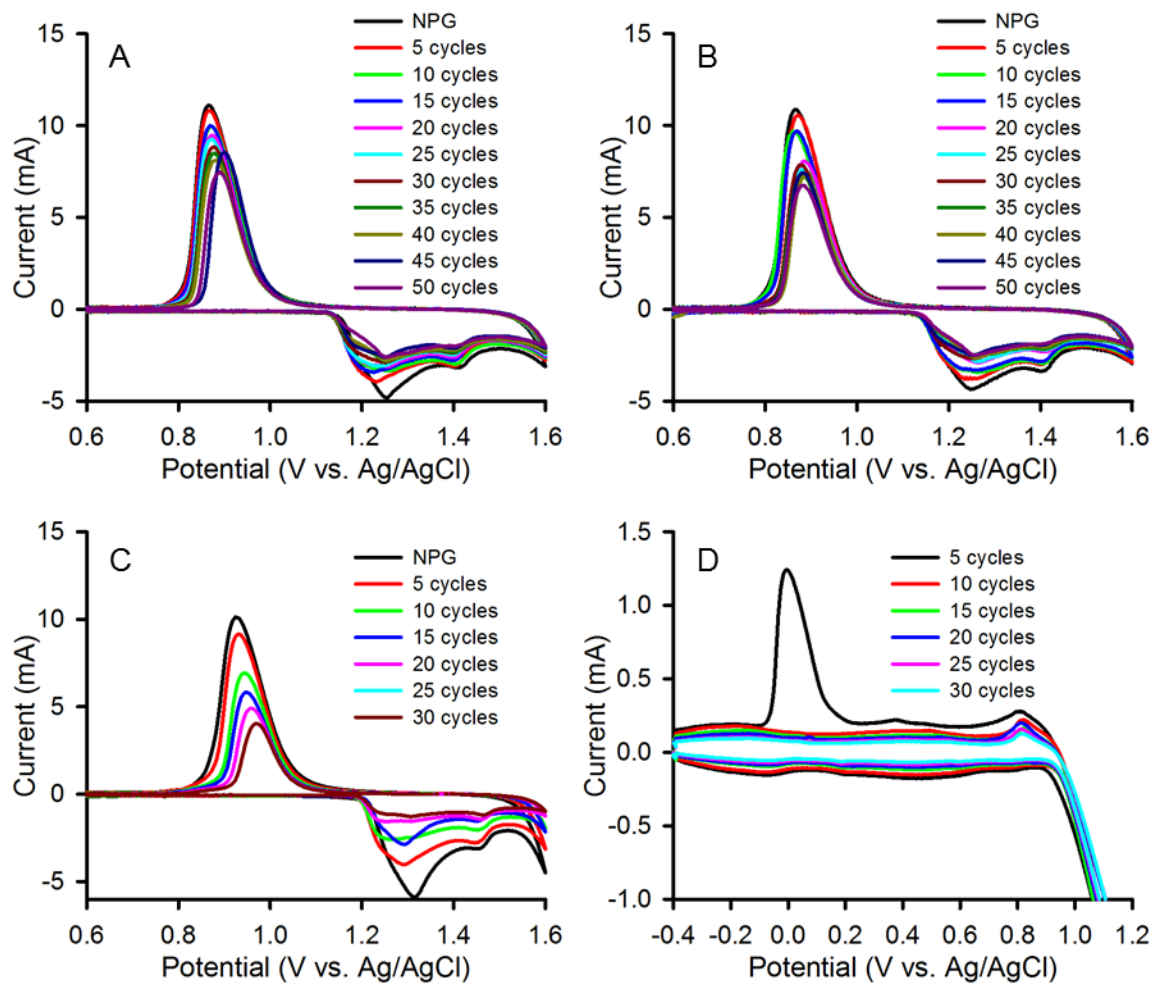


Figure 3.15 Cyclic voltammograms used to determine gold surface area by oxide formation and reduction for NPG annealed in: (A) 0.1 M NaClO_4 and (B) 0.1 M NaNO_3 for 50 oxidation–reduction cycles, shown after every 5 cycle, (C) similar CV scans shown for annealing of NPG performed for 30 cycles in 0.1 M KCl, with data shown after every fifth cycle. (D) The CV scans recorded during application of the 30 annealing cycles in 0.1 M KCl. Scan rate = 100 mV s^{-1} .

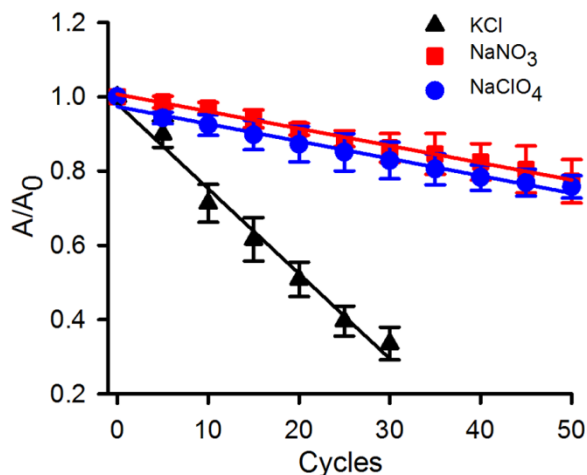


Figure 3.16 Surface area reduction after annealing in different electrolyte solutions using electrochemical cycling performed in 0.1 M NaClO₄, 0.1 M NaNO₃, and 0.1 M KCl. The values of A₀ are 21 ± 2 cm². The error bars represent the standard deviations for 3 experiments in each case.

Surface morphology and pore size analysis.

Figure 3.17 shows the SEM images of NPG before and after annealing. It can be seen that NPG is morphologically changed after the annealing cycles creating bigger pores or interligament distances. Histograms in **Figure 3.18** show how interligament gaps and ligament widths are distributed in size. The average interligament gaps and ligament width of NPG prepared using nitric acid are found to be 39 ± 10 and 37 ± 10 nm, respectively (**Figure 3.18A,A'**). It should be noted that mean ligament widths and gaps of as-prepared NPG are comparable. When NPG was annealed in KCl using 30 cycles, interligament gaps and ligament widths are found to be 88 ± 26 and 55 ± 22 nm, respectively (**Figure 3.18B,B'**). Similarly, the NPG annealed in NaNO₃ has interligament gaps and ligament widths 76 ± 32 and 54 ± 14 nm, respectively, while those of NaClO₄ annealed NPG are 58 ± 15 and 49 ± 12 nm, respectively (**Figure 3.18D–E'**). It is

noteworthy that the NPG subjected to electrochemical annealing cycles, resulted in smaller ligament widths than the interligament gaps. This is the novelty of this technique as annealing performed using previously studied method creates structures having almost similar ligament's widths and gaps. From these results, it is also reasonable to conclude that both these dimensional parameters and the difference between them could be made even larger by increasing the number of cycles.

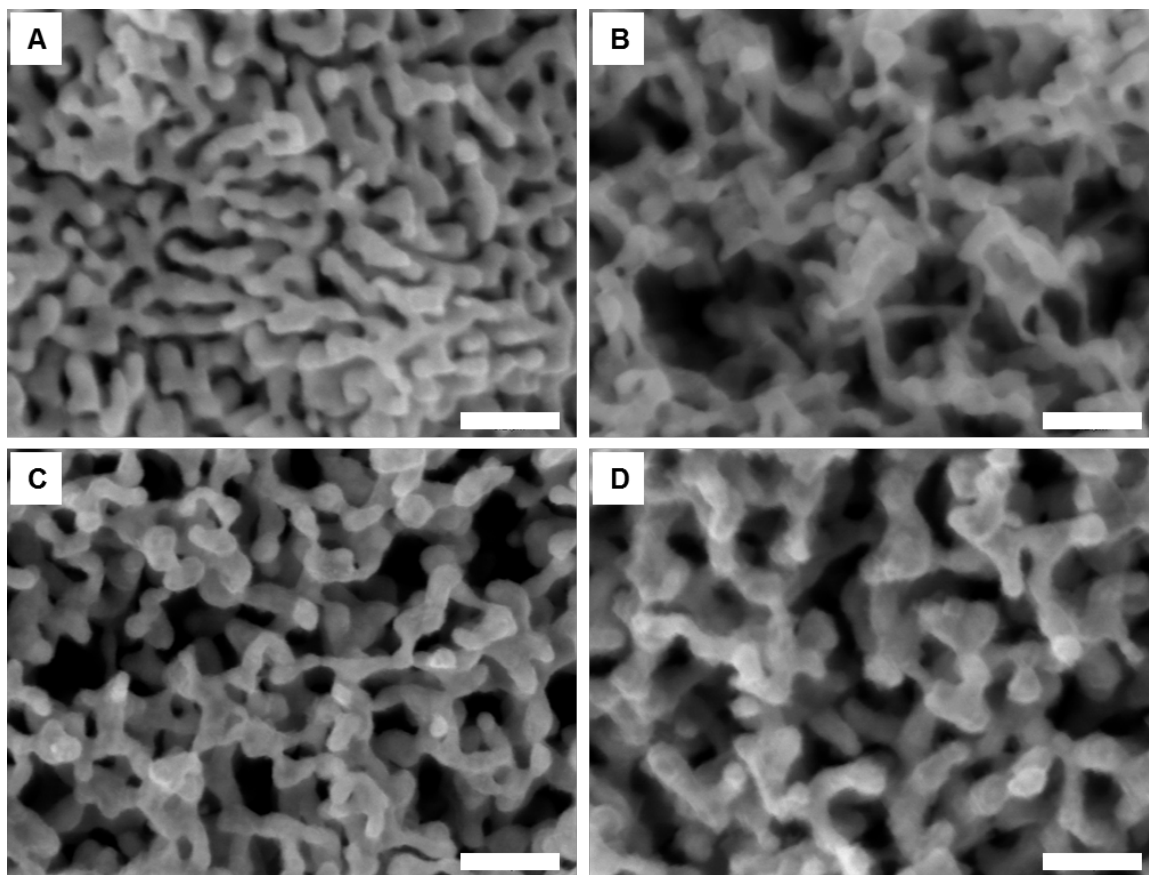


Figure 3.17 SEM images of NPG (A) unannealed (B-D) annealed, in KCl for 30 cycles, in NaNO₃ for 50 cycles and in NaClO₄ for 50 cycles, respectively. Scale bars: 200 nm.

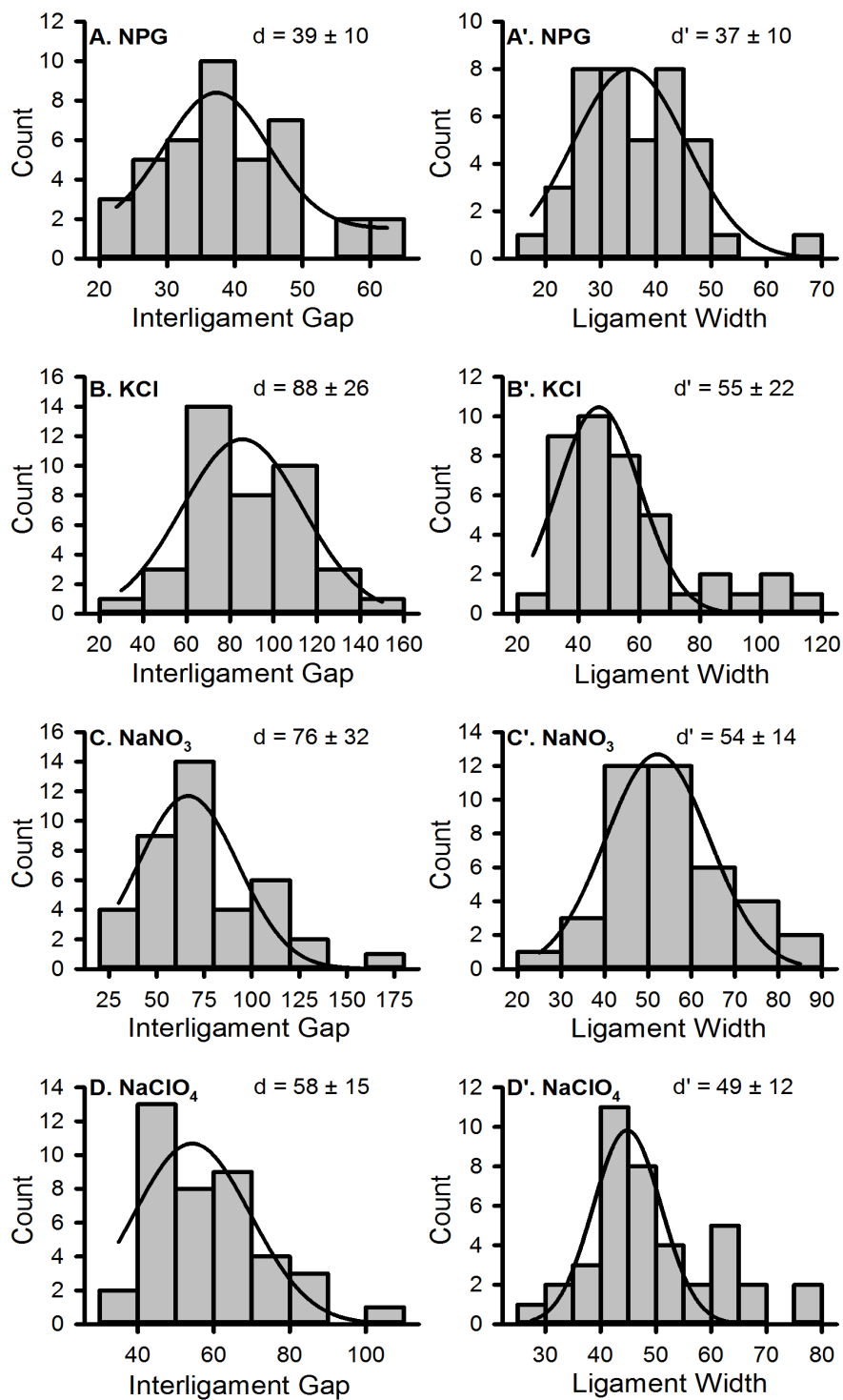


Figure 3.18 Interligament gap (A–D) and ligament width (A'–D') of nanoporous gold before (A and A') and after annealing under different solutions (B–D').

Accessible surface area to a diffusing redox probe.

The surface areas of the unannealed and annealed NPG-coated gold wire electrodes accessible to a diffusing redox probe during cyclic voltammetry sweeps were compared with those found for bare gold electrodes. These surface area values for NPG were significantly lower than those determined by the gold oxide stripping method and can be attributed to the relatively slow diffusion of the redox marker $\text{Fe}(\text{CN})_6^{3-/4-}$ (10 mM) into NPG from the bulk electrolyte solution. Since the interconnected ligaments and pores in the NPG create an irregular path we can assume that the diffusion of the redox marker during the sweep is limited to the outer NPG regions and the currents associated with its oxidation and reduction are not representative of the total NPG surface area. Depletion of the concentration of redox marker deeper inside the NPG structure which cannot be replenished by diffusion during the sweep should significantly limit the maximum currents observed even at the slowest scan rates used. In comparison, the gold oxide stripping method gives a more accurate approximation of the NPG surface area since the observed current is due to the oxidation and reduction of a monolayer of gold atoms on the NPG surfaces. The surface area for annealed and unannealed NPG remains higher than that of the bare gold wire which can be attributed to some extent to diffusion of the $\text{Fe}(\text{CN})_6^{3-/4-}$ into the NPG structure. The surface area was calculated using the Randles–Sevcik equation³⁴ where the anodic and cathodic peak currents were determined for a range of scan rates ranging from 20 mV s^{-1} to 200 mV s^{-1} . The plots of the cathodic and anodic peak currents versus the square root of the scan rate is shown in **Figure 3.19**, give an estimation of the electrochemically accessible surface area for NPG which is much smaller than the surface area calculated by the gold oxide stripping peak. The

surface area determined ($\approx 0.36\text{--}0.37\text{ cm}^2$) is only about 11 times the geometric surface area of the exposed gold wire (0.032 cm^2) compared to the surface area determined by gold oxide stripping ($21.0 \pm 2.0\text{ cm}^2$, $n = 8$) which is about 650 times the geometric surface area of the exposed gold wire.

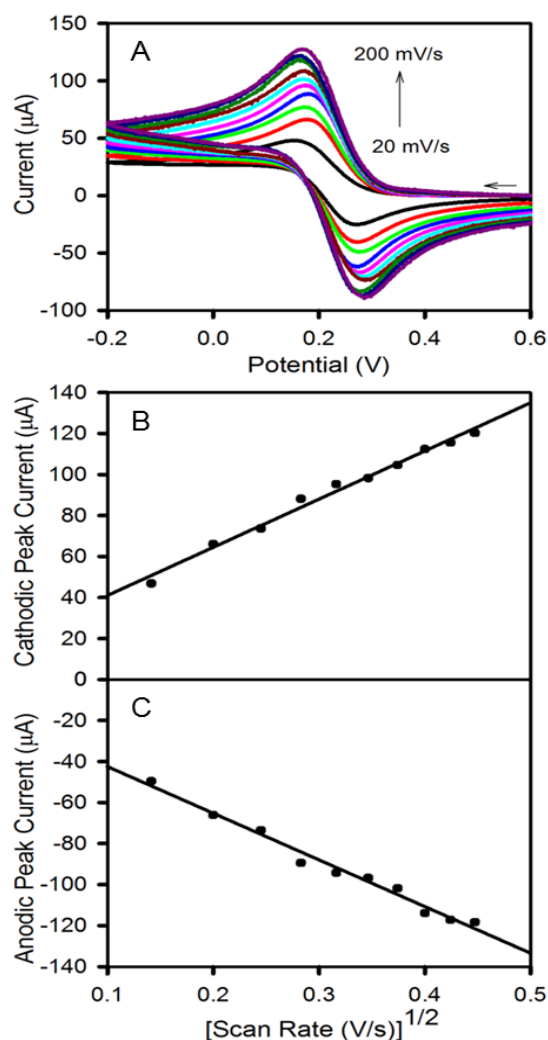


Figure 3.19 (A) Cyclic voltammograms for the determination of electrochemically accessible surface area, and (B,C) cathodic and anodic peak current versus the square root of the scan rate of flat gold wire showing linear dependency. The scans were from +0.6 to -0.2 V in $10\text{ mM K}_3[\text{Fe}(\text{CN})_6]$.

Table 3.3 Surface areas determined by both oxide stripping and use of a diffusing redox probe for the NPG-coated gold wire, annealed NPG-coated gold wire, and bare gold wire electrodes.

Method	NPG	Annealed in KCl	Annealed in NaNO ₃	Annealed in NaClO ₄	Flat Gold wire
Cathodic peak current (cm ²)	0.37 ± 0.02	0.19 ± 0.03	0.23 ± 0.02	0.32 ± 0.04	0.036 ± 0.003
Anodic peak current (cm ²)	0.36 ± 0.03	0.19 ± 0.03	0.22 ± 0.03	0.32 ± 0.05	0.0315 ± 0.0004
Oxide stripping (cm ²)	21 ± 2	7 ± 1	16 ± 1	16 ± 2	0.035 ± 0.001

3.2.4 Application of NPG

The high surface area-to-volume ratio of NPG, in conjunction with its high chemical and physical stability, ease of purification, and excellent conductivity makes NPG very attractive for protein immobilization,³⁵ and optical and electrochemical biosensing applications.³⁶⁻³⁷ When the goal is to improve sensitivity and lower detection limits, higher surface area electrodes are always preferred.

3.2.4.1 Protein immobilization

Immobilizing proteins on a substrate is a subject of interest to fields like proteomics, drug development, molecule separation, diagnosis, quality control and environmental monitoring.³⁸⁻³⁹ The most challenging part of the immobilization process

is maintaining the functionality of the immobilized protein.⁴⁰ To retain maximum biological activity of proteins, different methods are being used depending on physicochemical properties of the proteins used and the substrate onto which the proteins are immobilized.⁴¹ Though the chemically immobilized method strongly binds the proteins on the substrate and can also give the desired orientation, there is higher chances of denaturing or destroying the functionality of proteins while doing the chemistry between the foreign organic molecules with the molecules of the protein.⁴² Physical immobilization methods on the other hand are relatively better if orientation of the proteins molecules are not important in the experiment and binding between proteins and substrate is stronger.⁴³ Physical immobilization mainly occurs through ionic bonds and hydrophobic and polar interactions.⁴⁴ Our group has previously reported that nanoporous gold is a better substrate for protein immobilization with minimum denaturation, and protein can strongly bind to a gold surface.^{26, 45} In this part of the experiment, we have analyzed the physically bound protein on NPG surface using SEM. For this, we dipped half of the NPG wire into 20 μL of 1 mg mL^{-1} BSA solution for 5 min followed by air-drying. **Figure 3.20** shows SEM micrograph of the NPG wire half dipped in 1 mg mL^{-1} BSA solution for 5 min. It can be seen that there is a distinct color contrast between the BSA immobilized part (dark) and non-immobilized part (bright). The high-magnification SEM image near the boundary of protein immobilized and non-immobilized region clearly shows the protein moiety in the immobilized region. Low-magnification images of cross-section and top view of protein immobilized region shows thin BSA layers on NPG.

When we immobilized BSA on flat gold wire, high-density packing of BSA was observed compared to that in NPG surface (**Figure 3.21**). This type of close packing of protein molecules may sterically block the active sites, hindering their functional properties. We have found that when NPG on gold wire was dipped in 1 mg mL^{-1} BSA solution, surface coverage of BSA molecule was high. Therefore, as a next step, we tried to study how the concentration of proteins affects the surface coverage. For that, we dipped NPG on gold wire in $10\times$ and $100\times$ diluted BSA solution i.e. 0.1 mg mL^{-1} and 0.01 mg mL^{-1} . **Figure 3.22** shows SEM images of NPG at the above-mentioned concentrations. The surface coverage doesn't look much different for 1 mg mL^{-1} and 0.1 mg mL^{-1} , however, proteins immobilized from 0.01 mg mL^{-1} solution show lower surface coverage. It can be inferred from the data that very high concentration of protein solution may not be ideal for immobilizing protein in NPG as the protein might clog the pores, hindering access of protein molecules to the internal parts of the NPG.

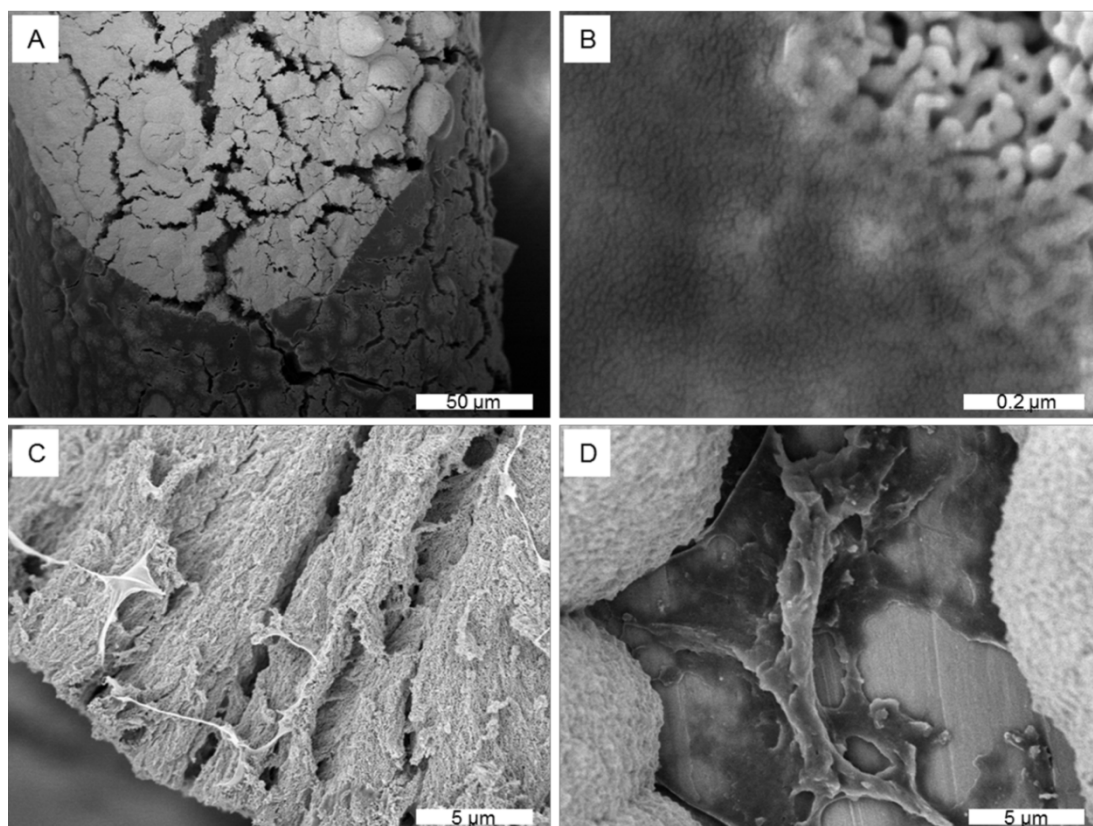


Figure 3.20 SEM micrograph of NPG wire half dipped in 1 mg mL^{-1} BSA solution for 5 min (A) color contrast showing no protein immobilized (bright) and physically immobilized BSA (dark). (B) High-magnification SEM image near the boundary of protein immobilized and non-immobilized region. (C) and (D) are low-magnification images of cross-section and top view of protein immobilized region showing BSA layers.

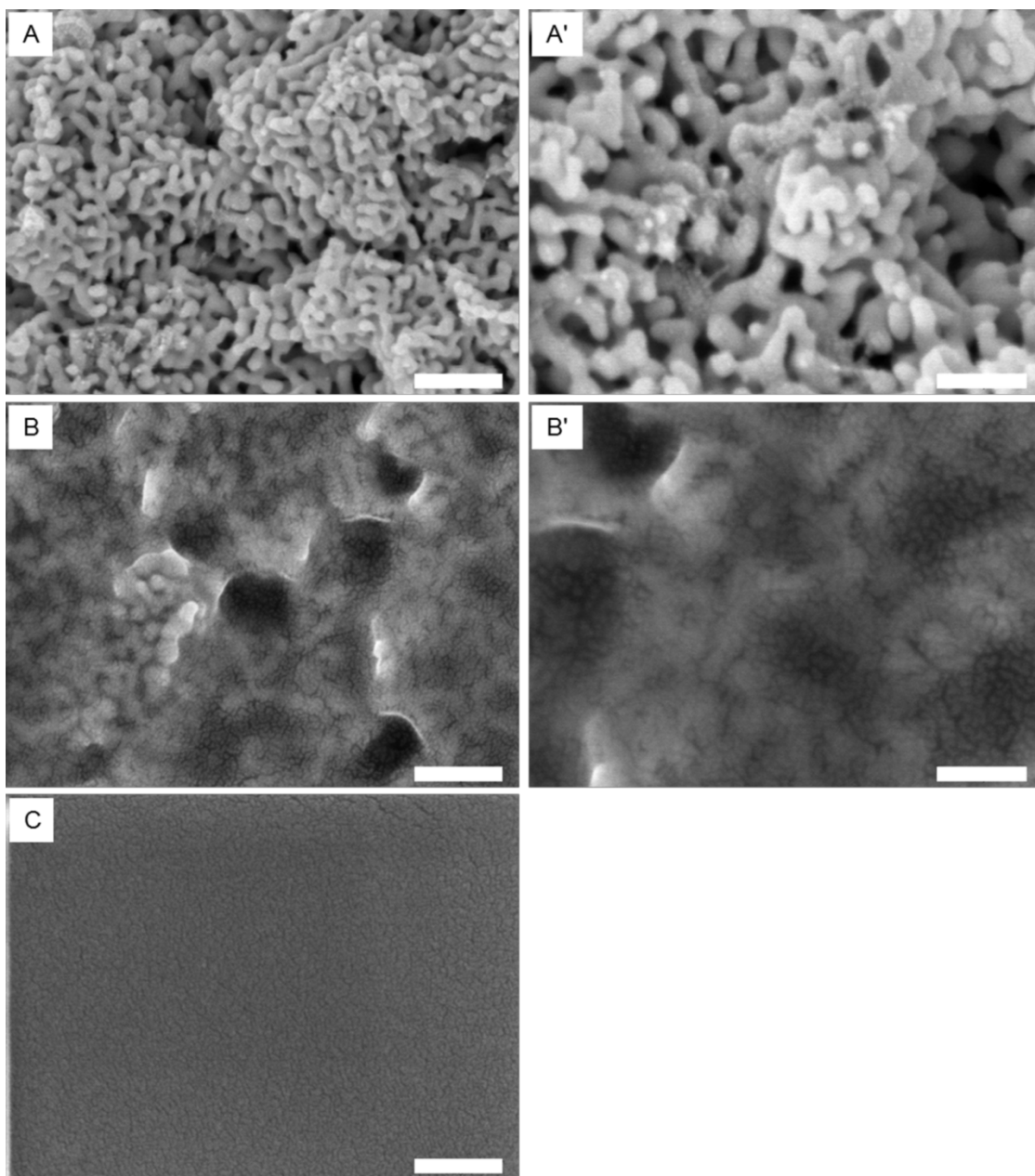


Figure 3.21 High-magnification SEM images of (A) NPG not dipped in protein solution and (B) and (C) NPG and flat gold wire, respectively, dipped in 1 mg mL^{-1} BSA solution. Scale bar: 200 nm. (A') and (B') are SEM images corresponding to (A) and (B) with scale bar 100 nm. Image with scale bar of 100 nm with better resolution cannot be obtained for BSA on flat gold.

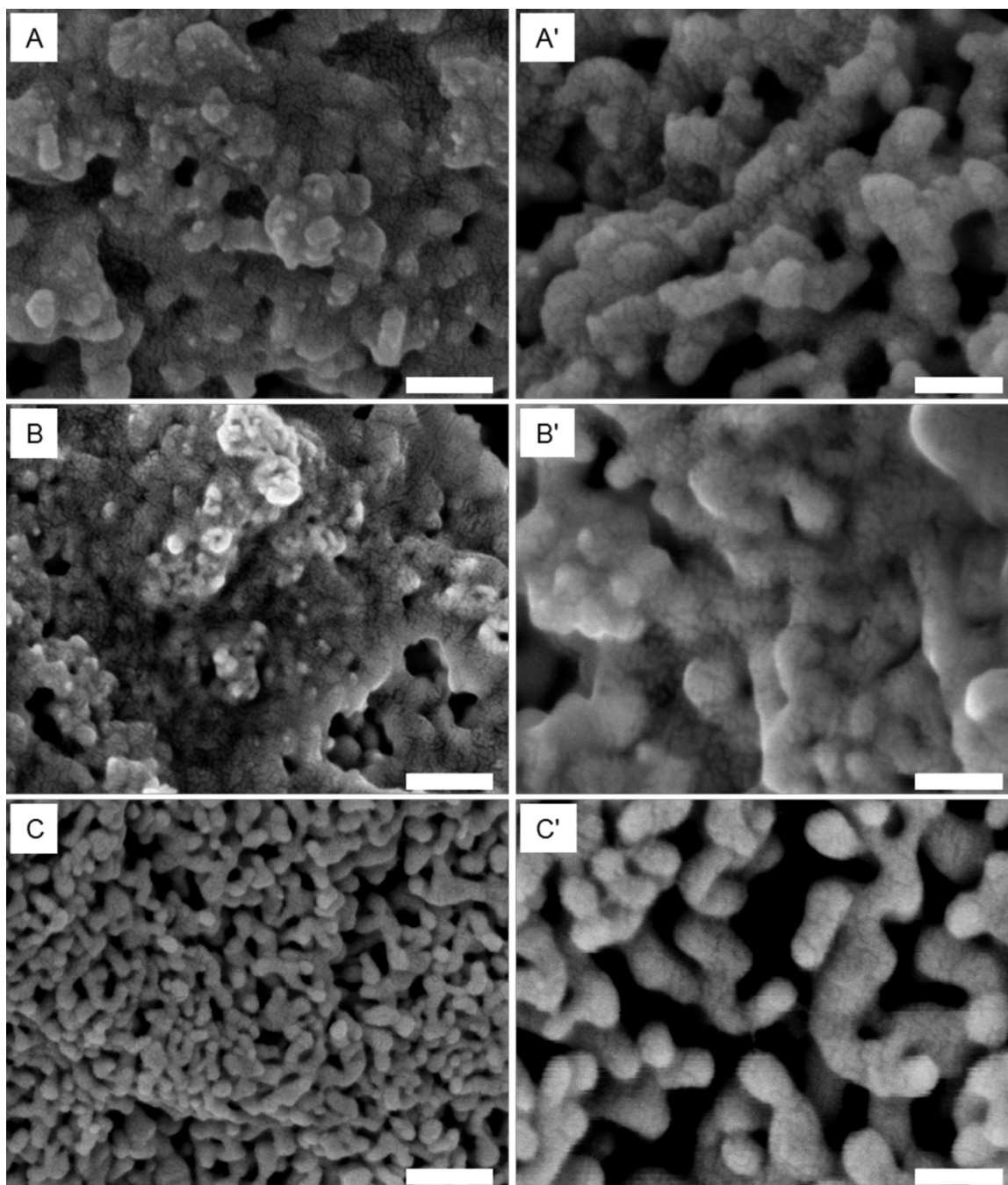


Figure 3.22 SEM images of NPG after immobilization of different concentration of BSA on surface for 5 min (A) 1 mg mL^{-1} (B) 0.1 mg mL^{-1} , and (C) 0.01 mg mL^{-1} . Scale bar: 200 nm. (A'), (B') and (C') are the corresponding images of (A), (B) and (C) with scale bar: 100 nm.

3.2.4.2 Optical biosensing using localized surface plasmon resonance

Since the NPG film prepared from alloy deposited at -1.2 V deposition followed by dealloying at $+1.0$ V shows higher bulk refractive index sensitivity, it was chosen for the biosensing experiments. The initial LSPR spectra of four different NPG films prepared from the same solution bath is shown in **Figure 3.23A**. It can be observed that all the spectra have same peak wavelength at around 469 nm. However, inverse reflection intensity varies significantly between the samples, and has been reported by other groups showing that even changing beam position within the same sample changes intensity.⁴⁶⁻⁴⁷ Therefore, in intensity-based biosensing, the same sample should be used throughout the experiment to obtain comparable data. For wavelength-based biosensing on the other hand, either the same sample or different samples, if required, can be used to compare the data owing to the reproducibility of the peak wavelength position. **Figure 3.23B** shows a label-free sensing of bovine serum albumin (BSA) on an NPG surface modified with lipoic acid (LPA) SAMs whose terminal $-\text{COOH}$ group was activated using EDC/NHS coupling. The initial LSPR peak wavelength of NPG was found at 469 nm which red shift to 475 nm on immobilizing the LPA for 2 h. The $-\text{COOH}$ group of LPA was activated using EDC/NHS coupling reaction for 10 min and on passing BSA solution through the activated LPA SAM, the final peak wavelength was found at 500 nm, confirming the immobilization of BSA. These data show that, NPG surface is sensitive enough to detect the small SAM to bigger protein molecules, using localized surface plasmon resonance spectroscopy.

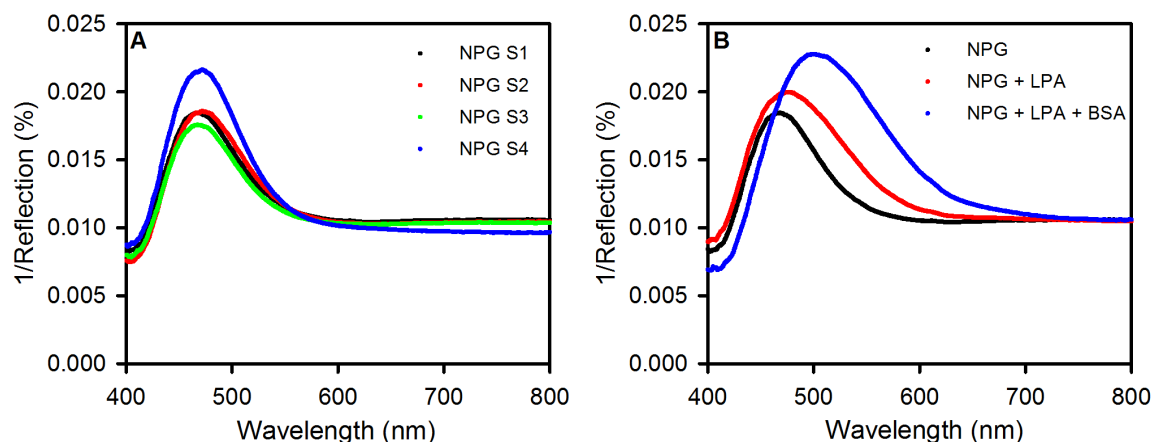


Figure 3.23 (A) Comparison of initial LSPR peak positions of different NPG samples prepared under the same conditions from the same solution bath. (B) LSPR spectra of LPA functionalized NPG (red) and after interaction with BSA (blue) clearly showing red shift in peak wavelength and increase in intensity of 1/reflection.

3.2.4.3 Electrochemical bioassay using square wave voltammetry

Electrochemical assays are attractive for researchers as they are not affected by the turbidity of the solution or background absorbance, involve relatively simple instrumentation, and potentially can be miniaturized.⁴⁸ Square wave voltammetry (SWV) is one of the preferred electrochemical techniques for detection of low concentration of the sample, as this technique minimizes the non-Faradaic current due to electric double layer charging which tends to increase with an increase in surface area of the electrode.³ Here, we used SWV to explore the possibilities for developing enzyme-linked lectinsorbent assays (ELLA) on an NPG wire. We report the application of an NPG wire for development of electrochemical ELLA, in both kinetic and competitive formats, using SWV. **Figure 3.24** summarizes the essential aspects of the electrode modifications used for lectin–enzyme glycoprotein immobilization.

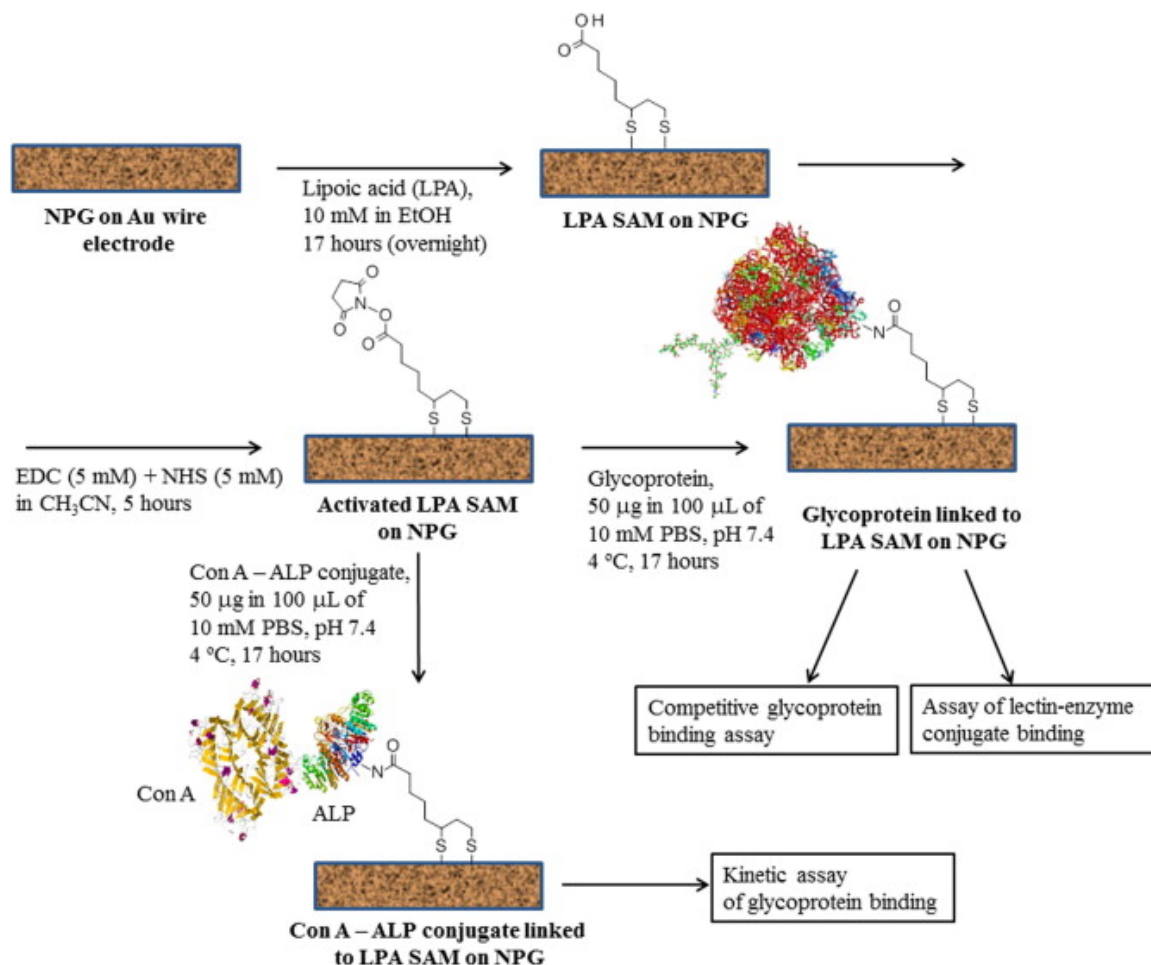


Figure 3.24 The schematic diagram of the electrode modification steps used to perform bioassays on an NPG wire. The NPG was first modified with LPA SAMs onto which either glycoprotein or lectin–enzyme conjugate was immobilized, and finally different types of assays were performed.

A wide variety of biologically significant glycoproteins, which are studied as biomarkers for various diseases, were selected for this study. The proteins included for the experiments are transferrin (TSF), immunoglobulin G (IgG), fetuin (FET), asialofetuin (ASF), carcinoembryonic antigen (CEA), and prostate specific antigen (PSA).

Square wave voltammetry (SWV) assay on gold wire versus NPG-coated gold wire.

We have performed a comparative study between gold wire and NPG-coated gold wire for the potential application in electrochemical ELLA using SWV. For this, LPA SAMs were first prepared on both surfaces, followed by activating the terminal –COOH group using EDC/NHS chemistry, and then immobilization of the Con A–ALP conjugate. SWV studies were performed by incubating these modified electrodes in 1 mM p-APP in glycine buffer (pH 9.0, 100 mM) for 2 min prior to recording the SWV sweep. **Figure 3.25** shows the square wave voltammograms of the Con A–ALP conjugate modified electrodes. When the modified electrodes were incubated in 1 mM p-APP, the gold wire shows no significant peak current, whereas a significant peak current was observed for the modified NPG-coated gold wire electrode. This observation shows the increased sensitivity of the higher surface area NPG-coated gold wire electrode compared to that of the gold wire electrode alone for use in an electrochemical assay using the immobilized enzyme–lectin conjugate. The SAMs of LPA allows easy immobilization of the conjugate onto the NPG surface, and forms a relatively disordered SAM with a significant presence of defects.⁴⁵ These defects provide sites for the electrooxidation of the p-aminophenol generated after the enzymatic reaction of alkaline phosphatase and p-APP substrate.

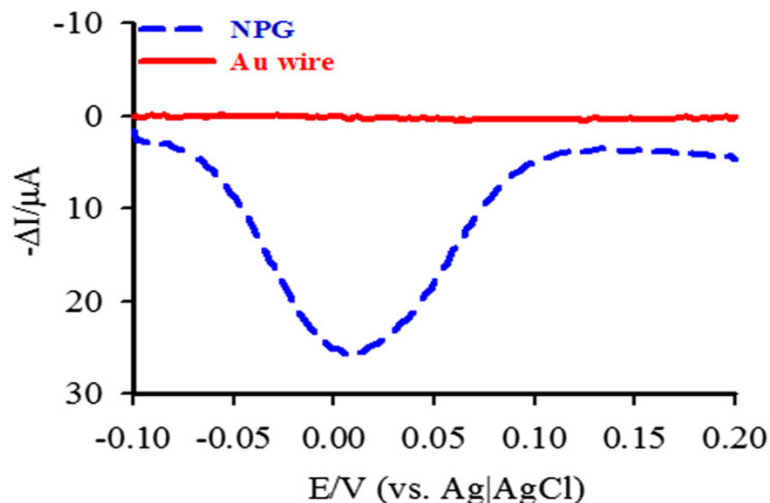


Figure 3.25 Square-wave voltammograms of Con A–ALP conjugate immobilized on gold wire and NPG using LPA SAMs. SWV were recorded with 1 mM p-APP in glycine buffer (pH 9.0, 100 mM) after 2 min incubation with the substrate p-APP.

Effects of SAMs on SWV assay.

We have studied several other SAMs for possible application for better protein immobilization and assay development. **Figure 3.26** shows square wave voltammogram of Con A–ALP conjugate immobilized onto different SAMs on NPG. SAMs of mercaptododecanoic acid (MDDA), MDDA and mercaptooctanol (HS-C₈-OH), and MDDA and 3,6-dioxa-8-mercaptooctanol (HS-(CH₂CH₂O)₂-CH₂CH₂OH) were studied.

Sweeps in the absence of p-APP are generally featureless but may show different background current. Among the SAMs studied, the LPA resulted in higher peak current due to oxidation of p-aminophenol to p-quinoneimine. The smaller peak currents observed for other SAMs are due to difficulty for p-aminophenol molecule to access the NPG surface to undergo electrooxidation. The SWV background current is also larger for the less ordered LPA SAM, possibly due to its higher monolayer capacitance than for the

better-ordered MDDA containing SAMs. LPA was thus chosen as a suitable molecule for SAM formation, as it allows for both protein immobilization and electrochemical detection of the enzyme product.

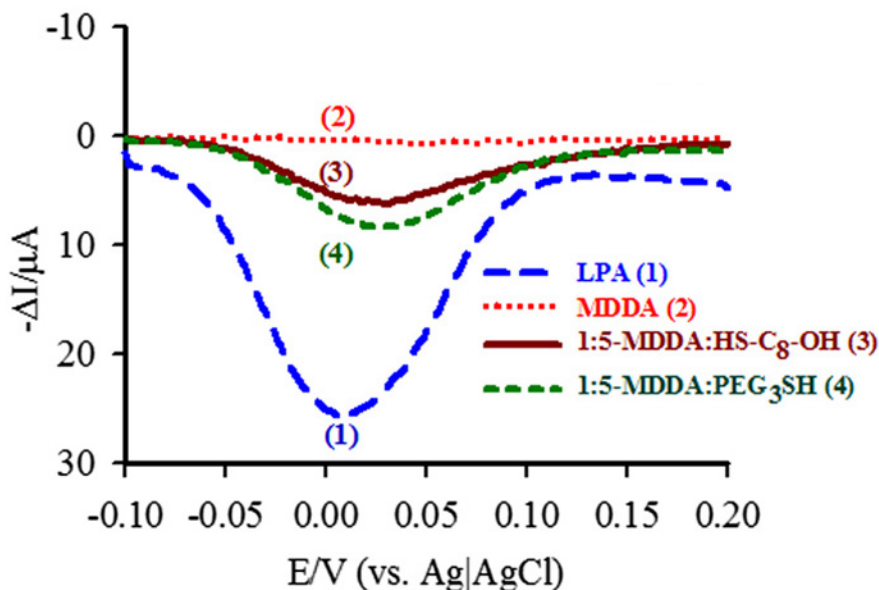


Figure 3.26 Square wave voltammogram of NPG wire after immobilizing Con A-ALP conjugates using different SAMs (1) LPA, (2) MDDA, (3) a 1:5 mixed SAM of MDDA and mercaptooctanol (HO-C8-SH), and (4) a 1:5 mixed SAM of MDDA and 3,6-dioxa-8-mercaptooctanol (PEG3-SH).

Surface coverage of different proteins on LPA SAM.

Total amount of protein immobilized on the NPG surface modified with LPA was determined by depletion method using the BCA assay. A calibration plot was obtained using known concentrations of Con A, and the amount of protein immobilized on NPG surface was determined from the difference in amount of protein initially present in solution and remaining in solution after immobilization onto the NPG surface. The surface coverage of LPA on the NPG electrodes was estimated by reductive desorption of

the SAMs in 0.5 M NaOH solution. The surface coverage for alkanethiol SAMs on flat gold surfaces has been reported to be $7.6 \times 10^{-10} \text{ mol cm}^{-2}$ and for LPA it is $7.1 \times 10^{-10} \text{ mol cm}^{-2}$, which is equivalent to $3.5 \times 10^{-10} \text{ mol cm}^{-2}$ of LPA molecules, assuming two thiol groups per LPA molecule. This indicated that the surface coverage of LPA on NPG surface is approximately 70% and is thus less than a monolayer. It is also possible that for some of the LPA molecules only one Au-thiolate bond has been formed.

The proteins (Con A–ALP conjugate, transferrin, IgG and CEA) were incubated on NPG-coated gold wires modified with a LPA SAM whose terminal –COOH group was activated by EDC/NHS chemistry for 17 h at 4 °C. The amount of protein remaining in the incubation solution was then determined. The difference between the amount of protein initially present in solution and the final amount left in solution gave the estimated amount of protein immobilized onto the NPG wires. **Table 3.4** represents the amounts of these proteins immobilized on an NPG wire as determined from the BCA assay. Given that the surface coverage of LPA is equivalent to $2.42 \times 10^{-10} \text{ mol cm}^{-2}$ and that of Con A–ALP conjugate, transferrin, IgG, CEA, and PSA are 4.6×10^{-13} , 7.1×10^{-13} , 4.7×10^{-13} , 3.0×10^{-13} , and $9.7 \times 10^{-13} \text{ mol cm}^{-2}$, respectively, one protein is estimated to be attached to approximately 280–800 LPA molecules. This shows that the conjugation of protein to the surface is dependent upon the type of protein, although association is most probably by bonding to the most easily accessible lysine residues. Transferrin is immobilized in larger amount compared to IgG and Con A–ALP conjugate. It is evident from the data that small fractions of the LPA molecules are conjugated to the much larger proteins. The area occupied by these proteins is subject to variability

considering that they can occupy a range of orientations. Hence, any estimate of fractional surface coverage is approximate in the absence of orientation information.

Table 3.4 Surface coverage of proteins on NPG.

Proteins	Coverage ($\mu\text{g cm}^2$) ^a	Molar mass (kDa)	Mol cm^{-2}	Molecules cm^{-2}
Con A-ALP	0.080	104 + 69 ^b	4.6×10^{-13}	2.8×10^{-11}
TSF	0.057	80	7.1×10^{-13}	4.3×10^{-11}
IgG	0.075	160	4.7×10^{-13}	2.6×10^{-11}
CEA	0.054	180	3.0×10^{-13}	1.0×10^{-11}

a. Surface coverage was determined by the BCA assay based on the solution depletion studies. Amount of protein left in the incubation solution was subtracted from the amount initially present in the solution to obtain amount immobilized on the NPG surface, wt. represent protein immobilized in 10 NPG wires.

b. Calculation is based on the assumption of one ALP per Con A molecule.

Michaelis–Menten kinetics of the Con A–ALP conjugates on NPG.

The activity of the Con A–alkaline phosphatase conjugate on the LPA SAM modified NPG was measured to further study the suitability of the surface for conjugate immobilization. We studied the ALP kinetic behavior on the NPG surface by dipping the electrode in 0.01–1.0 mM p-APP solutions for 2 min. SWV peak current was found to be increasing linearly with the increase in substrate concentration, finally reaching a plateau, consistent with Michaelis–Menten kinetic behavior (**Figure 3.27**). The peak current of the SWV measurement is related to the initial reaction rate and hence to the reaction kinetics. The K_m value was determined by fitting the data to the Michaelis–Menten equation, and was found to be 200 μM . This value was of interest because most enzyme electrodes are operated near K_m values.⁴⁹ The SWV sweeps resulted in a prominent peak for the oxidation of p-aminophenol in this concentration range. The oxidation of p-AP to p-quinoneimine occurs near a potential 0.0 V (vs. Ag/AgCl) on NPG. The surfaces of NPG are found more electroactive than relatively smooth gold surfaces because of defects, curvature, and roughness of the surface. The lower oxidation potential observed for p-AP in this study compared to the oxidation potential of p-AP on relatively flat gold surfaces reported before might be because of nanostructures of NPG.⁵⁰

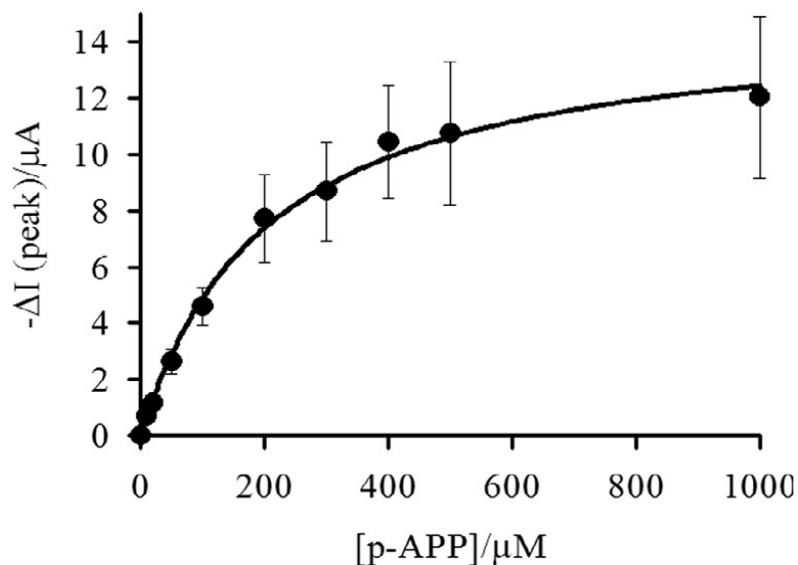


Figure 3.27 Peak current vs. p-APP concentrations of the Con A–ALP conjugate immobilized on LPA fitted to the Michaelis–Menten equation.

Enzyme-linked lectinsorbent assay on NPG.

The kinetics of enzyme-linked lectinsorbent assays are based on the difference in the rate of enzymatic reaction of ALP conjugated to Con A, before and after glycoprotein binding to the Con A. Thus, we chose a substrate concentration 200 μM for the kinetic assay, a concentration that falls in the pseudo-linear range. The presence of a large glycoprotein molecule bound to the lectin close to the ALP causes steric hindrance for the access of the p-APP substrate to the active site of ALP. The binding of the glycoprotein will reduce the initial rate of enzymatic conversion of p-APP to the oxidizable p-aminophenol product. The enzyme reaction rate was assumed proportional to the peak current of the square wave voltammogram. The difference in SWV peak current before and after incubation is the response variable for the assay. The concentration of p-APP of 200 μM is close to the K_m value and p-APP concentrations less than 100 μM did not produce current peaks of sufficient magnitude in the SWV scans. For the kinetic assay,

the incubation time of proteins is important, so a study was performed by varying the incubation time with the glycoprotein and the conjugate immobilized NPG. Saturation of the peak current was reached within 1 h and thus 2 h was chosen for the incubation time to be sure peak current saturation was reached. Enzyme kinetics and hence the rate of conversion of substrate to product depends on the access of the substrate to the active site of the enzyme. When relatively large and bulky molecules bind to the lectin conjugated to the enzyme, access of the substrate to the active site is hindered and results in a decrease in activity and hence a decrease in initial velocity of the reaction.⁵¹

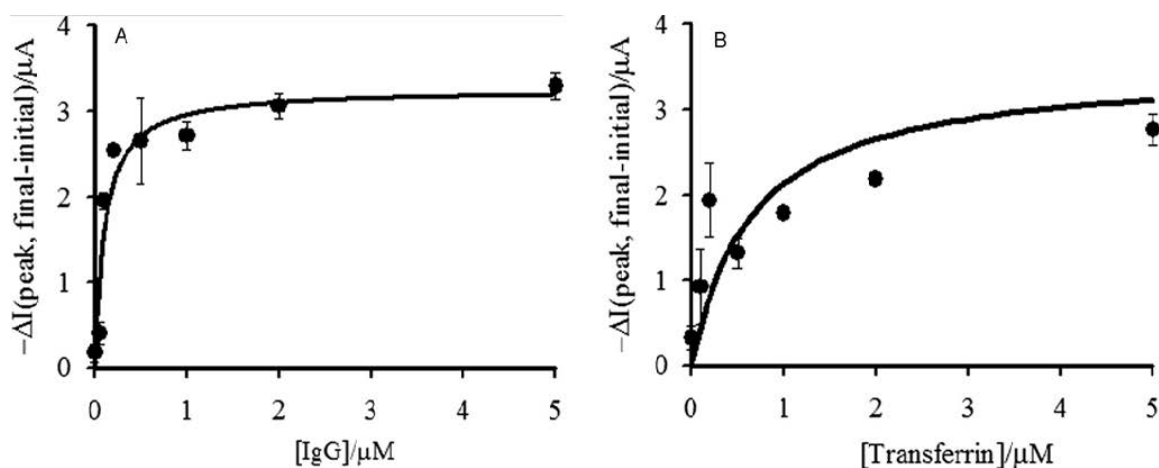


Figure 3.28 Kinetic ELLA response on NPG. Different concentrations of (A) IgG and (B) transferrin were incubated for 2 h in PBS (pH 7.4) with Con A-ALP conjugate immobilized on LPA modified NPG and the difference in peak current before and after incubation was plotted to obtain the response plot.

When glycoprotein binds to Con A–ALP conjugate, access of the p-APP to the enzyme active site is hindered and results in a decrease in the reaction velocity. **Figure 3.28A,B** shows the binding isotherms determined for the binding of IgG and transferrin, respectively, to the immobilized Con A–ALP conjugate. As expected, there is decrease in enzymatic activity with an increase in concentration of glycoprotein, which is observed in terms of the increased difference in peak current. The binding affinity of Con A to IgG was found to be $K_d = 105$ nM, and that of Con A to transferrin was found to be $K_d = 650$ nM.

The binding affinity of Con A to glycoprotein depends upon the glycan structure and multivalent interactions. Binding affinity of Con A to multivalent mannose units has found to be higher compared to similar monovalent units in the glycoconjugates.⁵² Thus, the overall affinity of a glycoprotein–lectin interaction depends on the mannose linkage, whether it is biantennary or triantennary, as well as the numbers and spacing of terminal mannose units, which can possibly lead to multivalent binding, increasing the affinity. Two other proteins asialofetuin and fetuin were also studied for the kinetic assay but these proteins did not produce any significant change in the peak current. This we believe is because of the relatively lower binding affinity and especially the smaller sizes of these proteins (45–55 kDa) compared to IgG (≈ 160 kDa) or transferrin (≈ 80 kDa). The kinetic assay described based on lectin–enzyme conjugates is thus expected to be more responsive for large-size glycoproteins. Based on the average of the standard deviations (σ) for the determinations at each protein concentration, a detection limit based on $3 \times \sigma$ would be a difference of 0.50 on the y-axis for the IgG data representing a detection limit of 0.02 μ M. A similar consideration for the transferrin data ($3 \times \sigma = 0.63$) gives a

detection limit of 0.14 μM . The response in each case is non-linear, with the range over which transferrin can be detected before the response approaches saturation being wider ($\approx 3\text{--}4\ \mu\text{M}$) than that over which IgG can be detected ($\approx 1\ \mu\text{M}$). The level of transferrin in human serum typically falls between $2\text{--}3\ \text{g L}^{-1}$ ($2.5\text{--}3.8\ \mu\text{M}$).⁵³ Thus, detection of variant glycoforms of transferrin of lower concentration seems at least worth considering using electrochemical ELLA provided the transferrin fraction can be isolated and comparison with other methods such as mass spectrometry made.

SWV detection of lectin–enzyme conjugate binding to immobilized glycoproteins.

The glycoproteins transferrin (TSF), immunoglobulin G (IgG), fetuin (FET), asialofetuin (ASF), carcinoembryonic antigen (CEA), and prostate specific antigen (PSA) were covalently immobilized onto the LPA SAMs on the NPG surface by EDC/NHS coupling. Bovine serum albumin (BSA) and LPA modified NPG were used as negative controls. These protein-modified wires after incubation with the Con A–ALP conjugate were incubated in p-APP and then SWV was performed. **Figure 3.29** shows a bar plot of peak current of the SWVs for the different glycoproteins. The maximum peak currents from Con A–ALP was obtained for TSF, IgG, CEA, and PSA, because of presence of large number of mannose unit within these glycoprotein, and the smallest peak currents were observed with fetuin and asialofetuin. On the other hand, BSA and the un-activated LPA SAM showed very small peak currents. The very small response from the LPA SAM indicates that the Con A–ALP conjugate does not strongly adsorb non-specifically on this surface. Significant amount of peak currents were observed with the bare NPG incubated with the Con A–ALP conjugate due to the non-specific adsorption of protein on the gold surface. A thiolated α -mannoside modified NPG was also used for the study

but an almost negligible signal was obtained using either the pure thiolated α -mannoside or 1:5 mixed SAM of the thiolated α -mannoside and 3,6-dioxa-8-mercaptooctanol. This could be because of the oxidation of the p-AP product was significantly blocked by the SAMs. It is hypothesized based on these results that an NPG array format with use of a larger number of lectin-ALP conjugates each responding differently to an immobilized glycoprotein could be used as a method of electrochemical profiling of glycosylation.

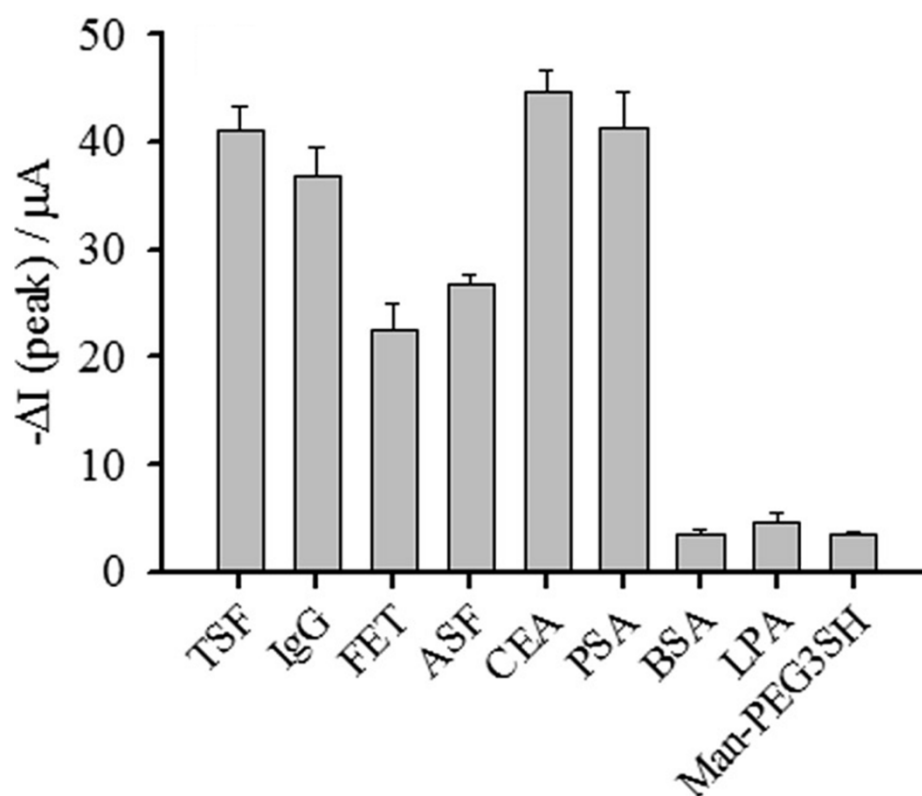


Figure 3.29 Bar plot for SWV response due to Con A-ALP conjugate binding to different glycoproteins on NPG. Glycoproteins were immobilized on NPG and incubated with $50 \mu\text{g mL}^{-1}$ conjugate for 24 h and then incubated with 1 mM p-APP for 2 min.

3.2.4.4 Glucose oxidation

Oxidation of glucose has been examined extensively for the development of better blood glucose sensors and biological fuel cells.⁵⁴ The most commonly used oxidation methods include microbe-assisted oxidation, enzyme-assisted oxidation, and direct oxidation at the electrode surface.⁵⁵ Glucose oxidase (GOx)-based glucose sensing is the most commonly used technique, since the discovery of glucose biosensor in 1962 by Clark and Lyons.⁵⁶⁻⁵⁷ However, the main challenges for the enzyme-based glucose sensors are long-term stability of the enzyme and reagents used,⁵⁸ and regeneration of the strips. To overcome these problems research has been performed where glucose can be electrochemically oxidized without the need of enzymes.^{55, 59} Here, we show the similar direct glucose oxidation technique using nanoporous gold wire (NPG) as an electrode and report the advantages of NPG electrode over the flat gold wire (FGW) electrode and previously reported nanostructured electrode in literatures.

Figure 3.30 represents cyclic voltammograms of FGW and NPG in 0.1 M NaOH solution (black) and 5 mM glucose in 0.1M M NaOH solution. In the absence of glucose, during the anodic scan, gold oxide layer start forming on the gold surface at nearly 0.2 V evident by the increase in anodic current in both FGW and NPG. On the negative scan back, we can see increase in cathodic current starting at nearly 0.2 V proving the removal of the oxide layer. In the presence of glucose, during the anodic scan an anodic peak current has been found at around -0.5 V, $+0.2$, and $+0.4$ for FGW. The first peak current at -0.5 V is because of oxidation of glucose to gluconolactone (two-electron oxidation product) and the second peak current at $+0.2$ V is because of subsequent oxidation of gluconolactone to oxalate (18-electron oxidation product). The third peak current at

nearly +0.4 is because of gold oxide layer formation. It should be noted that second oxidation and oxide layer formation process overlap near + 0.2 V. Therefore, the peak obtained for the second oxidation is not only because of oxidation of gluconolactone but also in part because of oxide layer formation. In NPG, during glucose oxidation, similar two oxidation peaks are observed at nearly -0.7 V and -0.2 V (**Figure 3.31**) which is negatively shifted by 0.2 V for the first oxidation and 0.4 V for the second oxidation. Interestingly, in NPG this shift also separates the second oxidation peak from the peak due to oxide layer formation. When scan is limited to 0.2 V, we have found no oxide removal peak, shown by green curve in **Figure 3.30** and **3.31**.

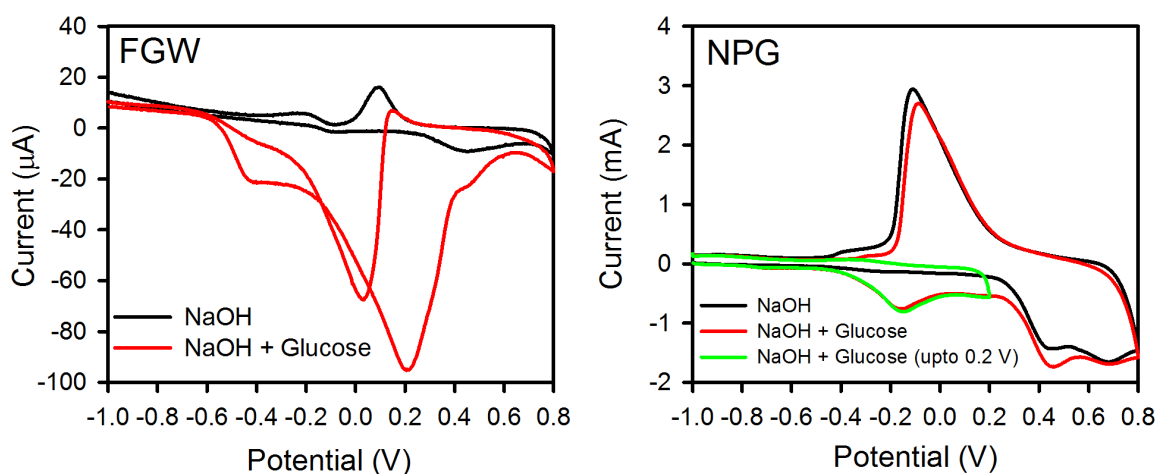


Figure 3.30 CV of FGW and NPG in 0.1 M NaOH solution (black) and 5 mM glucose in 0.1M NaOH solution (red). Green CV of NPG represents scanning up to 0.2 V in 5 mM glucose in 0.1M M NaOH solution. Scan rate: 100 mV s^{-1} .

Figure 3.32 shows the cyclic voltammetry of FGW and NPG on glucose oxidation at multiple scans. It can be seen that FGW electrodes does not give stable cv and keep changing with addition of each scan until seven cycles are reached. In contrast, in NPG the second scan is good enough to get a stable voltammogram. Separating the

second oxidation peak from the oxide layer formation peak and providing the stable voltammogram make NPG the optimal substrate for the oxidation of glucose, however, its efficacy in a real sample is still to explore.

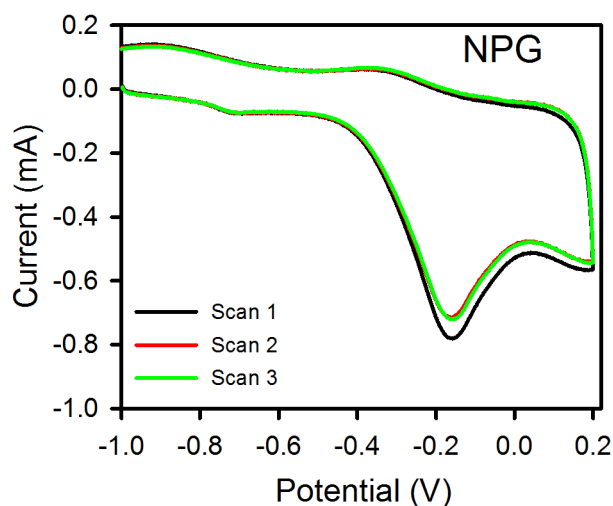


Figure 3.31 CV of NPG when scanned up to 0.2 V in 5 mM glucose in 0.1M M NaOH solution at three subsequent scans. Scan rate: 100 mV s^{-1} .

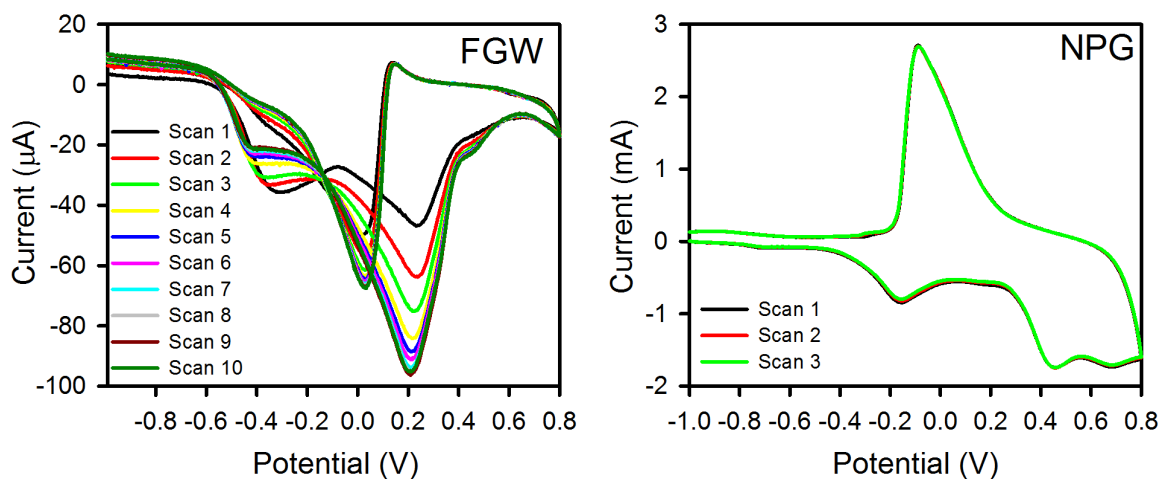


Figure 3.32 CV of FGW and NPG in 5 mM glucose in 0.1M NaOH solution under multiscan (number of scans indicated). Scan rate: 100 mV s^{-1} .

3.3 Conclusions

We have prepared nanoporous gold on gold wire and flat gold under varieties of conditions and characterized them to get most stable structure with high surface area structures. We were able to prepare nanoporous gold electrochemically under neutral pH at room temperature with controlled pore size. We were also successful in tuning the pores (gaps) and ligament size of nanoporous gold by post-treating NPG in different solvents with applying oxidation-reduction cycles. The resulting structures formed have around twice the pores (gaps) of NPG with decrease in surface area by nearly 24%. The interligament gaps and ligament width were also found different in size, unlike the structures formed by other annealing techniques. Finally, NPG structures were used for various applications, such as protein immobilization, localized surface plasmon resonance-based sensing of proteins and their interactions with carbohydrates, SWV-based bioassay of carbohydrates–proteins interactions, and glucose oxidation.

3.4 References

1. Stine, K. J.; Jefferson, K.; Shulga, O. V., Nanoporous Gold for Enzyme Immobilization. In *Enzyme Stabilization and Immobilization*, Springer: 2011; pp 67-83.
2. Hodge, A. M.; Hayes, J. R.; Caro, J. A.; Biener, J.; Hamza, A. V., Characterization and Mechanical Behavior of Nanoporous Gold. *Adv. Eng. Mater.* **2006**, 8 (9), 853-857.
3. Collinson, M. M., Nanoporous Gold Electrodes and Their Applications in Analytical Chemistry. *Int. Sch. Res. Not.* **2013**, 2013.
4. Shulga, O. V.; Jefferson, K.; Khan, A. R.; D'Souza, V. T.; Liu, J.; Demchenko, A. V.; Stine, K. J., Preparation and Characterization of Porous Gold and Its Application as a Platform for Immobilization of Acetylcholine Esterase. *Chem. Mater.* **2007**, 19 (16), 3902-3911.
5. Wittstock, A.; Zielasek, V.; Biener, J.; Friend, C. M.; Bäumer, M., Nanoporous Gold Catalysts for Selective Gas-Phase Oxidative Coupling of Methanol at Low Temperature. *Science* **2010**, 327 (5963), 319-322.
6. Xu, C.; Su, J.; Xu, X.; Liu, P.; Zhao, H.; Tian, F.; Ding, Y., Low Temperature Co Oxidation over Unsupported Nanoporous Gold. *J. Am. Chem. Soc.* **2007**, 129 (1), 42-43.
7. Zeis, R.; Lei, T.; Sieradzki, K.; Snyder, J.; Erlebacher, J., Catalytic Reduction of Oxygen and Hydrogen Peroxide by Nanoporous Gold. *J. Catal.* **2008**, 253 (1), 132-138.
8. Yin, H.; Zhou, C.; Xu, C.; Liu, P.; Xu, X.; Ding, Y., Aerobic Oxidation of D-Glucose on Support-Free Nanoporous Gold. *J. Phys. Chem. C* **2008**, 112 (26), 9673-9678.
9. Asao, N.; Ishikawa, Y.; Hatakeyama, N.; Yamamoto, Y.; Chen, M.; Zhang, W.; Inoue, A., Nanostructured Materials as Catalysts: Nanoporous-Gold-Catalyzed Oxidation of Organosilanes with Water. *Angew. Chem. Int. Ed.* **2010**, 49 (52), 10093-10095.
10. Biener, J.; Wittstock, A.; Zepeda-Ruiz, L. A.; Biener, M. M.; Zielasek, V.; Kramer, D.; Viswanath, R. N.; Weissmuller, J.; Baumer, M.; Hamza, A. V., Surface-Chemistry-Driven Actuation in Nanoporous Gold. *Nat Mater* **2009**, 8 (1), 47-51.
11. Qiu, H.; Xu, C.; Huang, X.; Ding, Y.; Qu, Y.; Gao, P., Immobilization of Laccase on Nanoporous Gold: Comparative Studies on the Immobilization Strategies and the Particle Size Effects. *J. Phys. Chem. C* **2009**, 113 (6), 2521-2525.
12. Liu, Z.; Du, J.; Qiu, C.; Huang, L.; Ma, H.; Shen, D.; Ding, Y., Electrochemical Sensor for Detection of P-Nitrophenol Based on Nanoporous Gold. *Electrochem. Commun.* **2009**, 11 (7), 1365-1368.
13. Shulga, O. V.; Zhou, D.; Demchenko, A. V.; Stine, K. J., Detection of Free Prostate Specific Antigen (Fpsa) on a Nanoporous Gold Platform. *Analyst* **2008**, 133 (3), 319-322.
14. Hu, K.; Lan, D.; Li, X.; Zhang, S., Electrochemical DNA Biosensor Based on Nanoporous Gold Electrode and Multifunctional Encoded DNA-Au Bio Bar Codes. *Anal. Chem.* **2008**, 80 (23), 9124-9130.
15. Ahl, S.; Cameron, P. J.; Liu, J.; Knoll, W.; Erlebacher, J.; Yu, F., A Comparative Plasmonic Study of Nanoporous and Evaporated Gold Films. *Plasmonics* **2008**, 3 (1), 13-20.

16. Qian, L. H.; Yan, X. Q.; Fujita, T.; Inoue, A.; Chen, M. W., Surface Enhanced Raman Scattering of Nanoporous Gold: Smaller Pore Sizes Stronger Enhancements. *Appl. Phys. Lett.* **2007**, *90* (15), 153120-153120-3.
17. Chen, H.-A.; Long, J.-L.; Lin, Y.-H.; Weng, C.-J.; Lin, H.-N., Plasmonic Properties of a Nanoporous Gold Film Investigated by Far-Field and near-Field Optical Techniques. *J. Appl. Phys.* **2011**, *110* (5), 054302.
18. Dursun, A.; Pugh, D. V.; Corcoran, S. G., Probing the Dealloying Critical Potential. *J. Electrochem. Soc.* **2005**, *152* (2), B65-B72.
19. Erlebacher, J.; Aziz, M. J.; Karma, A.; Dimitrov, N.; Sieradzki, K., Evolution of Nanoporosity in Dealloying. *Nature* **2001**, *410* (6827), 450-3.
20. Kameoka, S.; An Pang, T., Co Oxidation over a Fine Porous Gold Catalyst Fabricated by Selective Leaching from an Ordered AuCu₃ Intermetallic Compound. *Catal. Lett.* **2008**, *121* (3/4), 337-341.
21. Huang, J. F.; Sun, I. W., Fabrication and Surface Functionalization of Nanoporous Gold by Electrochemical Alloying/Dealloying of Au–Zn in an Ionic Liquid, and the Self-Assembly of L-Cysteine Monolayers. *Adv. Funct. Mater.* **2005**, *15* (6), 989-994.
22. Zhang, Z.; Wang, Y.; Qi, Z.; Lin, J.; Bian, X., Nanoporous Gold Ribbons with Bimodal Channel Size Distributions by Chemical Dealloying of Al– Au Alloys. *J. Phys. Chem. C* **2009**, *113* (4), 1308-1314.
23. Ding, Y.; Kim, Y. J.; Erlebacher, J., Nanoporous Gold Leaf: “Ancient Technology”/Advanced Material. *Adv. Mater.* **2004**, *16* (21), 1897-1900.
24. Qian, L. H.; Chen, M. W., Ultrafine Nanoporous Gold by Low-Temperature Dealloying and Kinetics of Nanopore Formation. *Appl. Phys. Lett.* **2007**, *91* (8), 083105-3.
25. Kertis, F.; Snyder, J.; Govada, L.; Khurshid, S.; Chayen, N.; Erlebacher, J., Structure/Processing Relationships in the Fabrication of Nanoporous Gold. *JOM* **2010**, *62* (6), 50-56.
26. Shulga, O. V.; Zhou, D.; Demchenko, A. V.; Stine, K. J., Detection of Free Prostate Specific Antigen (Fpsa) on a Nanoporous Gold Platform. *Analyst* **2008**, *133* (3).
27. Gish, D. A.; Nsiah, F.; McDermott, M. T.; Brett, M. J., Localized Surface Plasmon Resonance Biosensor Using Silver Nanostructures Fabricated by Glancing Angle Deposition. *Anal. Chem.* **2007**, *79* (11), 4228-4232.
28. Seker, E.; Gaskins, J. T.; Bart-Smith, H.; Zhu, J.; Reed, M. L.; Zangari, G.; Kelly, R.; Begley, M. R., The Effects of Post-Fabrication Annealing on the Mechanical Properties of Freestanding Nanoporous Gold Structures. *Acta Mater.* **2007**, *55* (14), 4593-4602.
29. Seker, E.; Reed, M. L.; Begley, M. R., Nanoporous Gold: Fabrication, Characterization, and Applications. *Materials* **2009**, *2* (4), 2188-2215.
30. Alonso, C.; Salvarezza, R. C.; Vara, J. M.; Arvia, A. J., The Surface Diffusion of Gold Atoms on Gold Electrodes in Acid Solution and Its Dependence on the Presence of Foreign Adsorbates. *Electrochim. Acta* **1990**, *35* (9), 1331-1336.
31. Diaz, M. A.; Kelsall, G. H.; Welham, N. J., Electrowinning Coupled to Gold Leaching by Electrogenenerated Chlorine: I. Au(III) → Au(I) / Au Kinetics in Aqueous Cl₂/Cl⁻ Electrolytes. *J. Electroanal. Chem.* **1993**, *361* (1–2), 25-38.

32. Honbo, H.; Sugawara, S.; Itaya, K., Detailed in-Situ Scanning Tunneling Microscopy of Single Crystal Planes of Gold (111) in Aqueous Solutions. *Anal. Chem.* **1990**, 62 (22), 2424-2429.
33. Vogler, A.; Kunkely, H., Photoreactivity of Gold Complexes. *Coord. Chem. Rev.* **2001**, 219, 489-507.
34. Kissinger, P. T.; Heineman, W. R., Cyclic Voltammetry. *J. Chem. Educ.* **1983**, 60 (9), 702.
35. Tan, Y. H.; Schallom, J. R.; Ganesh, N. V.; Fujikawa, K.; Demchenko, A. V.; Stine, K. J., Characterization of Protein Immobilization on Nanoporous Gold Using Atomic Force Microscopy and Scanning Electron Microscopy. *Nanoscale* **2011**, 3 (8), 3395-3407.
36. Hu, K.; Lan, D.; Li, X.; Zhang, S., Electrochemical DNA Biosensor Based on Nanoporous Gold Electrode and Multifunctional Encoded DNA– Au Bio Bar Codes. *Anal. Chem.* **2008**, 80 (23), 9124-9130.
37. Yu, F.; Ahl, S.; Caminade, A.-M.; Majoral, J.-P.; Knoll, W.; Erlebacher, J., Simultaneous Excitation of Propagating and Localized Surface Plasmon Resonance in Nanoporous Gold Membranes. *Anal. Chem.* **2006**, 78 (20), 7346-7350.
38. Lee, Y.; Lee, E. K.; Cho, Y. W.; Matsui, T.; Kang, I. C.; Kim, T. S.; Han, M. H., Proteochip: A Highly Sensitive Protein Microarray Prepared by a Novel Method of Protein Immobilization for Application of Protein-Protein Interaction Studies. *Proteomics* **2003**, 3 (12), 2289-2304.
39. Camarero, J. A.; Kwon, Y.; Coleman, M. A., Chemoselective Attachment of Biologically Active Proteins to Surfaces by Expressed Protein Ligation and Its Application for “Protein Chip” Fabrication. *J. Am. Chem. Soc.* **2004**, 126 (45), 14730-14731.
40. Cretich, M.; Damin, F.; Pirri, G.; Chiari, M., Protein and Peptide Arrays: Recent Trends and New Directions. *Biomol. Eng* **2006**, 23 (2), 77-88.
41. Mateo, C.; Palomo, J. M.; Fernandez-Lorente, G.; Guisan, J. M.; Fernandez-Lafuente, R., Improvement of Enzyme Activity, Stability and Selectivity Via Immobilization Techniques. *Enzyme Microb. Technol.* **2007**, 40 (6), 1451-1463.
42. Patel, N.; Davies, M. C.; Hartshorne, M.; Heaton, R. J.; Roberts, C. J.; Tendler, S. J.; Williams, P. M., Immobilization of Protein Molecules onto Homogeneous and Mixed Carboxylate-Terminated Self-Assembled Monolayers. *Langmuir* **1997**, 13 (24), 6485-6490.
43. Norde, W.; Zoungrana, T., Surface-Induced Changes in the Structure and Activity of Enzymes Physically Immobilized at Solid/Liquid Interfaces. *Biotechnol. Appl. Biochem.* **1998**, 28 (2), 133-143.
44. Rusmini, F.; Zhong, Z.; Feijen, J., Protein Immobilization Strategies for Protein Biochips. *Biomacromolecules* **2007**, 8 (6), 1775-1789.
45. Pandey, B.; Bhattarai, J. K.; Pornsuriyasak, P.; Fujikawa, K.; Catania, R.; Demchenko, A. V.; Stine, K. J., Square-Wave Voltammetry Assays for Glycoproteins on Nanoporous Gold. *J. Electroanal. Chem.* **2014**, 717, 47-60.
46. Jensen, T. R.; Duval, M. L.; Kelly, K. L.; Lazarides, A. A.; Schatz, G. C.; Van Duyne, R. P., Nanosphere Lithography: Effect of the External Dielectric Medium on the Surface Plasmon Resonance Spectrum of a Periodic Array of Silver Nanoparticles. *J. Phys. Chem. B* **1999**, 103 (45), 9846-9853.

47. Marinakos, S. M.; Chen, S.; Chilkoti, A., Plasmonic Detection of a Model Analyte in Serum by a Gold Nanorod Sensor. *Anal. Chem.* **2007**, *79* (14), 5278-5283.
48. Thompson, R. Q.; Barone Iii, G. C.; Halsall, H. B.; Heineman, W. R., Comparison of Methods for Following Alkaline Phosphatase Catalysis: Spectrophotometric Versus Amperometric Detection. *Anal. Biochem.* **1991**, *192* (1), 90-95.
49. Cracknell, J. A.; Vincent, K. A.; Armstrong, F. A., Enzymes as Working or Inspirational Electrocatalysts for Fuel Cells and Electrolysis. *Chem. Rev.* **2008**, *108* (7), 2439-2461.
50. Niwa, O.; Xu, Y.; Halsall, H. B.; Heineman, W. R., Small-Volume Voltammetric Detection of 4-Aminophenol with Interdigitated Array Electrodes and Its Application to Electrochemical Enzyme Immunoassay. *Anal. Chem.* **1993**, *65* (11), 1559-1563.
51. Wolfenden, R., Enzyme Catalysis: Conflicting Requirements of Substrate Access and Transition State Affinity. *Mol. Cell. Biochem.* **1974**, *3* (3), 207-211.
52. Mann, D. A.; Kanai, M.; Maly, D. J.; Kiessling, L. L., Probing Low Affinity and Multivalent Interactions with Surface Plasmon Resonance: Ligands for Concanavalin A. *J. Am. Chem. Soc.* **1998**, *120* (41), 10575-10582.
53. Nemeth, E.; Rivera, S.; Gabayan, V.; Keller, C.; Taudorf, S.; Pedersen, B. K.; Ganz, T., Il-6 Mediates Hypoferremia of Inflammation by Inducing the Synthesis of the Iron Regulatory Hormone Hepcidin. *J. Clin. Invest.* **2004**, *113* (9), 1271-1276.
54. Wang, J., Electrochemical Glucose Biosensors. *Chem. Rev.* **2008**, *108* (2), 814-825.
55. Pasta, M.; Ruffo, R.; Falletta, E.; Mari, C.; Della Pina, C., Alkaline Glucose Oxidation on Nanostructured Gold Electrodes. *Gold Bull.* **2010**, *43* (1), 57-64.
56. Clark, L. C.; Lyons, C., Electrode Systems for Continuous Monitoring in Cardiovascular Surgery. *Ann. N.Y. Acad. Sci.* **1962**, *102* (1), 29-45.
57. Newman, J. D.; Turner, A. P., Home Blood Glucose Biosensors: A Commercial Perspective. *Biosens. Bioelectron.* **2005**, *20* (12), 2435-2453.
58. Jena, B. K.; Raj, C. R., Enzyme-Free Amperometric Sensing of Glucose by Using Gold Nanoparticles. *Chem. Eur. J.* **2006**, *12* (10), 2702-2708.
59. Tominaga, M.; Shimazoe, T.; Nagashima, M.; Kusuda, H.; Kubo, A.; Kuwahara, Y.; Taniguchi, I., Electrocatalytic Oxidation of Glucose at Gold-Silver Alloy, Silver and Gold Nanoparticles in an Alkaline Solution. *J. Electroanal. Chem.* **2006**, *590* (1), 37-46.

CHAPTER 4 FABRICATION OF NANOSTRUCTURED GOLD FILM FOR THE STUDY OF BIOMOLECULAR INTERACTIONS USING LSPR SPECTROSCOPY

4.1 Introduction

Localized surface plasmon resonance (LSPR) spectroscopy is the one of current research fields that is gaining considerable attraction from researchers all around the world.¹⁻⁵ This is because it is a label free sensitive biosensing technique⁶ and bears great potential to be miniaturized.⁷ However, the overall sensitivity of the LSPR spectroscopy depends on transducer used. Nanostructures of the coinage metals copper⁸, silver⁹ and gold¹⁰ are being actively studied as LSPR-based transducers. When nanostructures having dimensions much smaller than the incident wavelength of light interacts with light there will be collective oscillation of the valence electrons locally around the nanostructures called LSPR.¹¹ LSPR depends on the composition, shape, size, and local dielectric properties of the nanostructures opening the broader field of research for fabricating sensitive nanostructures.¹² It has been found that silver shows better LSPR response compared to gold and copper, but it has the issue of oxidation and biocompatibility; whereas, gold is very stable and biocompatible but is expensive.¹³ Nanostructures having different shapes like triangular, sphere, cube, rod etc. produce different peak positions, full width at half maxima and hence different LSPR sensitivity.¹⁴ In general, nanostructures having sharp tips yield higher RI sensitivity.¹⁵ It has also been found that increasing the size of nanoparticles red shifts the resonance peak position and

increases the sensitivity; however, the peak becomes broader decreasing the figure of merit (FOM) due to radiation damping.¹⁶⁻¹⁷

Common techniques for fabricating nanostructured transducer are immobilization of nanoparticles on chemically modified substrate¹⁸⁻¹⁹, nanolithography e.g., nanosphere lithography²⁰⁻²¹ and electron-beam lithography²²⁻²³, and evaporation of thin layer of metal on glass surface followed by annealing²⁴. Although immobilized nanoparticles (e.g., nanorods, nanostar, nanoprisms, nanorice) show better LSPR response, there are some drawbacks with regards to stability and reproducibility.²⁵ In addition, aggregation of nanoparticles is always a problem and nanoparticles may not be completely free from stabilizer, used to avoid aggregation, which will directly affect the sensitivity measurements and binding experiments.²⁶ To avoid these limitations, nanolithography technique has been developed where templates are used to fabricate different nanostructures. One of the popular nanolithography techniques is nanosphere lithography.²⁷ In this method, polystyrene nanospheres of various diameters are used as deposition masks on glass substrates. These nanospheres self-assemble in hexagonally close-packed pattern on substrate, such that metals can be deposited in gap between the nanospheres. The nanospheres can then be removed by sonicating the substrate in organic solvents leaving behind the triangular or spherical nanostructures as periodical array.²⁸⁻²⁹ The popularity of this method is because it is cheaper, simpler, and do not require any sophisticated instrumentation.³⁰ However, there are possibilities of various types of defects in this method as a result of nanospheres polydispersity, site randomness, point defects, line defects, and polycrystalline domains.²⁸ Furthermore, concentration of nanospheres directly plays role in arrangement of nanospheres on substrate²⁸ which

means variety of structures may be formed within the same substrate if proper concentration cannot be maintained. Other lithography techniques like electron beam lithography can make nanostructures precisely without any defects;³¹ however, this technique is expensive and requires more time and expertise to fabricate nanostructures.²⁸ Evaporating a thin layer of metal on glass surface followed by an annealing technique is also cheaper and simple;³² however, nanostructure polydispersity and limitation to spherical shapes restricts this method from being method of choice for nanofabrication. All of these examples show that more research needs to be performed in this field for producing sensitive and stable nanostructures, so that LSPR spectroscopy would become method of choice for bio/chemical sensing. Besides LSPR spectroscopy, nanostructured transducer is also used in surface enhanced Raman spectroscopy (SERS),³³ a very sensitive analytical technique whose detection limit is in single molecular level,³⁴⁻³⁵ which once again emphasize the importance of research in nanostructure fabrication.

LSPR has been compared to traditional surface plasmon resonance (SPR),³⁶ and is found to be quite competitive on the basis of a number of features, especially cost. SPR experiments are based upon propagating surface plasmons, often at the surface of a flat gold film, whose thickness should be near 50 nm, and supported on a prism or waveguide. Many of the SPR experiments reported use commercial Biacore instruments along with supplied sensor chips. SPR can be performed in a variety of modes, the most popular being measurement of the shift of the resonance angle with analyte binding to the gold surface modified with some sort of recognition layer. Both SPR and LSPR can be conducted in imaging mode. For SPR the element size must be approximately 10 microns, while for LSPR single supported nanoparticles and changes occurring on them

can be imaged.³⁷ For a basic LSPR measurement on an ensemble of nanostructures, by either transmission or reflection geometry, the cost of instrumentation is a small fraction (as little as 1/60th) of the cost of a commercial Biacore instrument, thus far adopted as a standard by much of the life science community. Real-time detection is possible with LSPR as it is with SPR. For LSPR experiments conducted in transmission mode, extinction at a specific wavelength or resonant wavelength versus time can be followed, while in reflection mode reflectivity at a chosen wavelength or resonant wavelength versus time can be followed. As noted by Van Duyne group, the refractive index sensitivity of LSPR is much lower than that of SPR; however, the plasmon for SPR (200–300 nm), and hence a high level of sensitivity to molecular binding at the surface can still be achieved. The lower bulk refractive index sensitivity of LSPR does provide an advantage of simplicity in that close temperature control is less essential. Recent reviews have covered the variety of nanostructures developed for use with LSPR.³⁷⁻³⁸

SPR has played a major role in probing many types of biomolecular interactions, including protein–carbohydrate and lectin–glycoprotein binding. The applications of SPR to study carbohydrate-binding interactions have been reviewed, and compared with other analytical methods.³⁹ The use of imaging SPR to study binding to carbohydrate arrays is especially promising for screening carbohydrate–protein interactions.⁴⁰⁻⁴¹ Approaches based on coupling derivatized carbohydrates to activated SAMs, often in the presence of a diluting species terminated in oligoethylene glycol units known to minimize non-specific protein adsorption, have been pursued using Diels–Alder reactions,⁴² disulfide-thiol exchange,⁴³ and click chemistry⁴⁴. Use of Biacore sensor chips pre-modified with a carboxymethylated dextran gel to which amine derivative glycans can be bound after

NHS activation has been reported.⁴⁵ This widely used type of sensor chip has the potential complication that the lectin Con A, for example, has an affinity for the dextran component.⁴⁶ Mixed SAMs of a carbohydrate component and diluting species have also been prepared directly and studied using SPR.⁴⁷ Efforts have been made to precisely control the spacing between sugars using cyclic peptides presenting a specified number of mannose units and to examine the influence of this on the multivalency and clustering effects that can occur during lectin binding.⁴⁸⁻⁴⁹

The studies reported in which LSPR has been applied to studying protein binding to a carbohydrate modified nanostructure have primarily been carried out in transmission mode. In an early study, the results for studying a protein–carbohydrate interaction using LSPR and SPR were directly compared.⁵⁰ Mixed SAMs of a triethylene glycol terminated disulfide and a maleimide terminated analog were formed on silver triangular nanoprisms formed by nanosphere lithography on glass slides. Reaction of maleimide with a mannose thiol derivative gave about 5% mannose coverage available for interaction with Con A. Experiments were conducted in transmission mode, and both the peak wavelength and the magnitude of its shift due to Con A binding were found to depend on the aspect ratio of the nanoprisms. The modified Ag triangular nanoprisms were resistant to non-specific protein binding and were suitable for following Con A binding in real-time by monitoring the peak wavelength as a function of time, with comparable results for SPR found by monitoring the resonance angle versus time using a Biacore instrument. The response during the dissociation phase was markedly different for LSPR from SPR, and dependent on the aspect ratio of the triangular nanoprisms which was found to influence the plasmon decay length. Au nanoparticles supported on glass have been modified by

polymer brushes with many pendant glucose residues and LSPR was used to determine a binding constant from real-time analysis of $5.0 \pm 0.2 \times 10^5 \text{ M}^{-1}$ noted as larger than that for Con A binding to methyl α -D-glucopyranoside of $2.4 \pm 0.1 \times 10^3 \text{ M}^{-1}$ in solution and attributed to multipoint binding effects.⁵¹ The use of supported gold nanoparticles modified with a polymer brush having pendant mannose units was applied to follow Con A binding.⁵² An apparent association constant determined from analysis of real-time association kinetics data $7.4 \pm 0.1 \times 10^6 \text{ M}^{-1}$ greater than that for Con A to methyl α -D-mannopyranoside in solution $7.6 \pm 0.2 \times 10^3 \text{ M}^{-1}$ is due to multipoint binding effects. Au nanoparticles bound to glass modified by 3-aminopropyltrimethoxysilane were modified by dodecanethiol SAMs into which a N-acetylglucosamine glycolipid was inserted, and shift in the LSPR peak wavelength due to Con A binding was observed in transmission mode in real-time for both association and dissociation.⁵³ A recent study aimed at optimizing supported Au nanoislands formed on glass by evaporation.⁵⁴ Mixed SAMs were formed of alkanethiol derivatives with a penta(ethylene glycol) segment terminated in -OH, mannose, or galactose. The response to Con A binding in terms of peak wavelength shift or shift in extinction at a fixed optimal wavelength was found to be greatest for Au islands of average height 2.5 nm. The optimal combination of refractive index sensitivity and plasmon decay length was required to obtain the maximum response to Con A binding. Analysis of real-time binding kinetics data gave a value for K_a of $7.7 \times 10^6 \text{ M}^{-1}$. Glyconanoparticles presenting different sugars have been shown to differentiate between a set of 4 lectins using a pattern recognition approach.⁵⁵

In this chapter, we demonstrate a facile electrochemical method for preparing novel nanostructured gold film (NGF) which can be used as LSPR-based transducer. The

NGF prepared by this method is robust and sensitive compared to gold nanostructures films prepared by other methods. We will show how LSPR peak and RI sensitivity change with changes in nanostructure's shape and size which can be controlled by changing different dependable parameters. We will also demonstrate how a bioassay can be performed on NGF surface using LSPR spectroscopy by taking carbohydrate–lectin as a model. The interaction between carbohydrate and lectin is chosen because this type of interaction is predominant in many fundamental biological processes such as cellular recognition, inflammation, signal transduction, cell adhesion, and cancer cell metastasis.⁵⁶⁻⁵⁷ Concanavalin A (Con A), 104 kDa, originally obtained from jack bean, *Canavalia ensiformis*, is used as a model lectin.⁵⁸ It is a mannose specific lectin⁵⁹ and exists as tetramer above pH 7.0 and dimer below 6.0.⁶⁰ Here, we will show the interaction of Con A to thiolated mannoside (α Man-C₈-SH) immobilized on NGF surface at pH 7.4.

4.2 Results and Discussions

4.2.1 Nanostructured gold film (NGF) Preparation

NGFs were prepared using one-step and two-step chronoamperometry (CA) technique. When we used one-step CA by applying different potentials from -0.8 to -1.4 V with the increment of -0.2 V for 60 or 90 s, we found that films formed at -1.4 V are not very stable and got easily peeled off of glass slides. However, the films formed at -1.2 V or below are very stable with -1.2 V showing distinct LSPR peaks with reference to flat gold surface with the film prepared at 60 s showing the sharper peak compared to 90 s. This is due to rough structures formed at -1.2 V compared to the structures formed at lower potentials. However, bulk RI sensitivity of the structured formed at -1.2 V is

very low. Therefore, we chose two-step CA with -1.2 V as the initial potential and varying the second potential from -1.0 to -1.6 V for 30 s. The time for the second potential is fixed to 30 s as the peak becomes broader with 60 s deposition decreasing sensitivity of nanostructures. **Figure 4.1A** and **B** illustrates the detailed schematic diagram of NGF preparation technique.

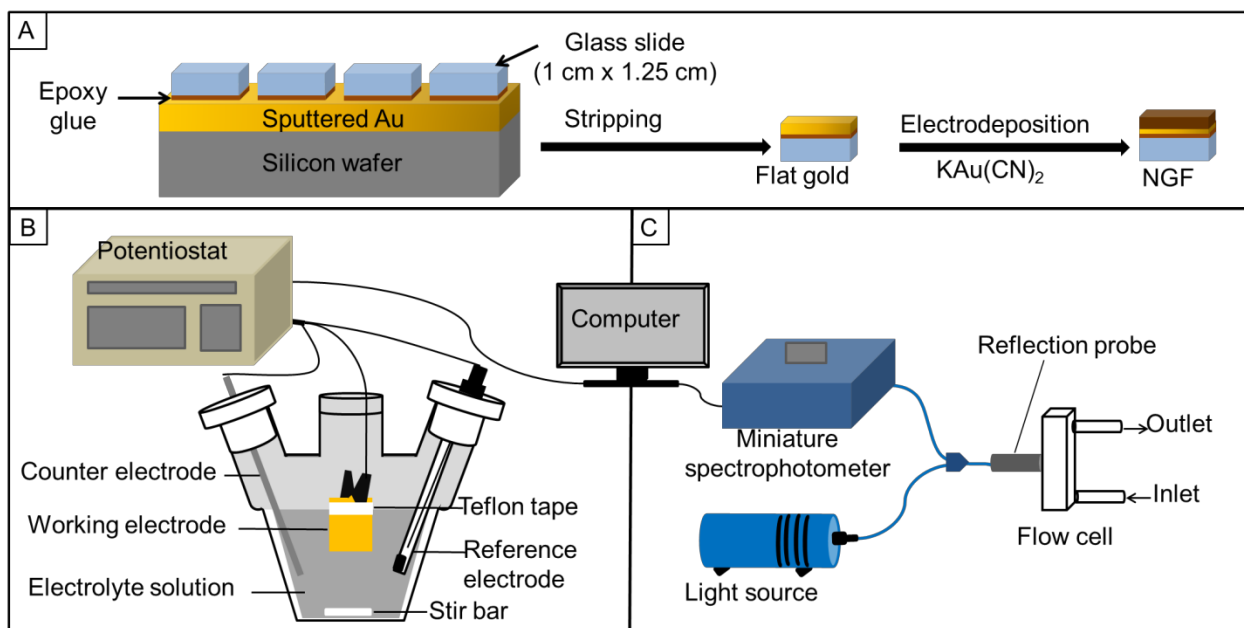


Figure 4.1 Schematic depiction of (A) nanostructured gold film fabrication steps (B) electrochemical setup for nanostructured gold film fabrication and (C) optical setup for localized surface plasmon resonance spectroscopy (reflection mode).

Figure 4.2A shows photographic images of gold sputtered silicon wafer containing attached glass slides. Flat gold surface was obtained by stripping the glass slide off the silicon wafer. Color comparison of gold surface before and after electrodeposition is shown in **Figure 4.2B**. The difference in surface color before and after the electrodeposition can be distinctly seen thorough unaided eyes. Flat gold has

faint golden color, whereas after electrodeposition the NGF formed shows a darker golden and slightly brownish color (**Figure 4.2B**).

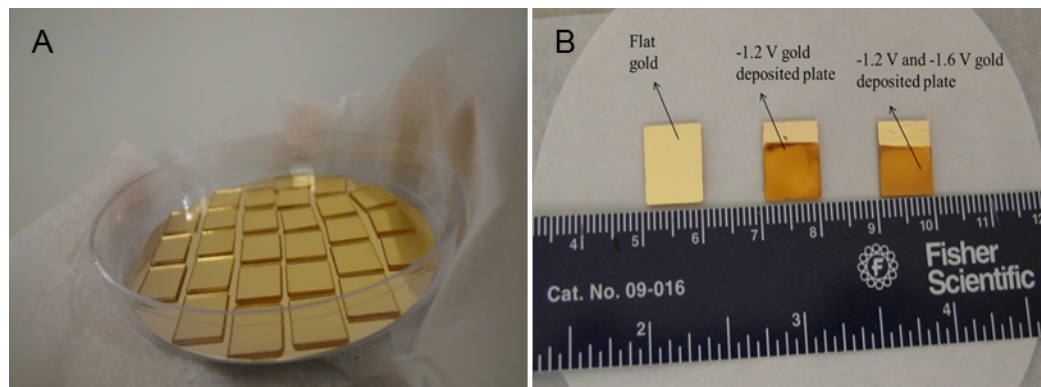


Figure 4.2 Photographic images of (A) flat gold surface on glass slide before stripping off of silicon wafer and (B) showing changes on gold surface before and after electrodeposition.

The chronoamperometric curves obtained during preparation of nanostructured films at different potentials are shown in **Figure 4.3A**. The chronoamperometric curves show the general trend of increasing current with increasing potential and vice versa. The corresponding extinction spectra of NGFs under N_2 are shown in **Figure 4.3B**. We have found that the peak wavelength of NGF prepared by depositing 90 s is around 520 nm whereas the structure that was formed by depositing for 60 s has peak wavelength at around 500 nm.

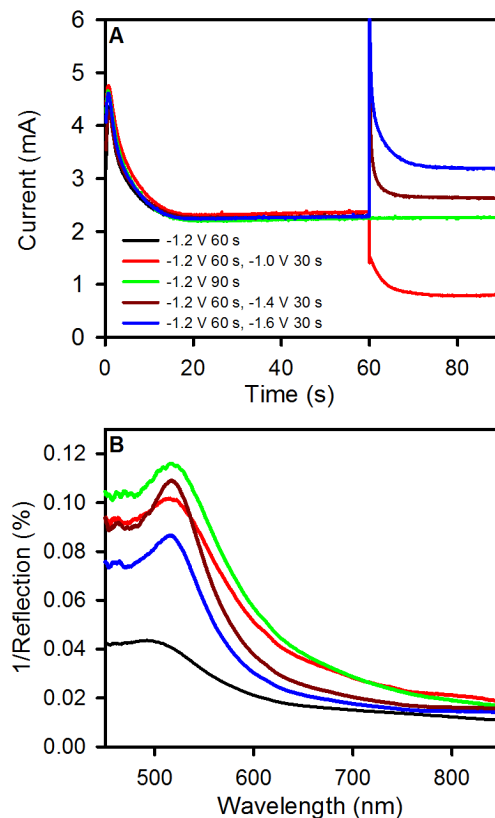


Figure 4.3 (A) Chronoamperometric curves obtained during the preparation of NGFs by applying different potentials and times (indicated). (B) LSPR spectrum of corresponding NGFs recorded in a nitrogen environment.

The morphology of thin films changed drastically when we changed potential as can be seen on SEM images (**Figure 4.4**). The NGF prepared at both -1.2 V for 60 and 90 s look almost similar and has randomly distributed different types of nanostructured features with 90 s deposition has slightly bigger nanostructures (**Figure 4.4A,B**). The nanostructures formed at second potential of -1.0 V for 30 s are also diverse but relatively smaller (**Figure 4C**). **Figure 4D,E** represents images of NGFs prepared at -1.2 V for 60 s followed by -1.4 V for 30 s and -1.6 V for 30 s, respectively. We can see

brick shaped nanostructure all over the surface having length of around 200 nm and width of around 100 nm.

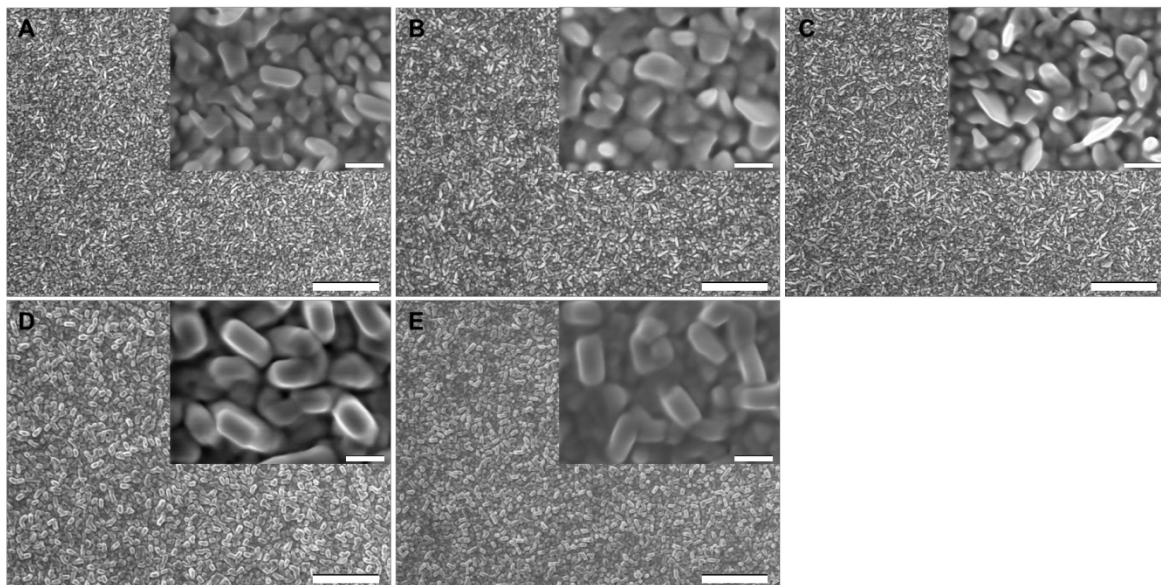


Figure 4.4 SEM images of NGFs prepared using (A,B) one-step chronoamperometry technique, -1.2 V for 60 s and -1.2 V for 90 s, respectively and (C–E) two-step chronoamperometry technique, -1.2 V for 60 s followed by -1.0 V for 30 s, -1.2 V for 60 s followed by -1.4 V for 30 s, and -1.2 V for 60 s followed by -1.6 V for 30 s, respectively. Scale bar: 2 μm . Insets are the corresponding high-magnification SEM images. Scale Bar: 0.2 μm .

4.2.2 Refractive index sensitivity (RIS) test

To check the bulk refractive index sensitivity of prepared NGFs we injected the liquid having different RI, water ($n = 1.33$), 15% glycerol ($n = 1.35$), 30% glycerol ($n = 1.37$), 45% glycerol ($n = 1.39$), 60% glycerol ($n = 1.41$), and 75% glycerol ($n = 1.43$), through the NGF surface inside flow cell and recorded the extinction spectrum. We have found that the nanostructure prepared by two-step CA using potential -1.2 V for 60 s

followed by -1.4 or -1.6 V for 30 s exhibit better red shift in the peak wavelength and increase in extinction with the increase in RI. **Figure 4.5** is the representative bulk RIS test performed on NGF prepared using two steps (-1.2 V 60 s followed by -1.6 V 30 s) and one step (-1.2 V 90 s) technique for comparison.

When we plotted the peak wavelength or inverse of reflectance versus the indices of refraction, a linear dependence of wavelength and inverse of reflectance with RI can be seen. The slope of line gives the bulk RIS value which is 100 ± 2 nm RIU⁻¹ for NGF prepared at -1.2 V 60 s followed by -1.6 V 30 s with FOM = 1.7 and 58 nm RIU⁻¹ for NGF prepared at -1.2 V 90 s with FOM = 0.8. **Table 4.1** shows the sensitivity comparison of NGFs prepared under different reported conditions. It has been found that the structures prepared by applying the second potential higher than -1.2 V shows better bulk RIS and figure of merit. Distinct nanostructured brick like feature having aspect ratio of 2 and the inter-nanostructure gap should be the cause that this structure shows better plasmonic response compared to other structures formed.⁶¹⁻⁶² When we increased the second potential to -1.8 V, it caused peeling of gold film.

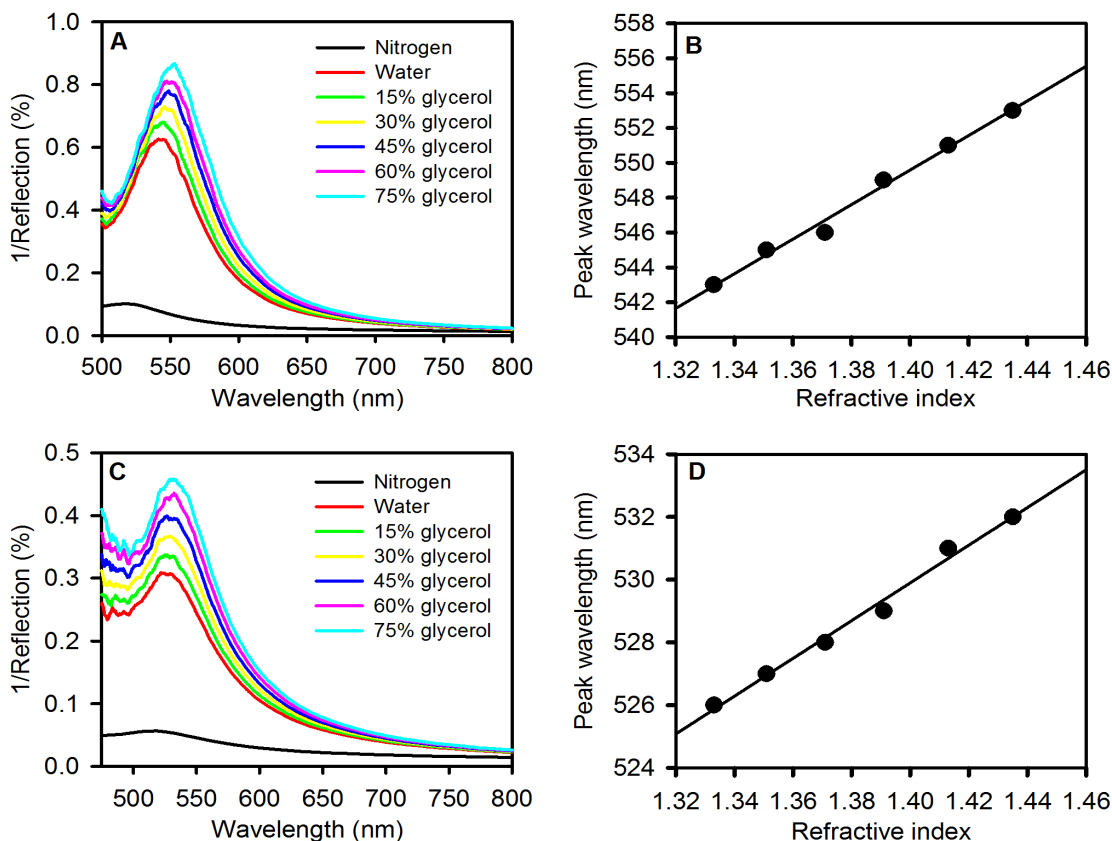


Figure 4.5 (A) Bulk refractive index response of nanostructured gold films prepared using electrodeposition conditions of -1.2 V for 60 s, and then -1.6 V for 30 s. LSPR spectra obtained at different refractive indices (n) = 1, 1.33, 1.35, 1.37, 1.39, 1.41, and 1.43 in nitrogen, water, 15, 30, 45, 60, and 75% glycerol, respectively. The nitrogen peak is the lowest and the peaks move upward in the graph with increasing refractive index. (B) Plot of peak wavelength versus refractive index for the spectra shown in (A). (C) LSPR spectra showing the bulk RIS response at the same series of refractive index values for nanostructured gold film prepared using electrodeposition at -1.2 V for 90 s. (D) Plot of peak wavelength versus refractive index for the spectra shown in (C).

Table 4.1 Sensitivity of NGF prepared under different conditions.

Conditions	Bulk RIS (nm/RIU)	FOM	Initial peak wavelength (nm)
-1.2 V 60 s	52 ± 4	0.9	499
-1.2 V 60 s, -1.0 V 30 s	58 ± 2	0.8	517
-1.2 V 90 s	58 ± 2	0.8	516
-1.2 V 60 s, -1.4 V 30 s	84 ± 2	1.4	518
-1.2 V 60 s, -1.6 V 30 s	100 ± 2	1.7	518

Higher bulk RIS and FOM have been reported previously for different shape and size of nanostructures.¹⁵ Even if shape and size are similar, nanostructure made from silver shows higher sensitivity compared to nanostructures made from gold.¹⁵ However, it has also been found that nanostructures can show better sensitivity when their initial LSPR peak falls toward higher wavelength.⁶³ Therefore, the structures that show higher RIS and FOM may be because their LSPR peak wavelength falls near the end of visible or IR-region which hinders the possibility of miniaturizing the LSPR-based biosensor. For making the spectra to shift within visible region even after immobilization of biomolecules and obtaining spectra under inert gas or buffers, the initial LSPR peak wavelength should be around 500 nm so that there is enough space for spectra to shift within visible region. However, the RIS of the nanostructures that have initial LSPR peak

position at around 500 nm is relatively low compared to the one that have initial LSPR peak position at higher wavelength. For gold nanostructures having initial LSPR peak wavelength of around 500 nm have reported value from 44 nm RIU⁻¹ depending on shape, size and composition.⁶⁴ Relatively free nanoparticles have higher sensitivity compared to films, but are difficult to handle and reproduce. They also create the problem while using them as biosensors, as some stabilizing agents are always left to nanoparticles to avoid aggregation.²⁶ Therefore, NGF was prepared not only to overcome the shortcomings of the free nanoparticles-based biosensor, but also to perform better sensitivity within the visible region.

4.2.3 Biosensing

4.2.3.1 Carbohydrate–lectin interaction

Because LSPR extinction peak position depends on the change in refractive index around the structures, we can apply this idea for studying biomolecules interactions. When binding occurs on the surface of nanostructures, the RI around the surface of the nanostructures increases compared to its initial RI, which red shifts the LSPR extinction peak wavelength, and increases the intensity of the peak. This phenomenon can be used to prepare a biosensor.

We have studied the interaction between mannose and Con A on the surface of NGF to show its sensitivity, the schematic representation of which was shown in **Figure 4.6**. For this purpose, we made carbohydrate-based biosensor where NGFs prepared under -1.2 V 60 s, -1.6 V 30 s was used as a transducer as it shows comparatively higher sensitivity. Mixed SAMs of thiolated mannoside and TEG worked as immobilized

bioreceptors whereas Con A was used as analyte to be detected. Mixed SAMs are formed instead of single SAMs to control nonspecific interactions, decrease steric effects between bioreceptor head group and to control the density of Con A.⁶⁵⁻⁶⁷

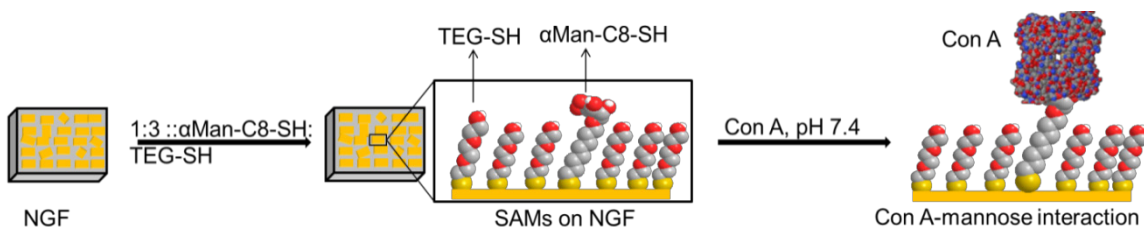


Figure 4.6 Schematic diagram of binding of Concanavalin A to thiolated mannoside immobilized on NGF surface.

Figure 4.7A shows that the initial LSPR peak wavelength of NGF modified with mixed SAM is at 521 nm, 2 nm red shifted from the unmodified NGF surface which was initially at 519 nm in a nitrogen environment. When we immobilized Con A on the SAMs modified NGF, by injecting 0.5 μ M Con A inside the flow cell for 1 h and washed thoroughly with buffer and water, the peak wavelength was found at 528 nm in a nitrogen environment. For the control experiment, we perform the similar experiment by injecting BSA through flow cell but no significant shift in either peak intensity or peak wavelength was observed. We conclude this is due to lack of specific or non-specific interaction between mannoside and BSA.

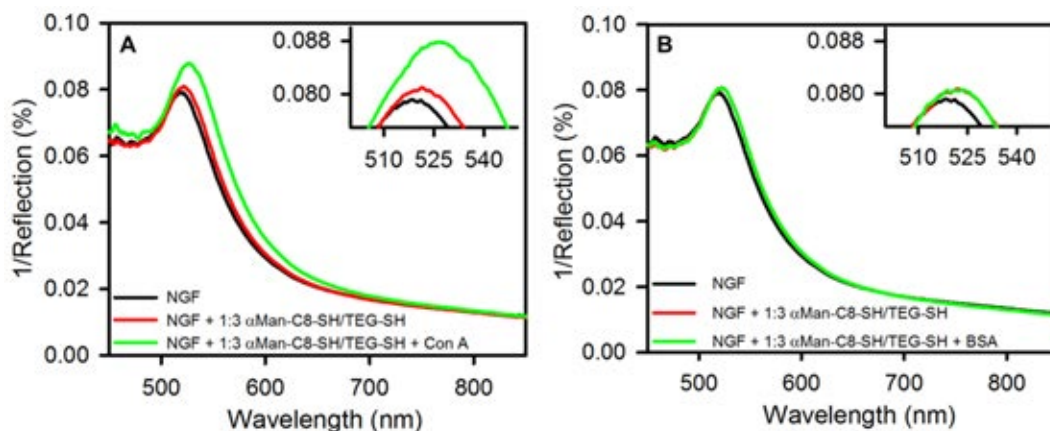


Figure 4.7 LSPR spectra of NGF, unmodified (black), modified with mixed SAMs of α Man-C8-SH and TEG-SH prepared from 1:3 solution molar ratio (1 mM total concentration in ethanol, 2 h (red) and after immobilization of 0.5 μ M proteins for 1 h (green) (A) Concanavalin A and (B) bovine serum albumin.

To further support the experiment, we performed the mannose–Con A interaction study using electrochemical impedance spectroscopy (EIS). The Nyquist plot obtained from EIS shows characteristic semicircle at the high-frequency region whose diameter represents charge transfer resistance (R_{ct}) and a straight line at the low-frequency region representing diffusion process. The Nyquist plot of unmodified, SAMs modified and Con A immobilized NGF is shown in **Figure 4.8**. The Nyquist plot for the unmodified NGF gives a very small charge transfer resistance value ($R_{ct} = 10 \Omega$). A small semicircle in the Nyquist plot at high frequencies has been reported previously for bare gold surface. Values of R_{ct} can only be directly compared if reported in units of $\Omega \text{ cm}^2$ to account for electrode surface area. The geometric surface area of our NGF used as an electrode that is exposed to the solution is 1.0 cm^2 , and the roughness factor is estimated to be near 1.4 on the basis of gold oxide stripping. Thus value of R_{ct} for the bare NGF surface is estimated

to be $14 \Omega \text{ cm}^2$ accounting for electrode area. This value can be compared with those of $24.4 \Omega \text{ cm}^2$ on bare Au(111), and $34 \Omega \text{ cm}^2$ (reported on a polished gold electrode of 1.6 mm diameter whose electroactive surface area was determined by application of the Randles-Sevcik equation), and $35.2 \Omega \text{ cm}^2$ (reported on a bare gold electrode of 2 mm diameter) using the electrode areas reported. On analyzing the mixed SAMs on NGF we found a subsequent increase in the interfacial charge transfer resistance ($R_{\text{ct}} = 30 \Omega$) which increases considerably after incubation with $0.5 \mu\text{M}$ Con A in buffer ($R_{\text{ct}} = 225 \Omega$) indicating specific binding of Con A to mannose in the SAM.

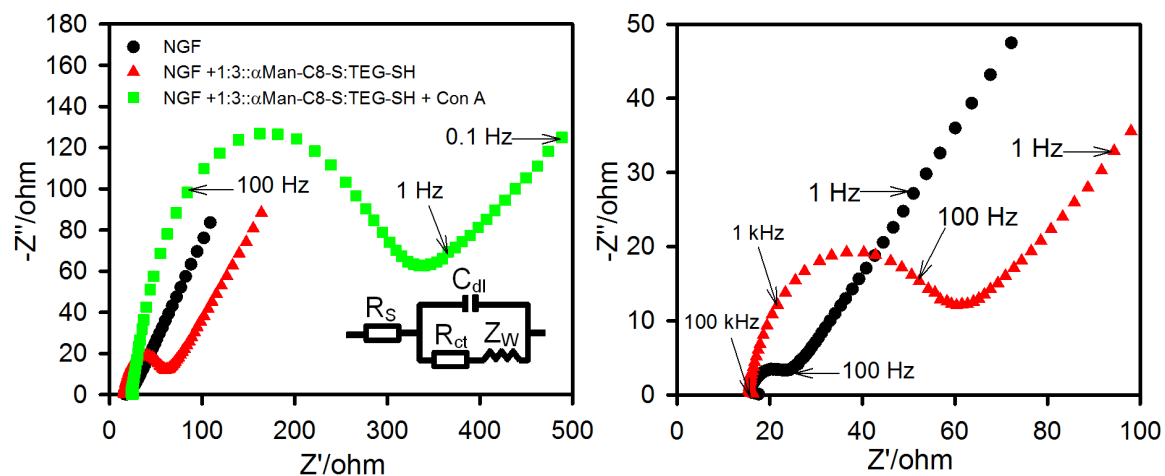


Figure 4.8 Nyquist diagram (Z' vs. Z'') for Faradic impedance measurement of NGF in 10 mM PBS buffer pH 7.4 containing 5 mM $\text{K}_3[\text{Fe}(\text{CN})_6]/\text{K}_4[\text{Fe}(\text{CN})_6]$ (1:1 mixture), unmodified (black), modified by mixed SAMs (red), and after Con A immobilization (green). The impedance spectra were recorded within frequency range of 100 kHz to 0.1 Hz. Inset is equivalent circuit used to model impedance data. The panel on the right shows an expanded view of the high-frequency data for the bare NGF and the SAM-modified NGF.

Both LSPR and EIS data provided similar types of response for mannose Con A binding; however, an advantage of LSPR over EIS is that it can be used to study binding directly in situ in real time. Therefore, we performed real-time interaction study of mannose and Con A on the surface of NGF. It is common practice that the real-time interactions studies are performed using change in intensity of extinction peak.⁶⁸ For this purpose, we placed the mixed SAMs modified NGF in the flow cell and Tris buffer was run through the flow cell. The intensity was recorded at constant wavelength of 557 nm. This wavelength was chosen above the LSPR peak for the SAM modified NGF in buffer (546 ± 2 nm) because as we immobilize the protein the change in both intensity and wavelength occurs. If we had chosen the constant wavelength at peak intensity, the shift after protein immobilization doesn't properly represent the intensity shift of peak. This has been explained before by Rubinstein group. For our experiment, we injected Con A manually inside the flow cell filled with pure Tris buffer after recording the peak intensity on buffer for 5 min. We can clearly see sharp increase in intensity with the time which is because of increase in refractive of bulk solution and specific and nonspecific binding between mannose and Con A at NGF surface (**Figure 4.9**). When we injected the Tris buffer after 15 min of immobilization, we saw slight decrease in response which is because of washing away of nonspecifically bound Con A on surface.

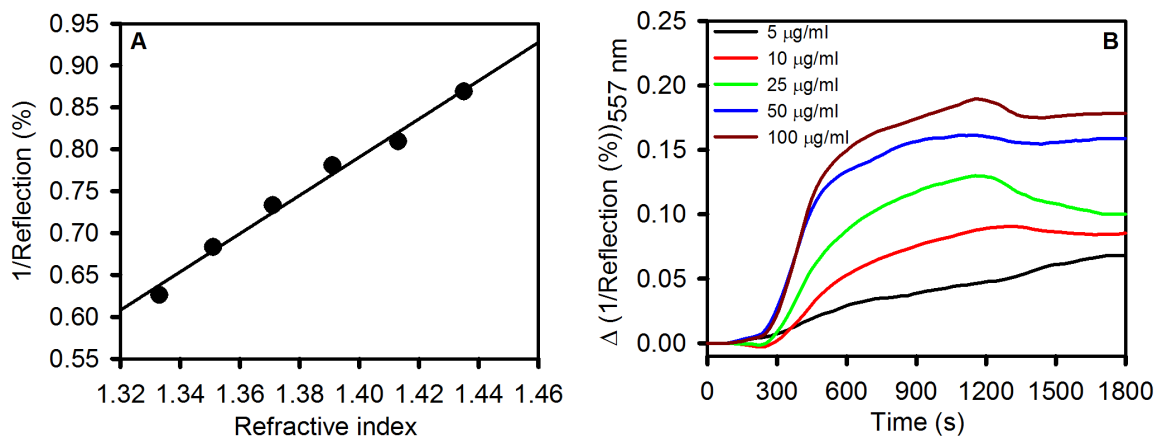
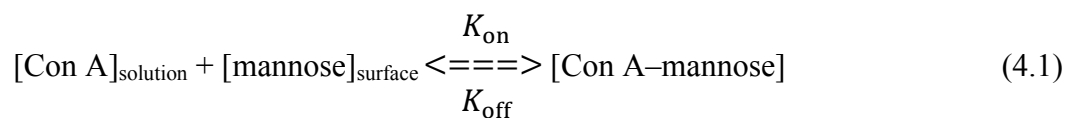


Figure 4.9 (A) Plot of the inverse of the percent reflectance at the peak wavelength versus bulk refractive index for the nanostructured gold film prepared at -1.2 V for 60 s followed by -1.6 V for 30 s. (B) Real-time LSPR response of SAMs modified NGF on injecting a series of concentrations of Con A. Flow cell was filled with buffer for first 5 min followed by manually injecting protein within 30 s, and washing after 20 min.

Real-time LSPR data have been used to determine values of association rate constants (k_{on}), dissociation rate constants (k_{off}), and dissociation equilibrium constant (K_d) using relaxation process.^{51-52, 54}



$$[\text{Con A-mannose}](t) = [\text{Con A-mannose}](\infty) [1 - \exp(-t/\tau)] \quad (4.2)$$

where t is time and τ is relaxation time on gathering the spectra before and after changing refraction around the NGF surface.

Since change in the extinction is directly proportional to the surface concentration of the Con A-mannose complex, eq 2 can be written as

$$\Delta(1/\text{Reflection})(t) = \Delta(1/\text{Reflection})(\infty) [1 - \exp(-t/\tau)] \quad (4.3)$$

It has also been known

$$1/\tau = k_{\text{on}}[\text{Con A}] + k_{\text{off}} \quad (4.4)$$

When we plot $1/\tau$ versus $[\text{Con A}]$, the slope of the line gives k_{on} and the intercept gives k_{off} . The dissociation equilibrium constant (K_d) can be obtained as, $K_d = k_{\text{off}}/k_{\text{on}}$. Association rate constant of mannose to Con A (k_{on}) was determined as $7.76 \times 10^3 \text{ M}^{-1} \text{ s}^{-1}$ and dissociation rate constant (k_{off}) as $2.0 \times 10^{-3} \text{ s}^{-1}$ giving the dissociation equilibrium constant (K_d) of 257 nM (**Figure 4.10 B**). Values of k_{on} $2.0 \times 10^4 \text{ M}^{-1} \text{ s}^{-1}$ and k_{off} $2.6 \times 10^{-3} \text{ s}^{-1}$ corresponding to K_d 130 nM were reported for Con A interacting with SAMs of a thiolated PEG linker terminated in a mannose unit, on 5 nm Au islands as noted by Bellapadrone et al. A range of values of k_{off} from $2.48 \times 10^{-4} \text{ s}^{-1}$ to $1.2 \times 10^{-2} \text{ s}^{-1}$ and k_{on} from $5.2 \times 10^3 \text{ M}^{-1} \text{ s}^{-1}$ to $1.4 \times 10^5 \text{ M}^{-1} \text{ s}^{-1}$, corresponding to K_d values from 42 nM to 423 nM have been reported for the Con A–mannose interaction depending upon measurement method, details of surface modification, and experimental conditions.⁵⁴

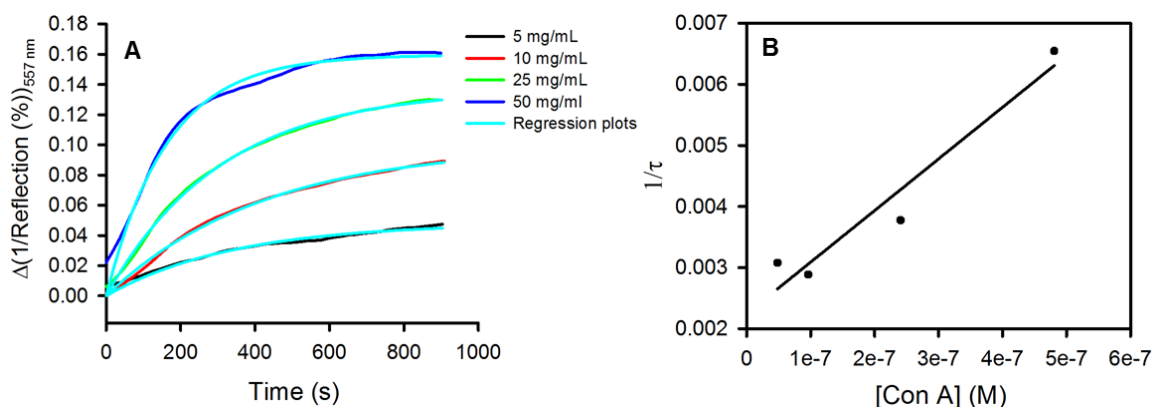


Figure 4.10 (A) Con A binding kinetics curves obtained for different concentration of Con A (indicated). The regression plots of the curves (cyan color) was obtained by fitting the built-in equation for exponential rise to maxima to obtain values of $1/\tau$. (B)

Determination of the binding affinity of Con A to a mannose SAM by plotting $1/\tau$ vs. different concentration of Con A.

4.2.3.2 Detection of carcinoembryonic antigen (CEA) on NGF

Carcinoembryonic antigen (CEA) is a glycoprotein containing nearly 50% carbohydrate with a molecular weight of approximately 200 kDa. This protein is highly expressed in fetal stage of human development for the first 2 trimester of gestation period. Adult human, however, have less than 2 ng/mL in the serum with heavy smokers having slightly greater than 5 ng/mL. A person with cancer, however, has greater than 10 ng/mL of CEA in serum. This makes CEA a good biomarker for early detection of cancer. Early detection of the high level of CEA in serum can help identify the cancer in the early stages, and hence make it easier to treat with less effort. CEA assays are cost-efficient, and helpful in detecting various cancers including colon cancer. There are various optical and electrochemical screening methods for early diagnosis of cancer; however, many methods have limits of detection (LOD) at nearly the diagnostic decision value. This creates challenge for accurately evaluating the biomarkers when slightly changes in concentration happens in serum. A screening method which is easy to perform, and require small sample size, short analysis time, and low cost are current interest of research. LSPR bears the potential to be used as an efficient technique for tumor biomarker detection. **Figure 4.11** shows the schematic of the technique used for the detection of CEA and **Figure 4.12** shows the LSPR spectra generated during different steps of the detection process. **Figure 4.12A** shows that the total shift in peak wavelength on immobilizing 50 $\mu\text{g/mL}$ Con A to EDC/NHS activated 11-mercaptoundecanoic acid is 17 nm in a nitrogen environment. When we passed 100 ng/mL CEA in phosphate buffer

through nitrogen dried Con A, we repeatedly found that instead of CEA immobilizing to Con A, CEA took Con A along with it on washing step, which is evident by LSPR peak going back to the position of SAMs. To overcome this problem, instead of nitrogen drying after Con A immobilization and taking reading, we directly immobilized CEA first and then dried under nitrogen. LSPR peak shift from initial position after this process is 23 nm which is 5 nm more than that after Con A immobilization (**Figure 11.12B**). We believe that this bigger shift is due to CEA immobilized to Con A through mannose present in CEA.

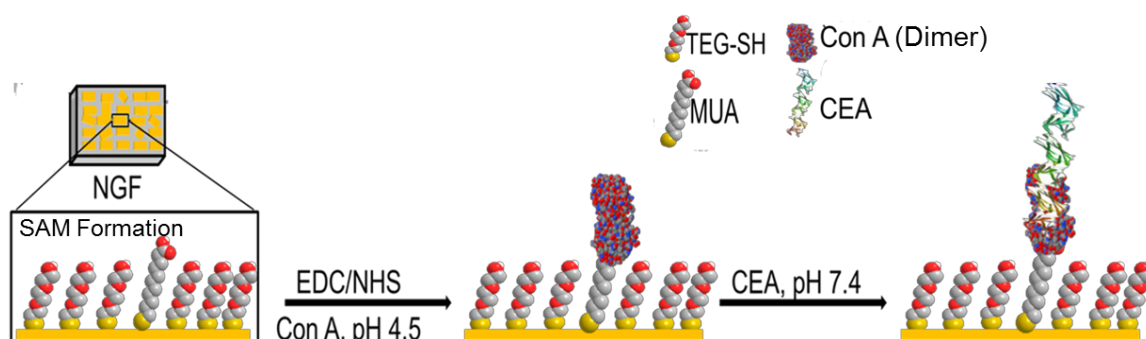


Figure 4.11 Schematic diagram of the technique applied for the detection of CEA using NGF.

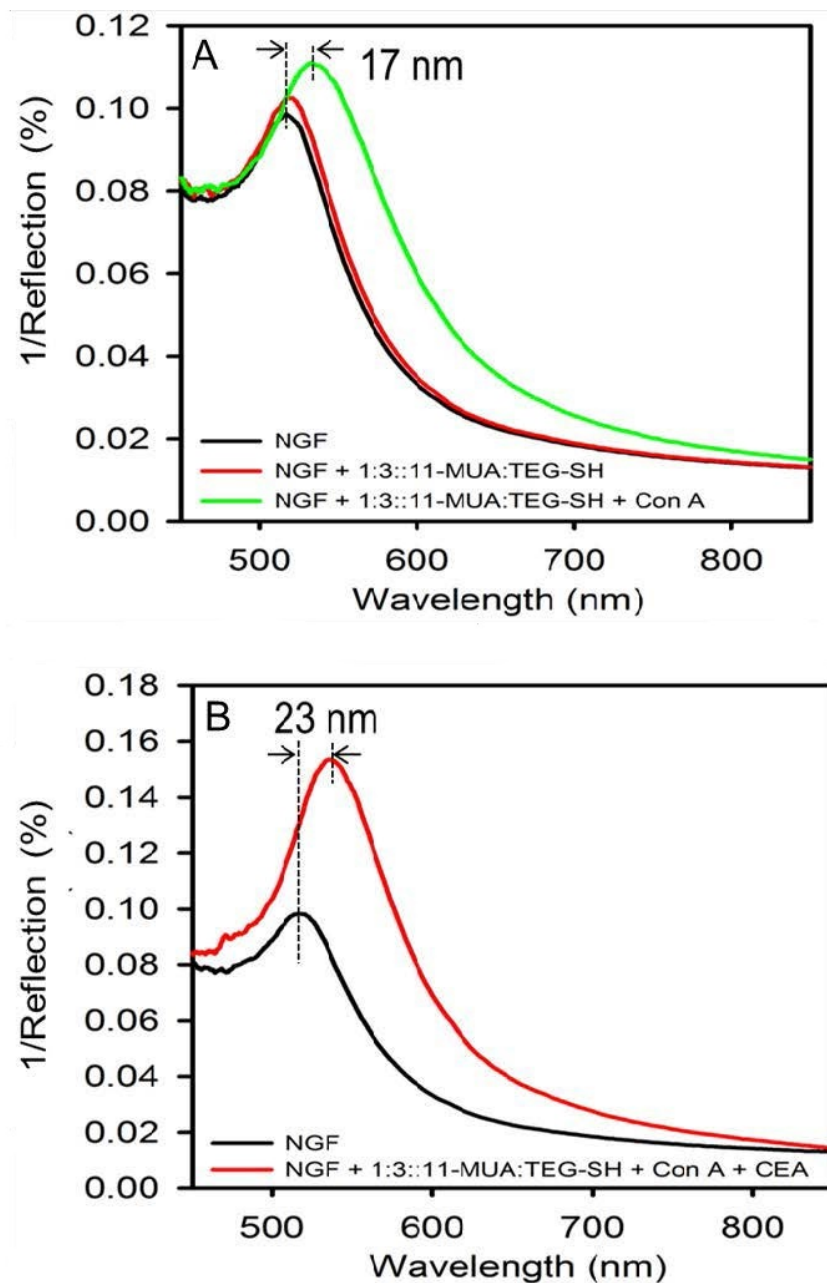


Figure 4.12 (A) LSPR spectra of NGF showing shift by 17 nm on covalent immobilization of Con A on SAMs of 11-mercaptoundecanoic acid (MUA). (B) LSPR spectra shift by 23 nm on interaction of CEA to Con A immobilized as in (A).

4.2.3.3 Layer-by-layer study of molecules

In this part, we tried to demonstrate that NGF substrate can be used to study multilayer interactions of the molecules using LSPR spectroscopy, and the molecules up to about 10 nm away from NGF can be easily detected. NGF prepared using -1.2 V for 60 s followed by -1.6 V for 30 s was used to study this multilayer system of biomolecules, as these conditions generate NGF having higher stability and sensitivity. The LSPR spectra generated during different stages of multilayer formation are shown in **Figure 4.13**. It can be observed that freshly prepared NGF show initial peak wavelength at around 520 nm, which red shifts 2–3 nm on immobilizing SAM of mercaptododecanoic acid (MDDA) on NGF surface. We activated terminal $-\text{COOH}$ group of the MDDA SAM using EDC/NHS chemistry for the immobilization of poly(amido amine) (PAMAM) generation 5 dendrimer having diameter 5.4 nm. The shift in LSPR peak wavelength was found to be 4–4.5 nm after the immobilization of PAMAM G5 dendrimer (5 wt/wt %) on SAM functionalized NGF. On further immobilizing Con A on the dendrimer linking through the activated mannose, further LSPR peak wavelength shift of 5–6 nm was observed.

4.2.4 Regeneration of NGF

Finally, we regenerated the NGF surface as this can reduce the cost of potential use as a transducer for biosensor development. For that purpose, we dipped the biomolecule functionalized NGF plate prepared at -1.2 V 60 s followed by -1.6 V 30 s, inside freshly prepared piranha solution for 45 s and rinsed thoroughly with milli-Q water. The NGF regenerated after this step was tested using different methods. **Figure 4.14A** compares LSPR spectra of freshly prepared unmodified NGF (black) and NGF

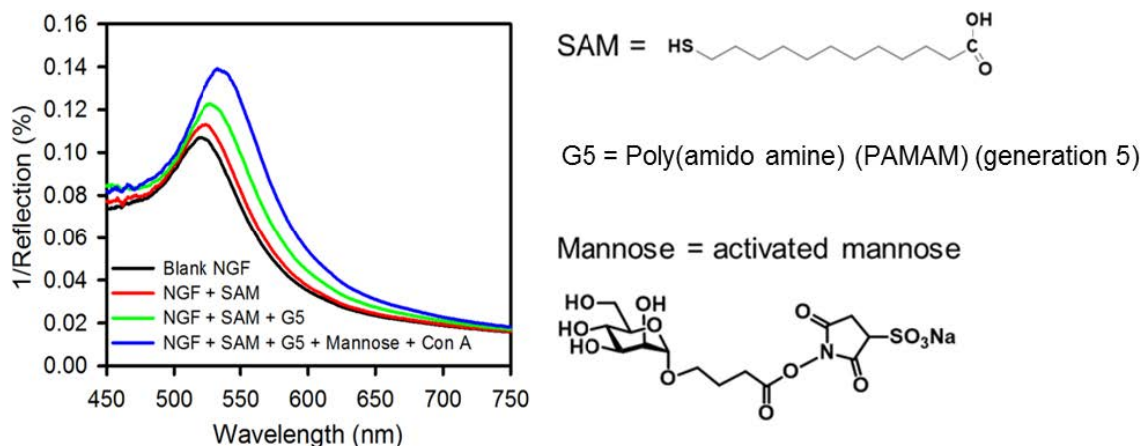


Figure 4.13 LSPR spectra of multi-layer of biomolecules formed on NGF surface: LSPR spectra of (black) blank NGF, (red) MDDA SAMs formed on NGF, (green) immobilized PAMAM dendrimers-G5 on SAM, and (blue) immobilized mannose first formed on G5 followed by Con A on mannose . Spectra were obtained in a nitrogen environment.

obtained after the regeneration (blue). It has been found that the peak wavelength is same for both spectra; however, there is always slight change in the intensity. We believe that the change in intensity is due to slight change in surface position of NGF while loading it back into flow cell after regeneration, and has been reported previously.⁶⁹ We have also performed cyclic voltammetry experiments to conform the complete removal of biomolecules from the surface of NGF. **Figure 4.14B** shows the cyclic voltammograms of freshly prepared unmodified NGF (black), NGF after SAM immobilization (red), NGF after Con A immobilization (green) and NGF after regeneration (blue). It can be seen clearly that unmodified NGF and NGF after regeneration have almost similar broad anodic and cathodic peaks whereas SAM and Con A immobilized NGF do not show any distinct anodic and cathodic peak due to blockage of charge transfer from the electrode surface by the immobilized molecules. The SEM image of NGF after regeneration do not

show any significant different from the freshly prepared NGF (**Figure 4.14C**). Finally, we performed the refractive index sensitivity test on regenerated NGF and found no difference compared to sensitivity of unmodified NGF.

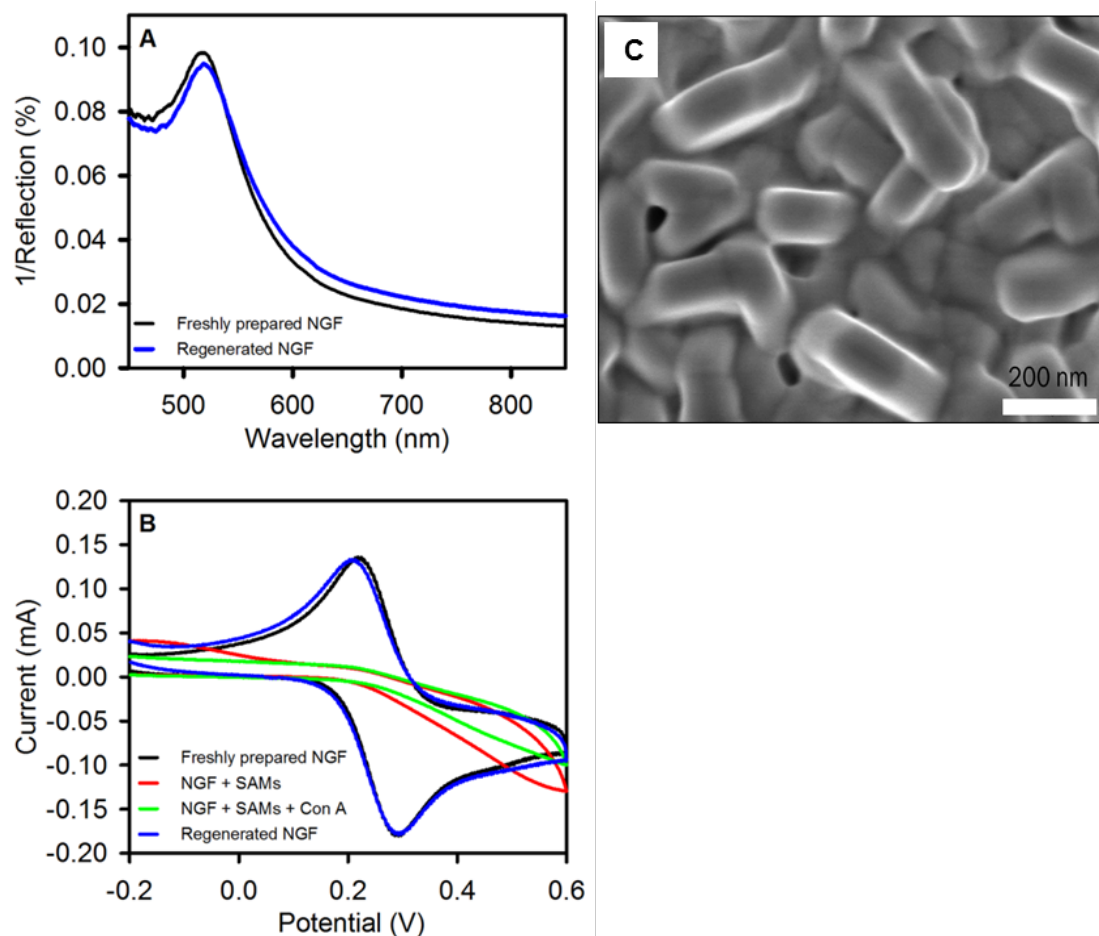


Figure 4.14 Experiments performed to compare freshly prepared and regenerated NGF. (A) LSPR spectra of freshly prepared NGF (black) and regenerated NGF (blue) in a N_2 environment. (B) cyclic voltammograms of freshly prepared NGF (black), SAM immobilized NGF (red), Con A immobilized NGF (green), and regenerated NGF (blue) showing very less difference between regenerated and the freshly prepared NGF. (C) SEM image of NGF after regeneration step showing no distinct difference than that of the freshly prepared NGF.

4.3 Conclusions

Here, we have prepared novel and sensitive nanostructured gold films using facile electrochemical technique and used them as a transducer for LSPR-based spectroscopy. We have found that the structure synthesized by two-step chronoamperometry technique having first potential of -1.2 V for 60 s and second potential higher than -1.2 V for 30 s can produce the sensitive nanostructure films, with reproducible RIS of up to 100 nm RIU^{-1} . The NGFs formed have randomly arranged bricks like nanostructure having length of about 200 nm and width of about 100 nm. As-prepared NGFs are easy to handle, robust and chemically stable showing LSPR peak within the visible region opening the great possibility for miniaturizing the LSPR related transducers.

We used the NGF prepared at -1.2 V for 30 s followed by -1.6 V for 30 s for label-free detection of carbohydrate–protein interactions showing how LSPR peak shifts with specific interaction of mannose and Con A while no shift in the peak was observed for mannose and BSA interaction. This interaction was also demonstrated and conformed using electrochemical impedance spectroscopy on the surface of NGF prepared under similar conditions. We were also able to demonstrate that LSPR-based technique is good to perform real-time bioassay, and different other types of interactions, including lectin–glycoproteins and dendrimer-based carbohydrate–lectin. Finally, biomolecules immobilized NGF was easily regenerated to its original structure and hence the sensitivity, supporting the cheaper alternative for biosensor's transducer.

Improved plasmonics substrates not only support LSPR-based biosensor but can also be used along with SERS technique for detecting small molecules and show promising improvement in photovoltaic cells.

4.4 References

1. Mock, J. J.; Hill, R. T.; Tsai, Y.-J.; Chilkoti, A.; Smith, D. R., Probing Dynamically Tunable Localized Surface Plasmon Resonances of Film-Coupled Nanoparticles by Evanescent Wave Excitation. *Nano Lett.* **2012**, *12* (4), 1757-1764.
2. Jia, K.; Bijeon, J. L.; Adam, P. M.; Ionescu, R. E., Sensitive Localized Surface Plasmon Resonance Multiplexing Protocols. *Anal. Chem.* **2012**, *84* (18), 8020-8027.
3. Dalfovo, M. C.; Salvarezza, R. C.; Ibañez, F. J., Improved Vapor Selectivity and Stability of Localized Surface Plasmon Resonance with a Surfactant-Coated Au Nanoparticles Film. *Anal. Chem.* **2012**, *84* (11), 4886-4892.
4. Blaber, M. G.; Henry, A.-I.; Bingham, J. M.; Schatz, G. C.; Van Duyne, R. P., Lspr Imaging of Silver Triangular Nanoprisms: Correlating Scattering with Structure Using Electrodynamics for Plasmon Lifetime Analysis. *J. Phys. Chem. C* **2011**, *116* (1), 393-403.
5. Endo, T.; Kerman, K.; Nagatani, N.; Takamura, Y.; Tamiya, E., Label-Free Detection of Peptide Nucleic Acid–DNA Hybridization Using Localized Surface Plasmon Resonance Based Optical Biosensor. *Anal. Chem.* **2005**, *77* (21), 6976-6984.
6. Haes, A. J.; Chang, L.; Klein, W. L.; Van Duyne, R. P., Detection of a Biomarker for Alzheimer's Disease from Synthetic and Clinical Samples Using a Nanoscale Optical Biosensor. *J. Am. Chem. Soc.* **2005**, *127* (7), 2264-2271.
7. Endo, T.; Kerman, K.; Nagatani, N.; Hiepa, H. M.; Kim, D.-K.; Yonezawa, Y.; Nakano, K.; Tamiya, E., Multiple Label-Free Detection of Antigen–Antibody Reaction Using Localized Surface Plasmon Resonance-Based Core–Shell Structured Nanoparticle Layer Nanochip. *Anal. Chem.* **2006**, *78* (18), 6465-6475.
8. Chan, G. H.; Zhao, J.; Hicks, E. M.; Schatz, G. C.; Van Duyne, R. P., Plasmonic Properties of Copper Nanoparticles Fabricated by Nanosphere Lithography. *Nano Lett.* **2007**, *7* (7), 1947-1952.
9. Jensen, T. R.; Malinsky, M. D.; Haynes, C. L.; Van Duyne, R. P., Nanosphere Lithography: Tunable Localized Surface Plasmon Resonance Spectra of Silver Nanoparticles. *J. Phys. Chem. B* **2000**, *104* (45), 10549-10556.
10. Mayer, K. M.; Lee, S.; Liao, H.; Rostro, B. C.; Fuentes, A.; Scully, P. T.; Nehl, C. L.; Hafner, J. H., A Label-Free Immunoassay Based Upon Localized Surface Plasmon Resonance of Gold Nanorods. *ACS Nano* **2008**, *2* (4), 687-692.
11. Willets, K. A.; Van Duyne, R. P., Localized Surface Plasmon Resonance Spectroscopy and Sensing. *Annu. Rev. Phys. Chem.* **2007**, *58* (1), 267-297.
12. Stewart, M. E.; Anderton, C. R.; Thompson, L. B.; Maria, J.; Gray, S. K.; Rogers, J. A.; Nuzzo, R. G., Nanostructured Plasmonic Sensors. *Chem. Rev.* **2008**, *108* (2), 494-521.
13. Rycenga, M.; Cobley, C. M.; Zeng, J.; Li, W.; Moran, C. H.; Zhang, Q.; Qin, D.; Xia, Y., Controlling the Synthesis and Assembly of Silver Nanostructures for Plasmonic Applications. *Chem. Rev.* **2011**, *111* (6), 3669-712.
14. Wiley, B. J.; Im, S. H.; Li, Z.-Y.; McLellan, J.; Siekkinen, A.; Xia, Y., Maneuvering the Surface Plasmon Resonance of Silver Nanostructures through Shape-Controlled Synthesis. *J. Phys. Chem. B* **2006**, *110* (32), 15666-15675.

15. Mayer, K. M.; Hafner, J. H., Localized Surface Plasmon Resonance Sensors. *Chem. Rev.* **2011**, *111* (6), 3828-3857.
16. Sönnichsen, C.; Franzl, T.; Wilk, T.; Von Plessen, G.; Feldmann, J., Plasmon Resonances in Large Noble-Metal Clusters. *New J. Phys.* **2002**, *4* (1), 93.
17. Zhao, J.; Pinchuk, A. O.; McMahon, J. M.; Li, S.; Ausman, L. K.; Atkinson, A. L.; Schatz, G. C., Methods for Describing the Electromagnetic Properties of Silver and Gold Nanoparticles. *Acc. Chem. Res.* **2008**, *41* (12), 1710-1720.
18. Joshi, G. K.; McClory, P. J.; Muhoberac, B. B.; Kumbhar, A.; Smith, K. A.; Sardar, R., Designing Efficient Localized Surface Plasmon Resonance-Based Sensing Platforms: Optimization of Sensor Response by Controlling the Edge Length of Gold Nanoprisms. *J. Phys. Chem. C* **2012**, *116* (39), 20990-21000.
19. Huang, H.; Tang, C.; Zeng, Y.; Yu, X.; Liao, B.; Xia, X.; Yi, P.; Chu, P. K., Label-Free Optical Biosensor Based on Localized Surface Plasmon Resonance of Immobilized Gold Nanorods. *Colloids Surf., B* **2009**, *71* (1), 96-101.
20. Haes, A. J.; Zhao, J.; Zou, S.; Own, C. S.; Marks, L. D.; Schatz, G. C.; Van Duyne, R. P., Solution-Phase, Triangular Ag Nanotriangles Fabricated by Nanosphere Lithography. *J. Phys. Chem. B* **2005**, *109* (22), 11158-11162.
21. Ormonde, A. D.; Hicks, E. C. M.; Castillo, J.; Van Duyne, R. P., Nanosphere Lithography: Fabrication of Large-Area Ag Nanoparticle Arrays by Convective Self-Assembly and Their Characterization by Scanning Uv-Visible Extinction Spectroscopy. *Langmuir* **2004**, *20* (16), 6927-6931.
22. Barbillon, G.; Bijeon, J. L.; Plain, J.; de la Chapelle, M. L.; Adam, P. M.; Royer, P., Electron Beam Lithography Designed Chemical Nanosensors Based on Localized Surface Plasmon Resonance. *Surf. Sci.* **2007**, *601* (21), 5057-5061.
23. Cao, W.; Elsayed-Ali, H. E., Stability of Ag Nanoparticles Fabricated by Electron Beam Lithography. *Mater. Lett.* **2009**, *63* (26), 2263-2266.
24. Karakouz, T.; Tesler, A. B.; Bendikov, T. A.; Vaskevich, A.; Rubinstein, I., Highly Stable Localized Plasmon Transducers Obtained by Thermal Embedding of Gold Island Films on Glass. *Adv. Mater.* **2008**, *20* (20), 3893-3899.
25. Park, D. K.; Kim, H. I.; Kim, J. P.; Park, J. S.; Lee, S. Y.; Yang, S.-M.; Lee, J.; Chung, C.-H.; Sim, S. J.; Yoo, P. J., Rigidflex Lithography-Based Nanodot Arrays for Localized Surface Plasmon Resonance Biosensors. *Langmuir* **2010**, *26* (9), 6119-6126.
26. Nusz, G. J.; Marinakos, S. M.; Curry, A. C.; Dahlin, A.; Hook, F.; Wax, A.; Chilkoti, A., Label-Free Plasmonic Detection of Biomolecular Binding by a Single Gold Nanorod. *Anal. Chem.* **2008**, *80* (4), 984-989.
27. Jones, M. R.; Osberg, K. D.; Macfarlane, R. J.; Langille, M. R.; Mirkin, C. A., Templated Techniques for the Synthesis and Assembly of Plasmonic Nanostructures. *Chem. Rev.* **2011**, *111* (6), 3736-3827.
28. Haynes, C. L.; Van Duyne, R. P., Nanosphere Lithography: A Versatile Nanofabrication Tool for Studies of Size-Dependent Nanoparticle Optics. *J. Phys. Chem. B* **2001**, *105* (24), 5599-5611.
29. Jensen, T. R.; Duval, M. L.; Kelly, K. L.; Lazarides, A. A.; Schatz, G. C.; Van Duyne, R. P., Nanosphere Lithography: Effect of the External Dielectric Medium on the Surface Plasmon Resonance Spectrum of a Periodic Array of Silver Nanoparticles. *J. Phys. Chem. B* **1999**, *103* (45), 9846-9853.

30. Haes, A.; Duyne, R., A Unified View of Propagating and Localized Surface Plasmon Resonance Biosensors. *Anal. Bioanal. Chem.* **2004**, *379* (7-8), 920-930.
31. Raphael, M. P.; Christodoulides, J. A.; Mulvaney, S. P.; Miller, M. M.; Long, J. P.; Byers, J. M., A New Methodology for Quantitative Lspr Biosensing and Imaging. *Anal. Chem.* **2011**, *84* (3), 1367-1373.
32. Tesler, A. B.; Chuntunov, L.; Karakouz, T.; Bendikov, T. A.; Haran, G.; Vaskevich, A.; Rubinstein, I., Tunable Localized Plasmon Transducers Prepared by Thermal Dewetting of Percolated Evaporated Gold Films. *J. Phys. Chem. C* **2011**, *115* (50), 24642-24652.
33. Haynes, C. L.; Van Duyne, R. P., Plasmon-Sampled Surface-Enhanced Raman Excitation Spectroscopy. *J. Phys. Chem. B* **2003**, *107* (30), 7426-7433.
34. Anker, J. N.; Hall, W. P.; Lyandres, O.; Shah, N. C.; Zhao, J.; Van Duyne, R. P., Biosensing with Plasmonic Nanosensors. *Nat Mater* **2008**, *7* (6), 442-53.
35. Stiles, P. L.; Dieringer, J. A.; Shah, N. C.; Van Duyne, R. P., Surface-Enhanced Raman Spectroscopy. *Annu. Rev. Anal. Chem.* **2008**, *1* (1), 601-626.
36. Stuart, D. A.; Haes, A. J.; Yonzon, C. R.; Hicks, E. M.; Van Duyne, R. P., Biological Applications of Localised Surface Plasmonic Phenomenae. *IEE Proc. Nanobiotechnol.* **2005**, *152* (1), 13-32.
37. McFarland, A. D.; Van Duyne, R. P., Single Silver Nanoparticles as Real-Time Optical Sensors with Zeptomole Sensitivity. *Nano Lett.* **2003**, *3* (8), 1057-1062.
38. Szunerits, S.; Boukherroub, R., Sensing Using Localised Surface Plasmon Resonance Sensors. *Chem. Commun.* **2012**, *48* (72), 8999-9010.
39. Safina, G., Application of Surface Plasmon Resonance for the Detection of Carbohydrates, Glycoconjugates, and Measurement of the Carbohydrate-Specific Interactions: A Comparison with Conventional Analytical Techniques. A Critical Review. *Anal. Chim. Acta* **2012**, *712*, 9-29.
40. Tyagi, A.; Wang, X.; Deng, L.; Ramström, O.; Yan, M., Photogenerated Carbohydrate Microarrays to Study Carbohydrate-Protein Interactions Using Surface Plasmon Resonance Imaging. *Biosens. Bioelectron.* **2010**, *26* (2), 344-350.
41. Fais, M.; Karamanska, R.; Allman, S.; Fairhurst, S. A.; Innocenti, P.; Fairbanks, A. J.; Donohoe, T. J.; Davis, B. G.; Russell, D. A.; Field, R. A., Surface Plasmon Resonance Imaging of Glycoarrays Identifies Novel and Unnatural Carbohydrate-Based Ligands for Potential Ricin Sensor Development. *Chem. Sci.* **2011**, *2* (10), 1952-1959.
42. Houseman, B. T.; Mrksich, M., Carbohydrate Arrays for the Evaluation of Protein Binding and Enzymatic Modification. *Chem. Biol.* **2002**, *9* (4), 443-454.
43. Smith, E. A.; Thomas, W. D.; Kiessling, L. L.; Corn, R. M., Surface Plasmon Resonance Imaging Studies of Protein-Carbohydrate Interactions. *J. Am. Chem. Soc.* **2003**, *125* (20), 6140-6148.
44. Zhang, Y.; Luo, S.; Tang, Y.; Yu, L.; Hou, K. Y.; Cheng, J. P.; Zeng, X.; Wang, P. G., Carbohydrate-Protein Interactions by "Clicked" Carbohydrate Self-Assembled Monolayers. *Anal. Chem.* **2006**, *78* (6), 2001-2008.
45. Nahálková, J.; Švitel, J.; Gemeiner, P.; Danielsson, B.; Pribulová, B.; Petruš, L., Affinity Analysis of Lectin Interaction with Immobilized C- and O- Glycosides Studied by Surface Plasmon Resonance Assay. *J. Biochem. Bioph. Methods* **2002**, *52* (1), 11-18.

46. Ballerstadt, R.; Schultz, J. S., Kinetics of Dissolution of Concanavalin a/Dextran Sols in Response to Glucose Measured by Surface Plasmon Resonance. *Sens. Actuators B Chem.* **1998**, *46* (1), 50-55.
47. Dhayal, M.; Ratner, D. M., Xps and Spr Analysis of Glycoarray Surface Density. *Langmuir* **2009**, *25* (4), 2181-2187.
48. Wilczewski, M.; Van der Heyden, A.; Renaudet, O.; Dumy, P.; Coche-Guerente, L.; Labbe, P., Promotion of Sugar-Lectin Recognition through the Multiple Sugar Presentation Offered by Regioselectively Addressable Functionalized Templates (Raft): A Qcm-D and Spr Study. *Org. Biomol. Chem.* **2008**, *6* (6), 1114-1122.
49. Chen, Y.-X.; Zhao, L.; Huang, Z.-P.; Zhao, Y.-F.; Li, Y.-M., Facile Synthesis of Cyclopeptide-Centered Multivalent Glycoclusters with 'Click Chemistry' and Molecular Recognition Study by Surface Plasmon Resonance. *Bioorg. Med. Chem. Lett.* **2009**, *19* (14), 3775-3778.
50. Yonzon, C. R.; Jeoung, E.; Zou, S.; Schatz, G. C.; Mrksich, M.; Van Duyne, R. P., A Comparative Analysis of Localized and Propagating Surface Plasmon Resonance Sensors: The Binding of Concanavalin a to a Monosaccharide Functionalized Self-Assembled Monolayer. *J. Am. Chem. Soc.* **2004**, *126* (39), 12669-12676.
51. Morokoshi, S.; Ohhori, K.; Mizukami, K.; Kitano, H., Sensing Capabilities of Colloidal Gold Modified with a Self-Assembled Monolayer of a Glucose-Carrying Polymer Chain on a Glass Substrate†. *Langmuir* **2004**, *20* (20), 8897-8902.
52. Kitano, H.; Takahashi, Y.; Mizukami, K.; Matsuura, K., Kinetic Study on the Binding of Lectin to Mannose Residues in a Polymer Brush. *Colloids Surf., B* **2009**, *70* (1), 91-97.
53. Guo, C.; Boullanger, P.; Jiang, L.; Liu, T., Highly Sensitive Gold Nanoparticles Biosensor Chips Modified with a Self-Assembled Bilayer for Detection of Con A. *Biosens. Bioelectron.* **2007**, *22* (8), 1830-1834.
54. Bellapadrona, G.; Tesler, A. B.; Grünstein, D.; Hossain, L. H.; Kikkeri, R.; Seeberger, P. H.; Vaskevich, A.; Rubinstein, I., Optimization of Localized Surface Plasmon Resonance Transducers for Studying Carbohydrate-Protein Interactions. *Anal. Chem.* **2011**, *84* (1), 232-240.
55. Jayawardena, H. S. N.; Wang, X.; Yan, M., Classification of Lectins by Pattern Recognition Using Glyconanoparticles. *Anal. Chem.* **2013**, *85* (21), 10277-10281.
56. Jelinek, R.; Kolusheva, S., Carbohydrate Biosensors. *Chem. Rev.* **2004**, *104* (12), 5987-6016.
57. Linman, M. J.; Taylor, J. D.; Yu, H.; Chen, X.; Cheng, Q., Surface Plasmon Resonance Study of Protein-Carbohydrate Interactions Using Biotinylated Sialosides. *Anal. Chem.* **2008**, *80* (11), 4007-4013.
58. Edelman, G. M.; Cunningham, B. A.; Reeke, G. N., Jr.; Becker, J. W.; Waxdal, M. J.; Wang, J. L., The Covalent and Three-Dimensional Structure of Concanavalin A. *Proc. Natl. Acad. Sci. U. S. A.* **1972**, *69* (9), 2580-4.
59. Perçin, I.; Yavuz, H.; Aksöz, E.; Denizli, A., Mannose-Specific Lectin Isolation from Canavalia Ensiformis Seeds by Phema-Based Cryogel. *Biotechnol. Progr.* **2012**, *28* (3), 756-761.
60. Fraser, A. R.; Hemperly, J. J.; Wang, J. L.; Edelman, G. M., Monovalent Derivatives of Concanavalin A. *Proc. Natl. Acad. Sci. U.S.A.* **1976**, *73* (3), 790-794.

61. Becker, J.; Trügler, A.; Jakab, A.; Hohenester, U.; Sönnichsen, C., The Optimal Aspect Ratio of Gold Nanorods for Plasmonic Bio-Sensing. *Plasmonics* **2010**, 5 (2), 161-167.
62. Duan, H.; Hu, H.; Kumar, K.; Shen, Z.; Yang, J. K. W., Direct and Reliable Patterning of Plasmonic Nanostructures with Sub-10-Nm Gaps. *ACS Nano* **2011**, 5 (9), 7593-7600.
63. Zhao, J.; Jensen, L.; Sung, J.; Zou, S.; Schatz, G. C.; Van Duyne, R. P., Interaction of Plasmon and Molecular Resonances for Rhodamine 6g Adsorbed on Silver Nanoparticles. *J. Am. Chem. Soc.* **2007**, 129 (24), 7647-7656.
64. Chen, H.; Kou, X.; Yang, Z.; Ni, W.; Wang, J., Shape- and Size-Dependent Refractive Index Sensitivity of Gold Nanoparticles. *Langmuir* **2008**, 24 (10), 5233-5237.
65. Love, J. C.; Estroff, L. A.; Kriebel, J. K.; Nuzzo, R. G.; Whitesides, G. M., Self-Assembled Monolayers of Thiolates on Metals as a Form of Nanotechnology. *Chem. Rev.* **2005**, 105 (4), 1103-1170.
66. Lahiri, J.; Isaacs, L.; Grzybowski, B.; Carbeck, J. D.; Whitesides, G. M., Biospecific Binding of Carbonic Anhydrase to Mixed Sams Presenting Benzenesulfonamide Ligands: A Model System for Studying Lateral Steric Effects. *Langmuir* **1999**, 15 (21), 7186-7198.
67. Patel, N.; Davies, M. C.; Hartshorne, M.; Heaton, R. J.; Roberts, C. J.; Tendler, S. J. B.; Williams, P. M., Immobilization of Protein Molecules onto Homogeneous and Mixed Carboxylate-Terminated Self-Assembled Monolayers. *Langmuir* **1997**, 13 (24), 6485-6490.
68. Bellapadrona, G.; Tesler, A. B.; Grünstein, D.; Hossain, L. H.; Kikkeri, R.; Seeberger, P. H.; Vaskevich, A.; Rubinstein, I., Optimization of Localized Surface Plasmon Resonance Transducers for Studying Carbohydrate-Protein Interactions. *Anal. Chem.* **2011**, 84 (1), 232-240.
69. Marinakos, S. M.; Chen, S.; Chilkoti, A., Plasmonic Detection of a Model Analyte in Serum by a Gold Nanorod Sensor. *Anal. Chem.* **2007**, 79 (14), 5278-83.

CHAPTER 5 REFRACTIVE INDEX SENSITIVITY OF NANOSTRUCTURED SILVER FILM, AND COMPARISON TO GOLD NANOSTRUCTURES

5.1 Introduction

Nanostructures of noble metal (gold, silver, and copper) on interacting with the electromagnetic radiation produces localized surface plasmon resonance (LSPR).¹ This process results in an enhancement of light scattering giving rise to surface plasmon resonance band. For the nanostructure of noble metals, this resonance band falls in visible or near-IR region, creating the possibilities to obtain them simply through UV–Vis setups using transmission or reflection geometry.¹ Therefore, there is a possibility that high-throughput, cheaper, and miniaturized biosensing optical device can be made by using these nanostructures of noble metals as a transducer. The sensitivity of nanostructures to be used as a transducer depends on their shape, size, elemental composition, separating distance, and refractive index surrounding the nanostructures.²

Many nanostructures reported before were in the form of individual particles or rods having different shapes.³⁻⁴ The major issues with these types of nanostructures are stability and reproducibility. Higher sensitivity can be obtained while data are acquired from colloidal solutions but on immobilization on substrate for biosensing, decreased in sensitivity and damping of spectra has been reported before.⁵

Commercializing the nanostructured–based transducer has not been successful yet because of some of these major issues, including preparation method, reproducibility, stability of transducer structure and sensitivity.⁶ If we use nanostructured films instead of

individual nanoparticles, we can address some of the issues that are hindering the nanostructured transducer from commercialization.

Different group have used different techniques to create different types of nanostructured metal film, the popular of which are nanosphere lithography technique to create nanotriangles⁷ and sputtering followed by annealing technique to create gold island films⁸. Our group has also previously developed the electrochemical technique to prepare such films of gold nanostructure to create nanostructured gold film (NGF).⁹ The nanostructure prepared by our technique is reproducible, stable, and very sensitive to detect the biomolecule on its surface using localized surface plasmon resonance spectroscopy. The NGF containing plate can also be used to detect biomolecules using electrochemical technique. None of the previously reported film can be used for both optical and electrochemical technique to detect the biomolecules as the films were formed on the glass substrate with the individual structures separated from each other at certain distance making a nonconductive plate overall.

Here, we report the electrochemical preparation technique to create nanostructured silver film (NSF), present refractive index sensitivity of prepared NSF under different conditions and compare the results with the previously formed gold nanostructures.

Study of nanostructured silver film is of interest because silver gives better sensitivity, produces sharper peak, and is cheaper to prepare compared to gold nanostructures. The main disadvantage of silver compared to gold is that even though silver is chemically and physically a relatively inactive metal it is more active than gold and can slowly oxidize or tarnish. However, the popularity of using silver metal

nanostructures as LSPR transducers is increasing and different types of important biomolecular interactions and detection have been performed on the surface of silver nanostructures. In one such study, a film of silver nanotriangles was used to detect the interaction between amyloid-derived diffusible ligands (ADDL) with anti-ADDL.¹⁰ ADDLs are small soluble oligomers found at early stages of amyloid- β (A β) self-assembly, and it has been found that ADDLs cause neurological dysfunctions relevant to memory. It has also been suggested that interaction of ADDL with anti-ADDL antibodies is possibly involved in development of Alzheimer's disease. Finally, the possible use of silver nanotriangles as a LSPR based transducer for early detection of Alzheimer's disease from body fluid has been reported.¹⁰

It is noteworthy to report that there are other instances where oxidation of silver structures was avoided by creating an inert environment during the study of the biomolecular interactions.¹¹ In this study, we are particularly focusing on showing a relationship between deposition time and bulk refractive index sensitivity and figure of merit of the silver nanostructures formed.

5.2 Result and Discussion

Figure 5.1 shows schematic diagram of the steps performed for the preparation of nanostructured silver film (NSF). As in NGF, we prepared NSF starting by sputtering 200 nm thick gold on top of a silicon wafer, onto which we attached glass slides using epoxy glue. We cured the epoxy by keeping glass slides attached silicon wafer inside oven at 150 °C for 2 h. We stripped the glass slide to obtain flat gold surface onto which we have electrochemically deposited silver from 0.05 M KAg(CN)₂ dissolved in sodium carbonate supporting electrolyte by applying different potentials for different times.

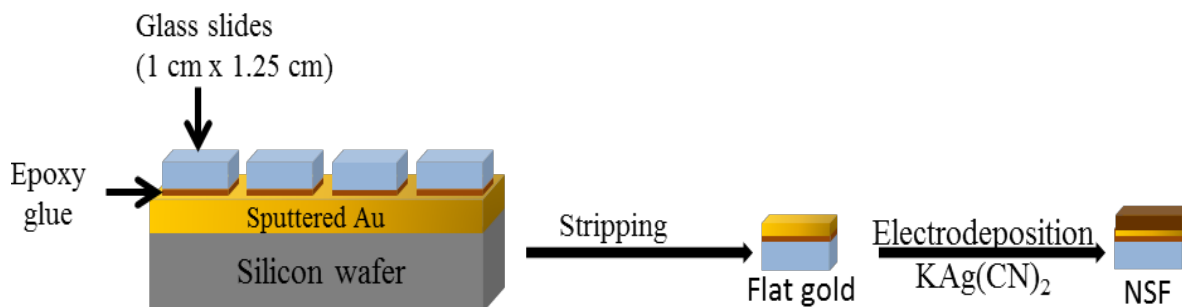


Figure 5.1 Schematic diagram of NSF preparation steps.

We started the experiment by applying four different potentials: -1.0 V, -1.2 V, -1.4 V, and -1.6 V for 60 s. We have found that at -1.6 V potential the gold film peels off of the glass substrate instantly, at -1.4 V we sometimes observed slight peeling off the samples, but at -1.0 V and -1.2 V, the samples were physically stable. We have found that the structured prepared at -1.2 V shows higher sensitivity compared to structures formed at -1.0 V which must be because of smoother structure formed at -1.0 V, and we found similar results before on NGF.⁹ As a next step, we varied deposition time of silver on the gold substrate keeping -1.2 V as an optimal potential. **Figure 5.2** shows LSPR spectra obtained for nanostructured silver film prepared by applying -1.2 V for 30 s (black) to 180 s (cyan), with the increment of 30 s. The NSF formed using this method is robust with peak wavelength increasing with time of deposition. It can also be seen that when we prepare NSF using 30 s deposition time, a sharper peak with a smaller full width at half maximum (FWHM) can be obtained. When we kept depositing silver for a longer time, the LSPR spectrum kept broadening giving higher FWHM and hence decreasing the sensitivity of the structure in term of figure of merit, which can be obtained by dividing bulk RIS by FWHM. For the LSPR based transducers, nanostructures that can show an initial peak wavelength near the beginning of visible

light wavelengths and can give better sensitivity is always preferred, as on immobilizing biomolecules on surface of such nanostructures there is enough space for the spectra to red shift and still remain within the visible region. Looking at these spectra, we can conclude that this property is maintained in our structures.

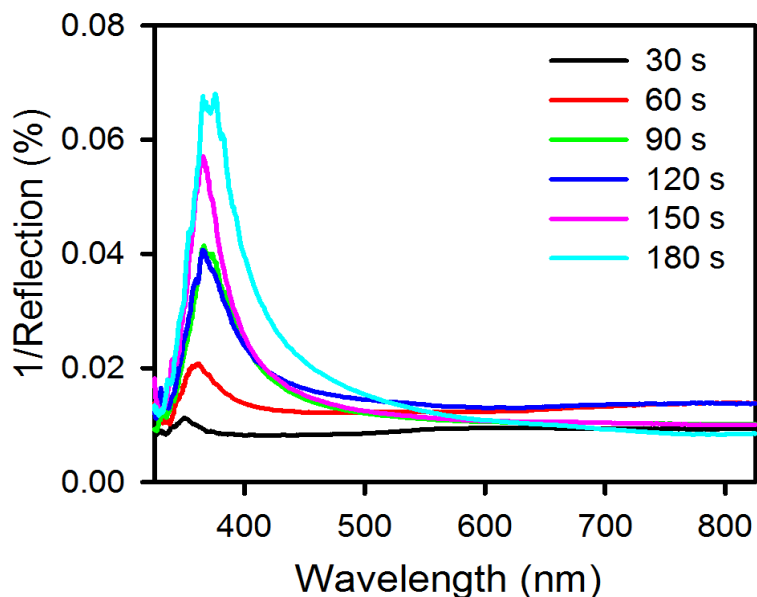


Figure 5.2 LSPR spectra of NSF prepared by applying a deposition potential of -1.2 V for different times (as indicated).

5.2.1 Refractive index sensitivity of NSF

The LSPR spectra of representative NSF formed by deposition potential of -1.2 V for 60 s are shown in **Figure 5.3A** for a series of solvents having different refractive index when passed over the NSF surface. The solvents used were water (1.330), ethanol (1.359), heptane (1.387), DMF (1.431), and toluene (1.496). As the solvent having higher refractive index is passed over the NSF surface, the peak becomes broader with a red shift in the peak wavelength. When the peak wavelength is plotted versus refractive index, a linear fit can be obtained whose slope provides the bulk refractive index

sensitivity (RIS) of the structure. The bulk RIS of the NSF prepared by applying different deposition times was found to range from 142–239 nm/RIU, with the nanostructures having higher initial wavelength maximum also having higher sensitivity but lower FOM and vice versa. It should be noted that preparing the NSF by using a deposition time of 90 s or higher does not increase the sensitivity, as can be seen by comparing the slope of the peak wavelength versus refractive index for the 90 s data with that for the 150 s data (**Figure 5.4**). Changing to a longer deposition time only serves to broaden the FWHM. These as-prepared and optimized sensitive NSF could open possibilities for the development of cheap and compact LSPR transducers giving better responses for diagnostic assay applications.

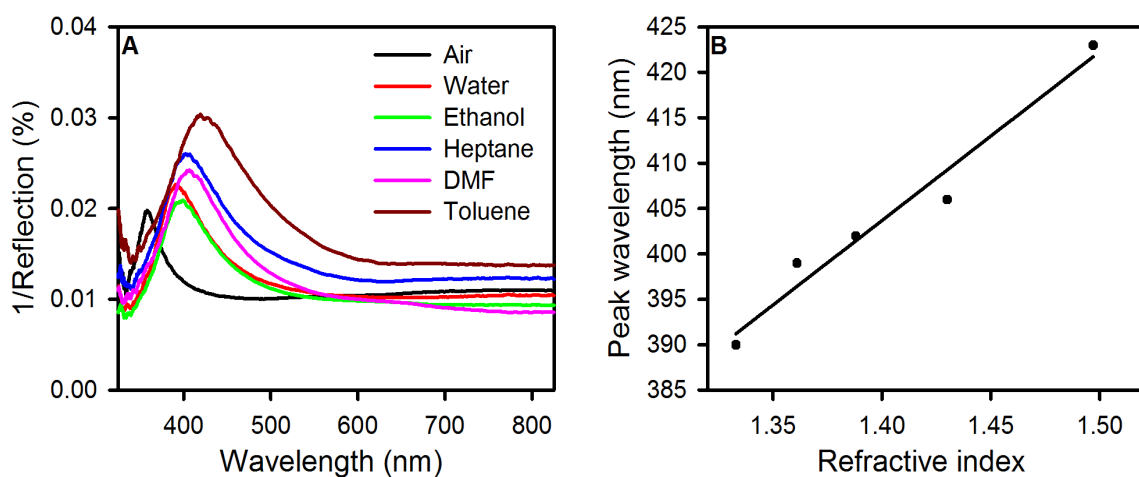


Figure 5.3 (A) LSPR spectra obtained when solutions of different refractive index were passed over the NSF surface prepared by depositing silver for 1 min by applying a -1.2 V potential. (B) A linear fit line is obtained when peak wavelength is plotted vs. refractive index, the slope of which gives the bulk RIS of the nanostructure and is equal to 186 ± 6 nm/RIU.

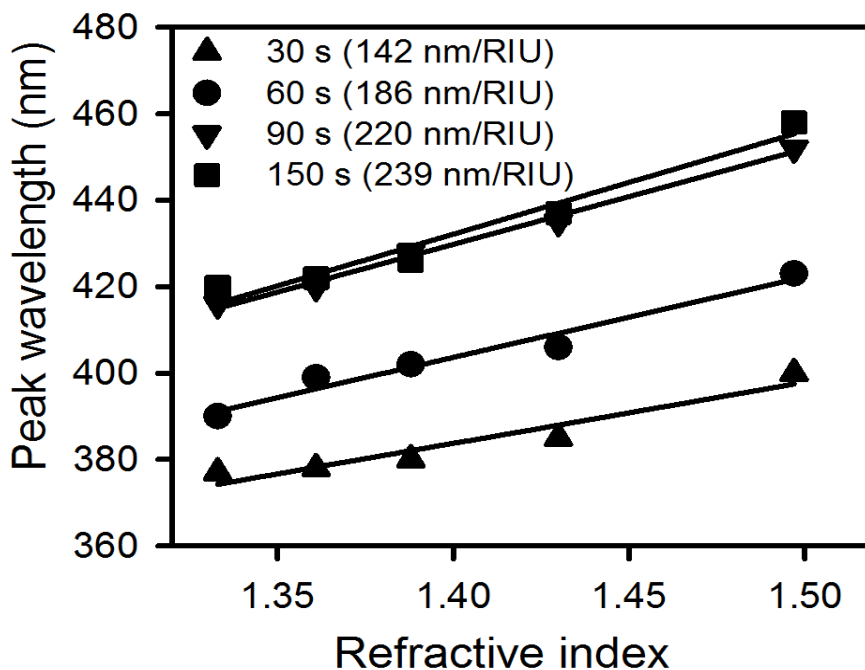


Figure 5.4 Comparison of bulk RIS of NSF prepared by applying -1.2 V for different deposition times (30 s, 60 s, 90 s, and 150 s).

Figure 5.5 shows SEM images of NSF prepared by applying -1.2 V and -1.4 V for 1 min on increasing magnification. Low-magnification images show a large domain without cracks, and uniformity of deposition can be seen. The high-magnification image shows that the -1.2 V prepared structure has less spherical structures whereas the structure prepared at -1.4 V are more spherical.

5.2.2 Comparison of RIS of silver and gold nanostructure

The bulk refractive index sensitivity (RIS) of a nanostructured silver film prepared by deposition voltage -1.2 V and deposition time 1 min reaches up to 186 nm/RIU and have figure of merit (FOM) 2.3. Bulk RIS increases with deposition time up to 150 s to give 239 nm/RIU, but decreasing the FOM to 2.0 because of higher full width at half maxima.

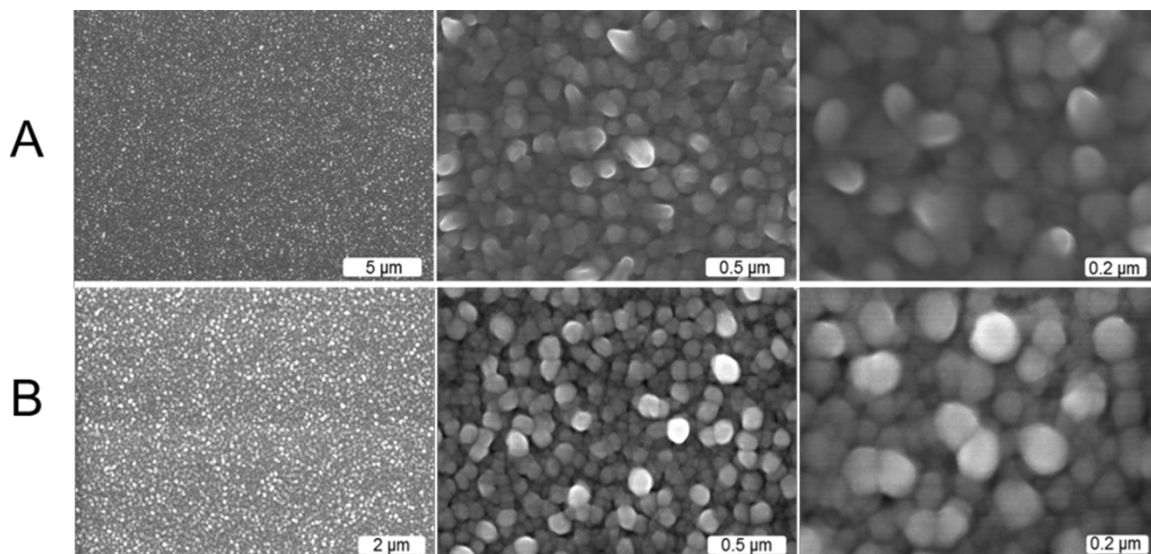


Figure 5.5 SEM images of NSF prepared by applying (A) -1.2 V and (B) -1.4 V potential for 1 min of deposition time. The images from left to right are in order of increasing magnification (scale bars: $2\text{ }\mu\text{m}$, $0.5\text{ }\mu\text{m}$, $0.2\text{ }\mu\text{m}$, respectively).

Deposition for 180 s or more only shows broader peak with decreasing bulk RIS and FOM. On the other hand, the nanostructured gold film can reach up to nearly 100 nm/RIU at the best optimized condition with FOM of 1.7. The bulk RIS of nanoporous gold film reaches up to 115 nm/RIU at the best optimized condition with the FOM of 1.3.

5.3 Conclusions

A facile electrochemical technique was used to prepare LSPR sensitive NSFs. The NSFs prepared by varying deposition times and potentials were compared for bulk RIS and FOM. We conclude that the structures prepared at -1.2 V for 1 min can be an optimal transducer owing to its sensitivity in term of bulk RIS and FOM.

We have also compared the different types of nanostructured films prepared in our lab. We have found that NSFs are the best in terms of both bulk RIS and FOM. They can be synthesized in fewer steps and are cheaper to produce. However, they are prone to oxidation in an open environment, so an inert environment is needed to perform biosensing experiments. NPG films have better sensitivity compared to NGF, but still contains significant amount of silver in the sensitive nanostructures. Decreasing the amount of silver from NPG films, decreases overall sensitivity of the structure. It also involves multiple preparation steps. NGFs on the other hand are easier to prepare in a few steps and show better sensitivity compared to other published gold nanostructures as a film. The structures formed are physically robust and chemically inert to be used as a transducer for biosensing.

5.4 References

1. Willets, K. A.; Van Duyne, R. P., Localized Surface Plasmon Resonance Spectroscopy and Sensing. *Annu. Rev. Phys. Chem.* **2007**, *58*, 267-297.
2. Lee, K.-S.; El-Sayed, M. A., Gold and Silver Nanoparticles in Sensing and Imaging: Sensitivity of Plasmon Response to Size, Shape, and Metal Composition. *J. Phys. Chem. B* **2006**, *110* (39), 19220-19225.
3. Mock, J.; Barbic, M.; Smith, D.; Schultz, D.; Schultz, S., Shape Effects in Plasmon Resonance of Individual Colloidal Silver Nanoparticles. *J. Chem. Phys.* **2002**, *116* (15), 6755-6759.
4. Kelly, K. L.; Coronado, E.; Zhao, L. L.; Schatz, G. C., The Optical Properties of Metal Nanoparticles: The Influence of Size, Shape, and Dielectric Environment. *J. Phys. Chem. B* **2003**, *107* (3), 668-677.
5. Jenkins, J. A.; Zhou, Y.; Thota, S.; Tian, X.; Zhao, X.; Zou, S.; Zhao, J., Blue Shifted Narrow Localized Surface Plasmon Resonance from Dipole Coupling in Gold Nanoparticles Random Arrays. *J. Phys. Chem. C* **2014**.
6. Karakouz, T.; Holder, D.; Goomanovsky, M.; Vaskevich, A.; Rubinstein, I., Morphology and Refractive Index Sensitivity of Gold Island Films. *Chem. Mater.* **2009**, *21* (24), 5875-5885.
7. Zhang, X.; Hicks, E. M.; Zhao, J.; Schatz, G. C.; Van Duyne, R. P., Electrochemical Tuning of Silver Nanoparticles Fabricated by Nanosphere Lithography. *Nano Lett.* **2005**, *5* (7), 1503-1507.
8. Ruach-Nir, I.; Bendikov, T. A.; Doron-Mor, I.; Barkay, Z.; Vaskevich, A.; Rubinstein, I., Silica-Stabilized Gold Island Films for Transmission Localized Surface Plasmon Sensing. *J. Am. Chem. Soc.* **2007**, *129* (1), 84-92.
9. Bhattarai, J. K.; Sharma, A.; Fujikawa, K.; Demchenko, A. V.; Stine, K. J., Electrochemical Synthesis of Nanostructured Gold Film for the Study of Carbohydrate-Lectin Interactions Using Localized Surface Plasmon Resonance Spectroscopy. *Carbohydr. Res.* **2014**.
10. Haes, A. J.; Hall, W. P.; Chang, L.; Klein, W. L.; Van Duyne, R. P., A Localized Surface Plasmon Resonance Biosensor: First Steps toward an Assay for Alzheimer's Disease. *Nano Lett.* **2004**, *4* (6), 1029-1034.
11. Han, Y.; Lupitskyy, R.; Chou, T.-M.; Stafford, C. M.; Du, H.; Sukhishvili, S., Effect of Oxidation on Surface-Enhanced Raman Scattering Activity of Silver Nanoparticles: A Quantitative Correlation. *Anal. Chem.* **2011**, *83* (15), 5873-5880.